PSE PRESS

CSChE Systems & Control Transactions

VOLUME 1

Selected Extended Abstracts from the
Systems & Control Division Sessions of the
71st Canadian Chemical Engineering Conference

October 24-27, 2021

Montréal, Québec

Edited by Thomas A. Adams II

Chemical Institute of Canada | *For Our Future*
Institut de chimie du Canada | *Pour notre avenir*

http://PSEcommunity.org/LAPSE:2021.0797

CSChE Systems & Control Transactions

Vol 1

Edited by

Thomas A. Adams II
McMaster University

PSE PRESS
PSEcommunity.org
PSE Press ● Hamilton

Chemical Institute of Canada | *For Our Future*
Institut de chimie du Canada | *Pour notre avenir*

CSChE Systems & Control Transactions, Volume 1

PSE Press
Hamilton, Ontario, Canada

Living Archive for Process Systems Engineering (LAPSE) Archive ID
LAPSE:2021.0797

Library and Archives Canada Catalogue
A catalogue record and copy of this book is available from Library and Archives Canada

Electronic Book
ISBN 978-1-7779403-0-0

10 9 8 7 6 5 4 3 2 1

Typeset in Constantina and Corbel

Suggested Citations for Individual Articles
Paper Style
Student MC, Supervisor QR. Title of the article. *CSChE Systems & Control Trans*, 1:43-48 (2021).

Proceedings Style
Student MC, Supervisor QR. Title of the article. *In: CSChE Systems & Control Transactions*, October 24-27, Montréal, Quebéc, Canada, 2021. Vol 1 Pages 1-6. ISBN 9781777940300.

Editor-in-Chief
Thomas A. Adams II, PhD
McMaster University
Chair, Systems & Control Division, Canadian Society for Chemical Engineering

Contents

Preface

Extended Abstracts

Biotechnology and Global Health

Industrial Applications in Process Systems Engineering

Artificial Intelligence and Machine Learning in Process Systems Engineering

Process Systems Engineering for Energy and the Environment

Methodologies and Fundamentals in Process Systems Engineering

Introduction

Thomas A. Adams II, PhD
McMaster University
Chair, Systems and Control Division, Canadian Society for Chemical Engineering

The Systems & Control Division

The Canadian Society for Chemical Engineering (CSChE), one of the constituent societies of the Chemical Institute of Canada, is a not-for-profit association made up of chemical engineering professionals, academics, students, and employees of government organizations. The Systems & Control (S&C) division of the CSChE is a collection of members who are interested in process systems engineering (PSE), which includes the design, control, optimization, modelling, simulation, planning, scheduling, and operations of chemical processes.

The S&C Division is an active group with many activities, which include:

(a) The development and management of the Living Archive for Process Systems Engineering, an open-access repository for pre-prints, post-prints, open access articles, research data, simulations, computer code, and other research assets relevant to the field of PSE.

(b) The development of technical standards relevant to the field, such as the development of a new standard on eco-technoeconomic analyses via Standards Council of Canada.

(c) Providing financial supporting for regional conferences relevant to the S&C division

(d) Distribution of relevant announcements and information to our members, such as job postings, new books, and events

About This Volume

This volume contains selected extended abstracts from the 2021 Canadian Chemical Engineering Conference (CCEC 2021). Six sessions at the conference were managed by the S&C Division, which represent the broad and changing nature of PSE in Canada:

Artificial Intelligence and Machine Learning in Process Systems Engineering
Biotechnology and Global Health
Data Driven Analytics, Control, and Optimization
Industrial Applications in Process Systems Engineering
Methodologies and Fundamentals in Process Systems Engineering
Process Systems Engineering for Energy and the Environment

Prospective contributors submitted short abstracts for either oral presentations or poster presentations for various sessions. Volunteer session co-chairs, who were chosen from the S&C division membership, reviewed each abstract for quality and relevance, and used a ranking system to determine acceptance as an oral presentation or poster, or, rejection. Those who were accepted were invited to contribute an extended abstract to this volume, which contains more information and detail than the original short abstract.

These extended abstracts were not peer reviewed. They generally consist of research-in-progress and early stage research results. In most cases, the information presented herein may be included as a part of a peer-reviewed study in a later publication. For more information about individual works, or to find out about updates, you are encouraged to contact the corresponding author of each study.

Each article has a corresponding LAPSE ID. Visit the LAPSE record to see if the authors have linked their contribution to other material, such as presentation slides, downloadable data, or other publications.

Chairs and Co-Chairs

Systems & Control Division Chair

Thomas A. Adams II, *McMaster University*

Session Co-Chairs

Artificial Intelligence and Machine Learning in Process Systems Engineering

Bhushan Gopaluni, PhD. *University of British Columbia*
Martin Guay, PhD. *Queens University*
Simant Upreti, PhD. *Ryerson University*

Biotechnology and global health

Céline Vaneeckhaute, PhD. *University of Laval*
Eric Walling, MSc. *University of Laval*
Vikramaditya Yadav, PhD. *University of British Columbia*

Data Driven Analytics, Control, and Optimization

Moncef Chioua, PhD. *Polytechnique Montréal*
Carl Duchesne, PhD. *University of Laval*
Qinqin Zhu, PhD. *University of Waterloo*

Industrial Applications in Process Systems Engineering

Ali Elkamel, PhD. *University of Waterloo*
Kim McAuley, PhD. *Queens University*
Ajay Ray, PhD. *University of Western Ontario*

Methodologies and Fundamentals in Process Systems Engineering

Debaprasad Dutta, MaSC. *Ryerson University*
Nicolas Hudon, PhD. *Queens University*
Kamil Khan, PhD. *McMaster University*

Process Systems Engineering for Energy and the Environment

Xiang Li, PhD. *Queens University*
Luis Ricardez-Sandoval, PhD. *University of Waterloo*
James Rose, BEng. *McMaster University*

We greatly thank our session chairs and presenters for their time and effort in contributing to this conference!

CSChE Systems & Control Transactions

Open Access | Original Research

Conference Proceedings
Canadian Chemical Engineering Conference 2021
October 24-27, Montréal, Québec, Canada

PSEcommunity.org/LAPSE:2021.0786

PSE PRESS

Set Membership Estimation for Dynamic Flux Balance Models

Xin Shen and Hector Budman*

Department of Chemical Engineering, University of Waterloo, Waterloo, ON, Canada
* Corresponding Author: hbudman@uwaterloo.ca.

ABSTRACT

A set membership estimator (SME) based on limited number of measurements is proposed for estimating metabolite concentrations using dynamic flux balance models (DFBMs). To deal with multiplicity of solutions of the DFBM, a weighted primal dual method is used to find solutions that best fit the data. Multiparametric nonlinear programming is applied to propagate uncertainty in initial concentrations along a batch/fed-batch operation. The proposed method has been applied to E. coli batch and fed-batch fermentation without noise.

Keywords: set membership estimation, dynamic flux balance model, multiparametric programming, multiplicity, weighted primal dual method, variable structure system

Date Record: Original manuscript received October 13, 2021. Published October 21, 2021

1. INTRODUCTION

Dynamic flux balance models (DFBMs) are one type of genome-based structural models that has gained attention in recent years due to their ability to describe the bioprocess with fewer tuning parameters in comparison with other modelling techniques. In DFBMs, cells are regarded as optimizing agents able to distribute resources to maximize/minimize a biological objective. Accordingly, DFBMs models can be formulated as a linear programing (LP) constrained optimization problem which solution serves as input to mass balances of metabolites.

However, due to multiplicity of solutions of the LP, the possible trajectories of the state variables, i.e. metabolites concentrations, for given initial condition are not unique for DFBMs. In a previous investigation by the authors, a weighted primal dual method (WPDM) was used to solve the multiplicity problem by introducing the weights that drive the optimization search to solutions that best fit the experimental data [1]. The WPDM approximates the LP by nonlinear convex programming. To propagate uncertainty in initial bounds on concentrations during the batch multiparametric nonlinear programming is applied to convert the system into a variable structure one.

A set membership estimation approach is used based on few available measurements to estimate bounds for all states. The proposed methods have been applied to fed-batch and batch fermentation of *E. coli* model.

2. METHODS

2.1 Dynamic Flux Balance Models.

The governing equation of DFBMs can be defined as Eq. (1) – Eq. (3) [2].

$$x_{k+1} = B(u_k, x_{vol,k})x_k + \Delta t x_{bio,k} S v_k + h(u_k, x_{vol,k}) \quad (1)$$

$$y_k = [x_{bio,k}\ x_{vol,k}]^T \quad (2)$$

$$x_0 \in \mathcal{P}_0 \quad (3)$$

where x_k is state vector of n_x state variables at time step k, including state biomass concentration $x_{bio,k}$ and volume $x_{vol,k}$. Δt is discrete time step size. S is stoichiometry matrix of metabolic reactions. v_k is metabolic flux. B and h are matrix -valued and vector-valued functions of input variable u_k and volume. In this research, we assume biomass concentration and volume can be measured. The initial states are uncertain but are known to lie within the set $\mathcal{P}_0$.

The flux v_k is obtained by solving LP in Eq. (4):

$$\min_{v_k} c^T v_k$$
$$\text{Subject to } Av_k \leq F\theta_k(x_k, y_k, u_k) + b \quad (4)$$

where matrix $A \in \mathbb{R}^{m \times n_x}$ and $F \in \mathbb{R}^{m \times n_\theta}$ are constant matrix and b is constant vector. c is objective coefficient vector. $\theta_k = H(y_k, u_k)x_k + g(y_k, u_k)$. $H(y_k, u_k)$ and $g(y_k, u_k)$ are matrix -valued and vector-valued functions of input variable u_k and measurements.

2.2 Weighted Primal Dual Method

Multiplicity of solutions is frequently observed in DFBM in view of insufficient number of constraints. Since the solution of LP is usually not unique for Eq. (4), different trajectories can be obtained by different LP solvers. To deal with the multiplicity issue, a weighted primal dual method (WPDM) was proposed in a previous work by the authors [1]. The

WPDM involves the addition of a weighted barrier function into the optimization cost as per Eq. (5), where w are interior-point weights and z are slack variables. μ is set as a very small number, $\mu = 1e^{-8}$. For simplicity, subscript k is omitted. Since the WPDM has strictly convex form objective, the solution is unique. When multiple solutions coexist in the original LP defined in Eq. (4), different unique solutions can be obtained corresponding to different weights. The weights in WPDM are calibrated to fit available experimental data.

$$\begin{aligned} &\min_{v} c^T v - \mu \sum_{i=1}^{m} w_i \ln(z_i) \\ &\text{Subject to } Av + z = F\theta + b \\ &z > 0 \end{aligned} \tag{5}$$

2.3 Multiparametric Programming

2.3.1 Multiparametric Nonlinear Programming

Since θ in Eq. (5) varies with time step k, θ can be regarded as varying parameters. Accordingly, Eq. (5) can be treated as a multiparametric nonlinear strictly convex programming problem defined as follows:

$$\begin{aligned} &\min_{v} f(v, \theta) \\ &\text{Subject to } Gv < K\theta + d \\ &G_e v = K_e \theta + d_e \\ &\theta \in \Theta \end{aligned} \tag{6}$$

Assume the Θ can be divided into n_Θ nonoverlapping sets as Θ^1, ..., Θ^{n_Θ}. These sets are defined as critical regions. For given θ_0 in a critical region Θ^j, the corresponding optimal solution is v_0. So at θ_0 and v_0, the solution can be approximated by a local quadratic programming problem as Eq. (7) [3].

$$\begin{aligned} &\min_{v} \frac{1}{2}(v - v_0)^T Q(v - v_0) + (L^T + (\theta - \theta_0)^T N)(v - v_0) \\ &\quad + r(v_0, \theta_0) \\ &\text{Subject to } Gv < K\theta + d \\ &G_e v = K_e \theta + d_e \\ &\theta \in \Theta^j \end{aligned} \tag{7}$$

where $H = \nabla^2_{vv} f(v_0, \theta_0)$, $L = \nabla_v f(v_0, \theta_0)$, $N = \nabla^2_{\theta v} f(v_0, \theta_0)$, $r(v_0, \theta_0) = f(v_0, \theta_0) + \nabla^T_\theta f(v_0, \theta_0)(v - v_0) + \frac{1}{2}(\theta - \theta_0)\nabla^2_{\theta\theta} f(v_0, \theta_0)(\theta - \theta_0)$. The optimal solution of Eq. (7) has affine form as $v^j = A^j_Q \theta + b^j_Q$, where superscript j denotes that for each critical regions a different analytical expression can be used to calculate the optimum. Different published multiparametric nonlinear programming codes can be used to obtain the constant matrix A_Q and b_Q. The critical regions can be further divided into smaller critical regions to improve the solution accuracy.

2.3.2 Variable Structure System

The state equation in Eq. (1) can be rewritten as Eq. (8) and Eq. (9).

$$\begin{aligned} x_{k+1} &= B(u_k, x_{vol,k})x_k + \Delta t x_{bio,k} S(A^j_Q \theta_k + b^j_Q) \\ &\quad + h(u_k, x_{vol,k}) \end{aligned} \tag{8}$$

$$\theta_k(x_k, y_k, u_k) \in \Theta^j \tag{9}$$

Since θ_k is a function of x, different critical region corresponds to different state space models. Therefore, the state equation is different in different positions of the state space thus defining a piecewise continuous system representation that is referred to as a variable structure system [4].

2.3 Set Membership Estimation (SME)

For the variable structure system defined above set membership estimation can be used to propagate the initial value uncertainty $\mathcal{P}_0$ to estimate bounds on concentrations along the batch based on few measurements. Set membership estimation is based on set operations, usually including linear mapping, projection, translation, Minkowski addition, intersection, union, and outer approximation. Multi-Parametric Toolbox 3 [5] and bensolve tools [6] are used to preform the set operations. By taking the measurements into consideration, post estimate sets of states at different time steps can be obtained. Through projections of the obtained sets, the upper bounds and lower bounds of states can be determined.

3. RESULTS AND DISCUSSION.

The proposed set membership estimation has been applied to an E. coli fermentation example for both batch and fed-batch operations. To test the multiplicity issue, an artificial constraint is added into the DFBM of *E. coli* on purpose. Figure 1 presents the results of simulation of batch fermentation. Assume only volume and biomass concentration are measured, the red dash lines are estimated bounds for unmeasured states which also cannot be estimated by classical observers. It was concluded that the proposed SME generates tight bounds that contain the true plant state denoted by black line. Similar results have been obtained for fed-batch operations.

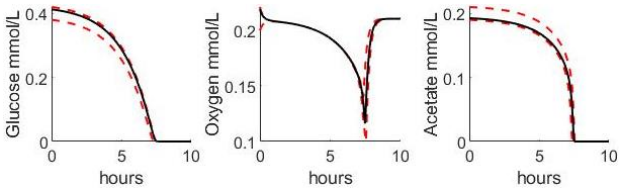

Figure 1. SME for batch fermentaiton of *E.coli*.

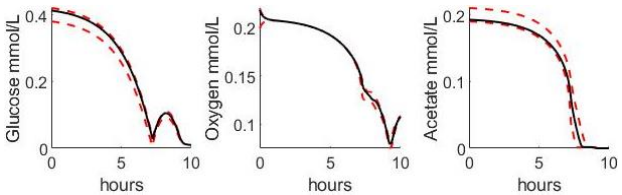

Figure 2. SME for fed-batch fermentaiton of *E.coli*..

4. CONCLUSIONS.

DFBMs based on WDPM solver can solve the multiplicity problem. Multiparametric nonlinear programming is used to convert the DFBMs based on WPDM solver into a variable structure system. Based on the simplified variable structure system, SME can propagate the initial value uncertainty by set operations and estimate the bounds of unmeasured states given the limited measurements.

ACKNOWLEDGEMENTS

We acknowledge the support from The Natural Sciences and Engineering Research Council of Canada (NSERC), Mitacs, and Sanofi Pasteur.

REFERENCES

1. Shen X, Budman H. A method for tackling primal multiplicity of solutions of dynamic flux balance models. *Comp Chem Eng*, 143:107070 (2020).
2. Mahadevan R, Edwards JS, Doyle FJ III. Dynamic flux balance analysis of diauxic growth in Escherichia coli. *Biophy J*, 83:3:1331-1340 (2002).
3. Johansen TA. On multi-parametric nonlinear programming and explicit nonlinear model predictive control. *Proceedings of the 41st IEEE Conference on Decision and Control*, 3:2768-2773 (2002).
4. Shen X, Budman H. A Type of Set Membership Estimation Designed for Dynamic Flux Balance Models. *Processes* 9:10:1762 (2021).
5. Herceg M, Kvasnica M, Jones CN, et al. Multi-parametric toolbox 3.0, *Euro Cont Conf*, 502-510 (2013).
6. Löhne A, Weißing B. Equivalence between polyhedral projection, multiple objective linear programming and vector linear programming. *Math Oper Res* 84:2:411-426 (2016).

This conference proceeding has not been peer reviewed.

CSChE Systems & Control Transactions

Open Access | Original Research

Conference Proceedings
Canadian Chemical Engineering Conference 2021
October 24-27, Montréal, Québec, Canada

PSEcommunity.org/LAPSE:2021.0787

PSE PRESS

Towards the Development of a Diagnostic Test for Autism Spectrum Disorder: Big Data Meets Metabolomics

Juergen Hahn*

Rensselaer Polytechnic Institute, Center for Biotechnology and Interdisciplinary Studies, Troy, NY 12180, USA
* Corresponding Author: hahnj@rpi.edu

ABSTRACT

Autism Spectrum Disorders (ASD) are a group of neurological disorders that present with limited social communication/interaction and restricted, repetitive behaviors/interests. The current estimate is that approximately 1.9% of children in the US are diagnosed with ASD. While this is a high prevalence and the economic burden by ASD is significant, there is still considerable debate regarding the underlying pathophysiology of ASD. Because of this lack of biological knowledge, autism diagnoses are restricted to observational behavioral and psychometric tools. This work takes a step towards the goal of incorporating biochemical data into ASD diagnosis by analyzing measurements of metabolite concentrations of the folate-dependent one-carbon metabolism and transulfuration pathways. Unlike traditional approaches that are based upon comparing differences in individual metabolite concentrations between children with and without an ASD diagnosis, we made use of multivariate classification via Fisher Discriminant Analysis and used Kernel Partial Least Squares regression to predict adaptive behavior. Although these results need to be replicated in independent studies, these analyses suggest combinations of metabolites in these pathways as potential biomarkers for ASD.

Keywords: autism spectrum disorder, fisher discriminant analysis, kernel partial least squares

Date Record: Original manuscript received Sept 27, 2021. Published October 21, 2021

INTRODUCTION

Autism Spectrum Disorders (ASD) are a group of neurological disorders that present with limited social communication and interaction and restricted, repetitive behaviors and interests [1]. The current estimate is that approximately 1.9% of children in the US are diagnosed with ASD [2]. While this is a high prevalence and the economic burden by ASD is significant [3], there is still considerable debate regarding the underlying pathophysiology of ASD. Because of this lack of biological knowledge, autism diagnoses are restricted to observational behavioral and psychometric tools. Subsequently, the average age at which children receive an ASD diagnosis is four years, while it is generally acknowledged that diagnosis between 18-24 months is possible [4]. Furthermore, disparities by race/ethnicity in estimated ASD prevalence as well as disparities in the age of earliest comprehensive evaluation and presence of a previous ASD diagnosis or classification, suggest that access to treatment and services might be lacking or delayed for some children. Thus, confirmation and expansion of the unique metabolic abnormalities in children with autism that accurately distinguishes them from typically developing children would not only strengthen diagnostic accuracy, but also provide insights into underlying pathophysiology and a personalized approach to treatment options.

METHODS

Stepping towards this goal of incorporating biochemical data into ASD diagnosis, we analyzed measurements of metabolite concentrations of the folate-dependent one-carbon metabolism and transulfuration pathways taken from blood samples of 83 participants with ASD and 76 age-matched typically developing peers. Fisher Discriminant Analysis enabled multivariate classification of the participants as on the spectrum or typically developing which results in 96.1% of all typically developing participants being correctly identified as such while still correctly identifying 97.6% of the ASD cohort [5]. Furthermore, kernel partial least squares was used to predict adaptive behavior, as measured by the Vineland Adaptive Behavior Composite score, where measurement of five metabolites of the pathways was sufficient to predict the Vineland score with an R^2 of 0.45 after cross-validation [5]. These results have been partially validated in a separate study involving 156 participants with an ASD diagnosis where over 88% of the participants were correctly identified as having an ASD diagnosis [6].

DISCUSSION

This computational study enhances the analysis obtained from traditional population-level statistics and suggest that folate-dependent one carbon metabolism and transsulfuration may play an integral role in ASD pathophysiology. Furthermore, the work highlights the contribution that systems approaches can make for clinical studies involving significant amount of data, some of which are often correlated and require multivariate analysis methods [7]. Although these results need to be replicated in independent studies, these analyses suggest combinations of metabolites in these pathways as potential biomarkers for ASD.

ACKNOWLEDGEMENTS

The authors gratefully acknowledge partial financial support from the National Institutes of Health (Grant R01AI110642).

REFERENCES

1. *American Psychiatric Association, Diagnostic and Statistical Manual of Mental Disorders*, 5th ed. Washington, D.C.: American Psychiatric Association (2013)
2. Maenner MJ, Shaw KA, Baio J, et al. Prevalence of Autism Spectrum Disorder Among Children Aged 8 Years — Autism and Developmental Disabilities Monitoring Network, 11 Sites, United States, 2016. *MMWR Surveill Summ 2020*. 69:SS-4:1–12 (2020)
3. Leigh JP and Du J. Brief Report: Forecasting the Economic Burden of Autism in 2015 and 2025 in the United States. *J Autism Dev Disord*, 45:12:4135–4139 (2015)
4. McPheeters ML, et al. Screening for Autism Spectrum Disorder in Young Children: A Systematic Evidence Review for the U.S. Preventive Services Task Force. Rockville, Maryland, 13-05185-EF-1 (2016)
5. Howsmon DP, Kruger U, Melnyk S, James SJ, and Hahn J. Classification and Adaptive Behavior Prediction of Children with Autism Spectrum Disorder based upon Multivariate Data Analysis of Markers of Oxidative Stress and DNA Methylation. *PLoS Computational Biology* 13:3:e1005385 (2017)
6. Howsmon DP, Vargason T, Rubin RA, Delhey L, Tippett M, Rose S, Bennuri SC, Slattery JC, Melnyk S, James SJ, Frye RE, and Hahn J. Multivariate Techniques Enable a Biochemical Classification of Children with Autism Spectrum Disorder versus Typically-Developing Peers: A Comparison and Validation Study. *Bioeng Translational Med* 3:2:156-165 (2018)
7. Vargason T, Grivas G, Hollowood-Jones KL, and Hahn J. Towards a Multivariate Biomarker-based Diagnosis of Autism Spectrum Disorder: Review and Discussion of Recent Advancements. *Seminars in Pediatric Neurology* 34:100803 (2020)

CSChE Systems & Control Transactions

Open Access | Original Research

Conference Proceedings
Canadian Chemical Engineering Conference 2021
October 24-27, Montréal, Québec, Canada

PSEcommunity.org/LAPSE:2021.0788

PSE PRESS

Dynamic Modelling of T Cell Vaccination Response

Alisa C. Douglas[a], Thomas A. Adams II*[a], and David A. Christian[b]

[a] McMaster University, Department of Chemical Engineering, Hamilton, Ontario, Canada
[b] University of Pennsylvania, School of Veterinary Medicine, Philadelphia, Pennsylvania, United States
* Corresponding Author: tadams@mcmaster.ca

ABSTRACT

In our previous work, a mathematical, agent-based dynamic model was developed which simulates the response of the mammalian omentum to a T cell vaccine injection during the expansion phase. The model tracks how each individual naïve T cell interacts with antigen presenting cells, and subsequently primes and divides over an 8-day period following vaccine injection. The model works from first principles; individual phenomena based on experimental observation and theory are incorporated into the model, and the collection of many such phenomena together create a nuanced model of the system as a whole. In this work, we show that the model works well in other relevant tissues, such as the spleen.

Keywords: T cells, stochastic, dynamic, modeling, vaccine

Date Record: Original manuscript received October 7, 2021. Published October 21, 2021.

ORIGINAL MODEL

Background

In our previous work [1], a mathematical, stochastic, dynamic model called the STORE model (STochastic Omentum REsponse) was developed in MATLAB to simulate T cell priming and division in the omentum after vaccination. The model is stochastic and agent-based such that each individual agent is tracked over time during the dynamic simulation valid up to a period of 8 days after vaccine injection. The individual agents include antigen presenting cells and T cells at various stages during vaccination:

A = naïve T cells
B = primed T cells
C = primed T cells which have matured and divided once
D = C cells which have divided
E = D cells which have divided
F = E cells which have divided
G = F cells which have divided
H = G cells which have divided
I = H cells which have divided
J = I cells which have divided, plus all subsequent generations
P = antigen presenting cells (APCs)

The model inputs include the initial count of T cells injected, the arrival rate of APCs which is the time required for APCs to travel from the site of injection to the tissue of interest, the number of APCs or antigens that enter the tissue, the division time for J, as well as probabilities of cells leaving the system or maturing (see [1] for specifics). The model uses probability distributions for each cell type to mature, divide and leave the system, based on their age and/or concentration within the tissue. At each time step, random number generators are used in conjunction with probability distribution functions to determine the action (or inaction) of each agent in the system.

The previous work showed that the model fit experimental data well in mice for multiple experimental data sets provided by different groups. The model was shown to have sufficient complexity to explain how multiple different behavioural regimes (such as cyclic behaviour vs. pulse behaviour) naturally arise from the system given different input stimuli. However, the model was previously developed only for the omentum and only verified with data for the omentum. In this work, we investigate whether the model is also predictive for other relevant tissues, such as the lymph nodes, spleen, and peritoneum. Most of the underlying phenomena in the omentum also occurs in these other tissues, and so the model that was developed for the omentum should have some predictive qualities as well in these other tissues.

APPLICATION TO OTHER TISSUES

The mathematical model initially developed for the omentum could be extended to other tissues including the peritoneum, draining lymph nodes, non-draining lymph nodes, and the spleen. However, experimental data shows that there are timing differences in when the explosive growth rates of T cells actually occur.

T Cell Counts in Other Tissues

Applying the MATLAB model for the omentum to other tissues in the body would be significant as the route of T cell migration in the body can be determined. Understanding T cell behaviour and their migration patterns between different tissues help explain important phenomena such as central

memory and resident memory (different aspects of protective immunity) as well as the stochastic nature behind immunization. Recent experiments at the University of Pennsylvania [2] examined the cell count of T cell stages after injecting T cells intravenously (IV) 24 hours before vaccinating intraperitoneally (IP), which is through the peritoneum (in the abdomen). Five different tissues were examined: draining lymph nodes, non-draining lymph nodes, omentum, peritoneum and spleen. The study was done 15 mice which were tracked for 90 hours with data collected from at a time points 42, 66 and 90 hours post injection (5 mice per time point). We note that these data are in preparation for publication and so only summaries and averages are provided in this work.

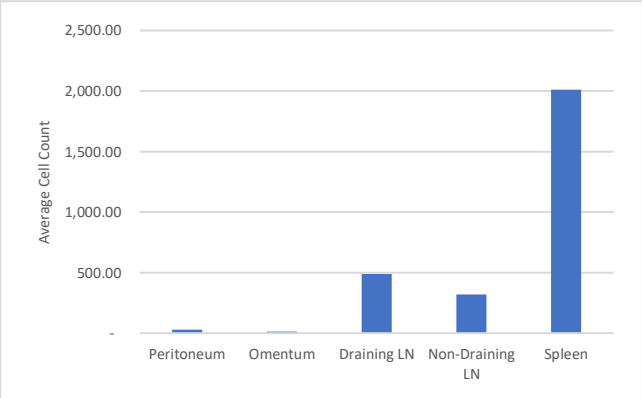

Figure 1. Average total cell count of T cells after 42 hours.

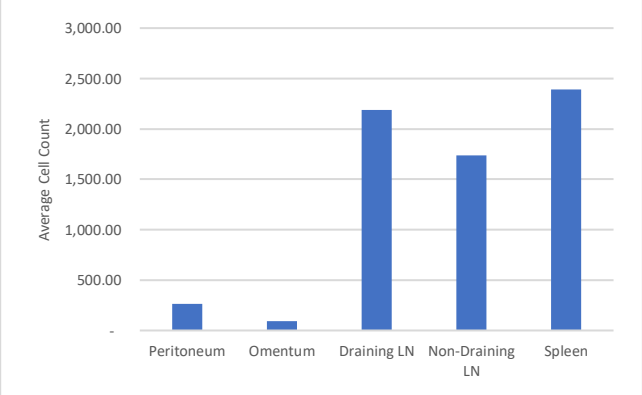

Figure 2. Average total cell count of T cells after 66 hours.

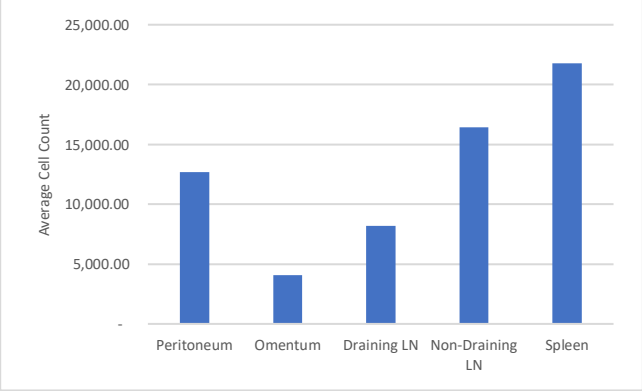

Figure 3. Average total cell count of T cells after 90 hours.

The average cell counts of each group of five mice are shown in Figure 1. The majority of the T cells accumulate in the spleen, with some in the draining and non-draining lymph nodes and a small number of cells in the omentum and peritoneum. Figure 2 shows the later time point where the lymph nodes become more active than the spleen as cells are dividing more rapidly. The results in Figure 3 shows omentum and peritoneum are the last tissues for T cells to accumulate.

Method of Injection Influences Cell Counts

The distribution of T cells is based on the method of injection. When cells are injected IV, cells travel through the circulatory system and majority of the cells end up in the spleen as there is a large supply of blood. Lymph nodes have a small blood supply, however due to the large number of lymph nodes in the body, an adequate amount of T cells can also be found in the lymph nodes. Alternatively, when the vaccine is injected IP and APCs are generated in the peritoneum, the cells enter the lymphatic system which connects directly to the lymph nodes and no cells will enter the spleen as it is not connected to the lymphatic system. This explains why the lymph nodes become more active than the spleen even though it has more T cells. Although the majority of the T cells are in the spleen and some in the lymph nodes, all the APCs generated by IP immunization will travel to the lymph nodes and not the spleen. The APCs meet the T cells in the lymph nodes and prime them causing a chain reaction of cell divisions. On the other hand, as no APCs enter the spleen, the naive T cells present in the spleen will not be primed and therefore the cells will not divide. This explains the activeness of lymph nodes compared to the spleen. After clonal expansion of primed T cells, they leave through the lymph and blood. Some will enter the spleen through the blood supply, and some are recruited to the infection site, which are the omentum and peritoneum. This is supported by figures 1-3 which show omentum and peritoneum are the last to have accumulation of T cells due to recruitment.

SIMULATIONS OF THE SPLEEN

Because the previous analysis shows that the cell counts do not all peak at the same time in each tissue, and because of the complex interactivity between tissues, the original model developed for the omentum cannot be used directly to model the system as a whole. However, it can be readily adapted to each individual tissue by changing some key parameters and then creating additional model elements that represent the transportation of cells between tissues. As a first step, we examine the adaptation of the omentum model for the spleen.

T Cell Activity in the Spleen

The same mathematical model was applied to an unpublished dataset from University of Colorado [3] (again, only averages are presented), where they tracked the activity of T cells in the spleen of 19 mice. T cells were injected IV 12 hours prior to injecting the APCs IV. Two sets of mice were used in this study: wild type (WT) and knockout (KO). WT mice are found in natural populations and KO mice are genetically modified by removing a gene to study its effects. Data were collected from 3 mice at a time after approximately 24, 36, 48, 72, 96 and 168 hours with an exception of using 4 mice for data collection at 72 hours.

The MATLAB model originally developed for the omentum and for a different set of experiments was modified for the spleen simply by changing the values of some model parameters (such as the reproduction rate of J) to best fit the experimental data. The fundamental theory and underlying phenomena was not modified. The simulation results for the WT mice are shown in Figures 4-9, where the lines are the simulation, and the circles are the experimental average cell counts of the indicated cell type at the appropriate time point. We note that some cell type counts in this experiment are extremely small, and that data points are not integers because they are averages of 3-4 data points. The model itself is restricted to only having integer values.

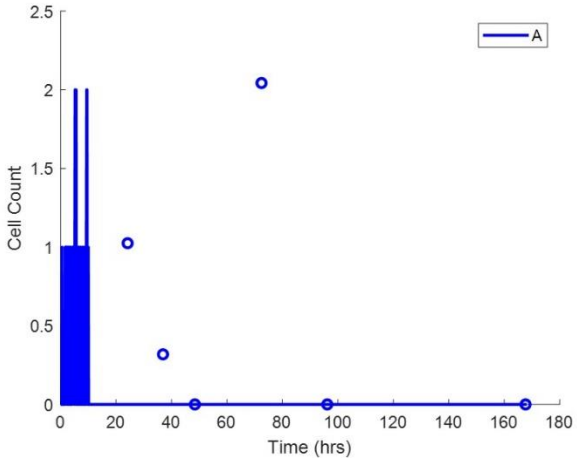

Figure 4. Simulation results for A cells (naïve T cells) in WT mice.

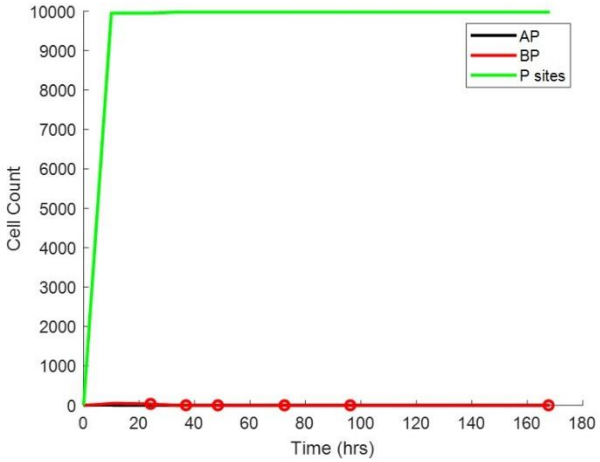

Figure 5. Simulation results for AP (naïve T cells bound to APC), BP (matured AP) and P sites (total APC binding sites) in WT mice.

The arrival rate of APCs in the simulation was set such that it takes 10 hours for all APCs to arrive in the spleen (starting at time zero and continuing at a constant rate until 10 hours have elapsed) to simulate the effects of IV injection. This is more rapidly than if it were to be injected IP and travel through the lymphatic system (requiring about 24 hours to arrive). The division time parameter for J was also set to 8 hours as T cell replication was occurring at a faster rate in the spleen (in the previous omentum model, 24 hours used [1]). This can be seen in Figure 8. The leaving probabilities of BP (p_{BP}), E through H (p_{EH}) and I through J (p_{IJ}), see [1] for definitions, were also decreased (from the omentum model) down to 0.001, 0.001 and 0, respectively.

From the results, the cells in the spleen seem to accumulate faster than in the omentum. It can be seen in Figure 4 that the number of naive T cells (A) present in the spleen were only 1 or 2 cells which is extremely small compared to the data from University of Pennsylvania. This is because APCs were injected in at least 200 times the magnitude of T cells, therefore APCs were in a large excess and consumed majority of the naive T cells at a rapid rate. Hence, the initial number of T cells (N_{A0}) was set as 50 and the initial number of APCs (N_{P0}) were set at a ratio of $N_{A0}/0.005$.

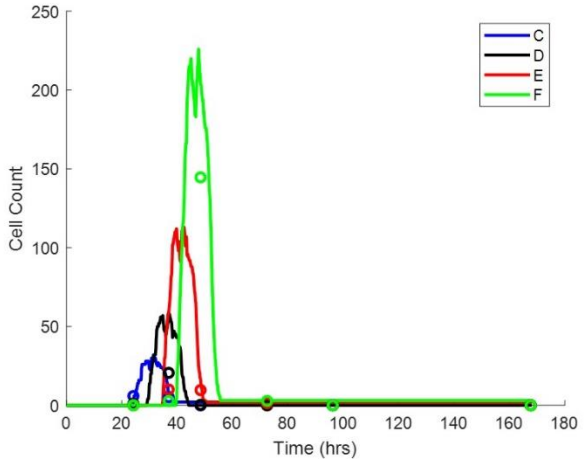

Figure 6. Simulation results for stages C through F in WT mice.

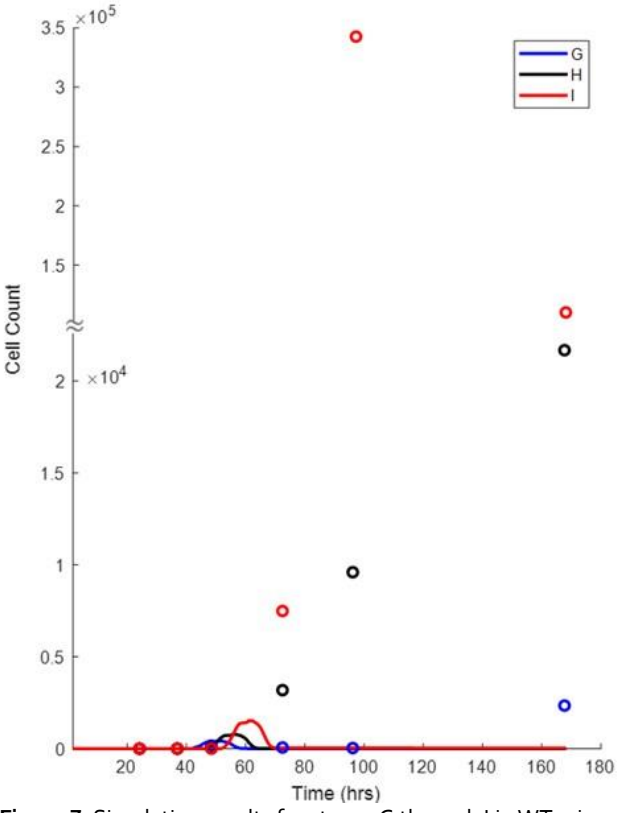

Figure 7. Simulation results for stages G through I in WT mice.

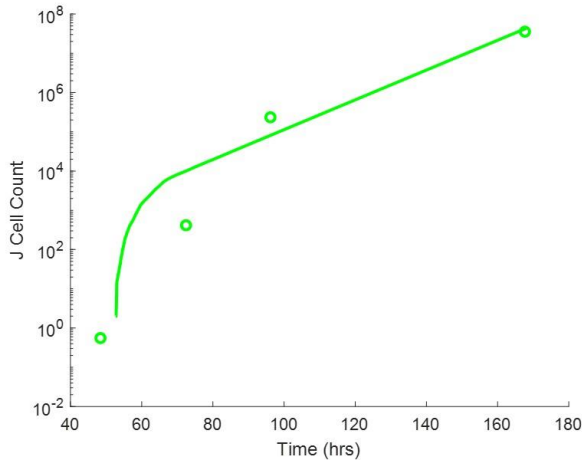

Figure 8. Simulation results for J cells in WT mice.

This simulation results from using these parameters can be seen in Figure 5 as the green curve represents total APC sites which is in excess. Having APC in excess results in "pulse-like" behaviour, which is in contrast to having excess naïve T cells which results in "cycle-like" behaviour [1]. In these experiments, having excess APC counts mean that naïve T cells are almost immediately paired with APCs upon arrival in the spleen, which is why cell counts of type A and BP are so low as shown in Figures 4 and 5. The model reflects this in the experiment quite well.

As the cells start to divide (Figure 6) the pulse behaviour is evident in cell divisions C through F, with each stage going through a single maximum before they have all either divided or have left the system. The simulation fits the data extremely well considering the model was created and validated using a different injection method, tissue, and application with drastically different number of T cells and APCs. This demonstrates that the underlying physical phenomena considered in the model characterises the cell interactions within a tissue well.

However, Figure 7 shows the simulation fits the data poorly for cells G through I. The peaks from the simulation are not occurring at the same time as the data and the data points are orders of magnitude too high for the simulation peaks to possibly reach. The data also do not follow the theorem used by the model, which is considers that almost all cells double by division after 5.3 hours and a small amount would remain in the system. By using this principle, the subsequent divisions should peak at approximately double the peak cell count of the previous stage (i.e. the peak of G should be double of the peak of F). However, the data points for G through J are significantly higher than the previous stages.

Possible explanations for these results are either the cells are dividing at an extremely rapid rate due to an unknown phenomenon, more likely, or the experimental method used to differentiate the cells into stages is not accurate. This could happen as cell count in stages G through J are much higher than the previous stages which can result in clustering of cells. This can cause the gating of cells obtained from flow cytometry to be inaccurate and group the cells into the incorrect stages. As a result, the number of cells in each stage are likely to be a combination of G, H, I and J cells, which would explain the extremely high magnitude in cell count.

Figure 8 shows a semi-log plots of type J counts, noting that type J cells include all subsequent generations of J and their divisions. Because of this grouping, type J grows exponentially, doubling about every 8 hours. Since the simulations predict both the value and timing of the peak extremely well with experimental data, it is likely that the unexpectedly high and irregular experimental data for types G- I are due to measurement error.

Effects of Gene Removal

KO mice were genetically engineered as the IL-27R gene was removed from each mouse. Data were collected in the same fashion [3] and the spleen model was applied. The simulation results for KO mice are shown in Figure 9-13.

The model used the same parameters from the WT mice except for the division time of J which was slower in KO mice. This is expected, since inhibiting IL-27 signaling is likely to reduce cell division rates, cause J cells to leave the system at a greater rate, and/or cause J cells to die at a greater rate [4]. The replication time was changed from 8 to 10 hours and the simulation results of J cells are shown in Figures 13. The results in Figures 9-12 show the KO mice data set is similar to WT data for stages A through I, and the simulation fits the data very well. Since all other parameters were unchanged from the first experiment, this serves to validate the spleen model.

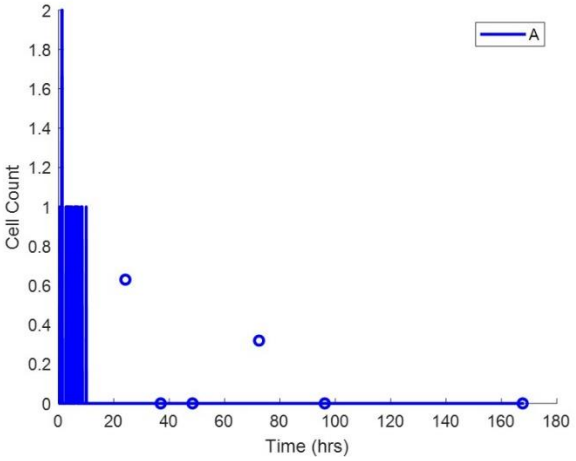

Figure 9. Simulation results for A cells (naïve T cells) in KO mice.

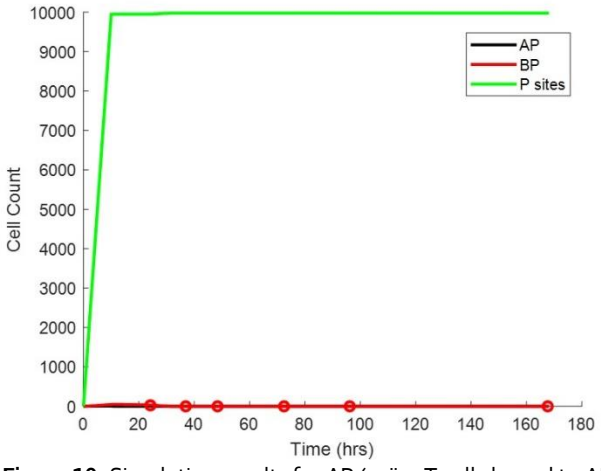

Figure 10. Simulation results for AP (naïve T cells bound to APC), BP (matured AP) and P sites (total APC binding sites) in KO mice.

CONCLUSIONS

The STORE model, which was originally developed for the omentum, can also accurately predict T cell responses in the spleen by changing four model parameters relating to the probabilities that certain cell types leave the system or die at any given time, as well as the rate at which type J cells divide. This shows that T cell priming and division is likely governed by the same fundamental phenomena in both tissues, but with some differences that require further study and explanation. These differences may be unique to the tissue, or, they may be the result of other cross-tissue phenomena, such as how T cells are transported throughout the system between tissues. It can also be concluded that genetic deletion of IL-27R from T cells likely either results in slower replication of type J cells, and/or, an increase in the leaving rate of J from the system, since all other model parameters remained the same when comparing WT and KO mice.

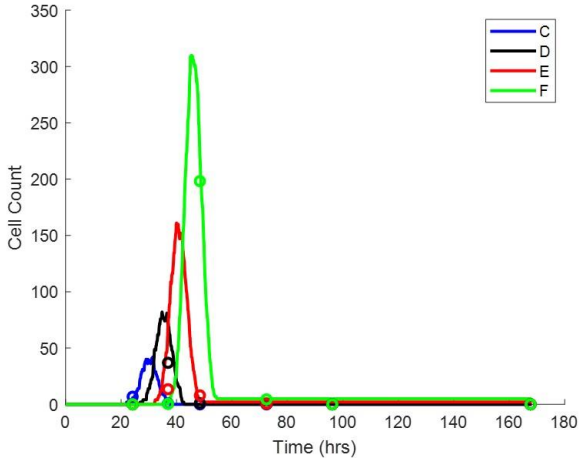

Figure 11. Simulation results for stages C through F in KO mice.

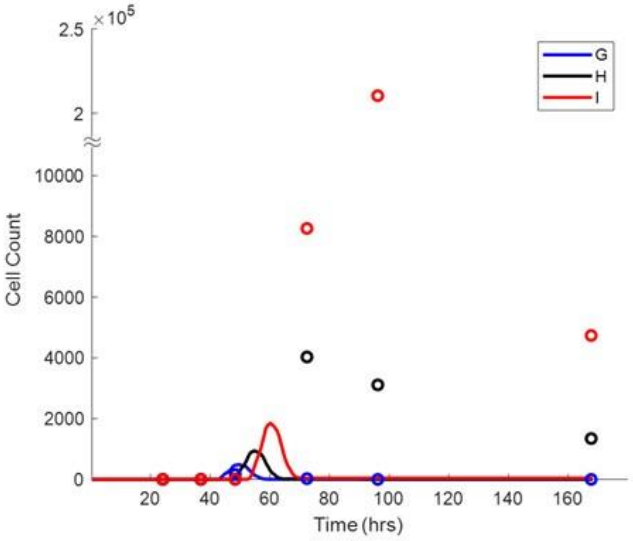

Figure 12. Simulation results for stages G through I in KO mice.

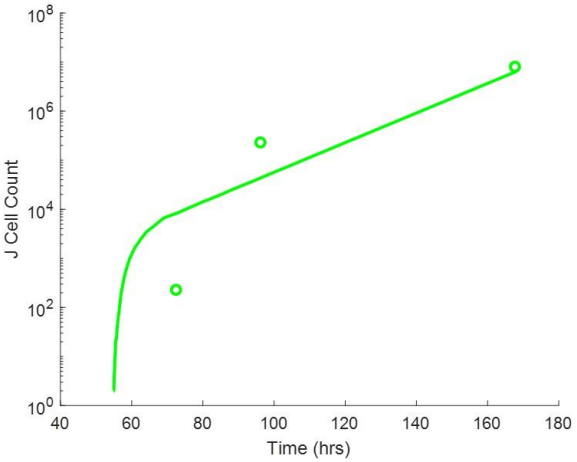

Figure 13. Simulation results in a semi-log plot for J cells in KO mice.

REFERENCES

1. Christian DA, Adams TA II, Smith TA, Shallberg LA, Theisen DJ, Phan AT, Abraha M, Perry J, Ruthel G, Clark JT, Murphy KM, Kedl, RM, Hunter CA. cDC1 coordinate innate and adaptive responses in the omentum required for T cell priming and memory. Submitted to *Immunology* (2020). https://www.biorxiv.org/content/10.1101/2020.07.21.214809v1
2. Christian DA, et al. Unpublished data set of cell counts in variant tissues from IP vaccine injections (2021).
3. Kedl R, et al. Unpublished data set of cell counts in the spleen from IV vaccine injections (2021).
4. Pennock ND, Gapin L, Kedl RM. IL-27 is required for shaping the magnitude, affinity distribution, and memory of T cells responding to subunit immunization. *PNAS* 111:16472-16477 (2014).

CSChE Systems & Control Transactions

Open Access | Original Research

Conference Proceedings
Canadian Chemical Engineering Conference 2021
October 24-27, Montréal, Québec, Canada

PSEcommunity.org/LAPSE:2021.0789

PSE PRESS

Ozone Sterilization of N95 Masks

Mohammad Irfan Malik, Karen Bechwaty, François Guitzhofer, and Inès Esma Achouri*

University de Sherbrooke, Department of Chemical and Biotechnology Engineering, Sherbrooke, Quebec, Canada
* Corresponding Author: Ines.Esma.Achouri@USherbrooke.ca

ABSTRACT

The rapid spread of the COVID-19 worldwide pandemic at the beginning of 2020 has significantly affected the global economy with severe human and economic losses. Despite the shortage of personal protective equipment, the facemask serves as a fundamental means to protect health care professionals' and restrict the spread of the coronavirus. However, due to the limited stock of facemasks, many sterilization methods were developed to eliminate the infection and established strategies for fast and repeated reuse without affecting the filtration efficiency. The current study extrapolates the effective utilization of the ozonic sterilization of the N95 mask. First, we demonstrated the potential of ozone as a disinfectant that successfully destructs the organic food colour compounds deposited on the N95 mask; In the quantitative part of this research, the N95 facemask pieces were soaked in diphenylamine solution and later oxidized with ozone under the different intervals of time. Finally, the different standards of diphenylamine and methanol solution were calibrated under the spectrometric analysis to quantify the amount of the oxidized product present in the methanol solvent. The results show that ozone disinfectant has a significant potential to sterilize the mask, recover the cost-effective reuse, and can generate a comparable result equivalent to the other high-cost techniques. Furthermore, it was observed that the sample's ozone exposure time and accurate calibration are vital to influence the organic species' oxidization and accurately quantify the oxidized amount.

Keywords: ozone disinfectant, N95 mask, COVID-19, organic compounds

Date Record: Original manuscript received October 20, 2021. Published October 21, 2021

INTRODUCTION

During the COVID-19 crises, the spread of the COVID-19 in large cities caused the shortage of personal protective equipment (P.P.E.) and widely highlighted the capacity to reuse the P.P.E. worldwide. Despite the challenges, the health care professionals continued to use fundamental respiratory tools such as N95 masks, which filter the 95 % particulate matter at or above the 0.3-micron size [1,2]. Recently, the Italian institute of health has published a report that broadly recommends and emphasize the sanification process for non-healthcare environments to disinfect the surfaces and maintain the hygienic quality in the indoor environments [3]. Therefore, to cope with the shortage and at the same to meet filtration standards, the government, hospitals, and the companies emphasized and doubled their efforts to look for better disinfect solutions for certified masks, including several other personal protective equipment [4,5]. As a result, a great deal of effort and many strategies have been proposed for the quick and safe reuse of the N95 masks. Several disinfection technologies have already been utilized in large hospitals, especially the initial progress with highly concentrated hydrogen peroxides. However, the cost-effective disinfection technologies to cope with the shortage and at the same time disinfect the PPEs with ultra-high filtration is a big challenge [6,7].

Many sterilization methods, such as U.V. irradiation, and steam treatment, also have been used. Nevertheless, light (intensity-wavelength) standardization and mask degradation are significant challenges in U.V. irradiation. However, ozone disinfection is one of the widely accepted methods reported in the literature [8–10]. Besides, its recognition as an effective disinfectant has been widely accepted by numerous international organizations such as the European food and drug administration, the centre for disease control and prevention, the European chemical agency, and the international ozone associations [11]. It is an allotropic form (O3) of oxygen produced from the air using air plasma or U.V. irradiation [2]. The natural presence of ozone in the atmosphere is approximately 0.04 ppm (I ppm = 2mg/m^3), and nearly 90% of the ozone is located in the stratospheric zone. It has roughly ten times higher solubility (49 ml per 100 ml at 0 ^{0}C) in the water compared to oxygen; this makes them immediately react with any biological substance in the biological fluids; in addition, it has a higher density (2.14 kg/m^3) than air, concentrating it close to the environment and indoor stations. It has high reactivity and the potential to oxidize the organic compounds [8,11–13]. Moreover, it has been used successfully in waste water treatments [14,15], and effectivity deactivated the bacteria [13] and some members of the corona family [4,16,17]; Being a gaseous

sterilizations agent, it can assess and disinfect the materials that are difficult to access because of tiny pores [2].

Therefore, this study aims to investigate the potential role of ozone as a disinfectant for N95 masks in indoor environments. Also, the crucial role of ozone in damaging the organic substances in the food colour is highlighted—the reason to choose particular food colours is due to their availability, safety, and ease of use. In addition, for the quantitative analysis, the masks samples were oxidized with diphenylamine and later, the oxidized amount was measured using the calibration method under the spectroscopy characterization. Finally, we demonstrate that this approach is straightforward, cost-effective, and can be extended for further broad-scale research.

METHODS

In the first qualitative set of the experiment, a particular class of quartz reactor as shown in Figure 1, the ozone generator containing oxygen and inert (Ar) cylinders as shown in Figure 2 and different organic food colours (red, green, purple, blue, and black) were used as received without any further treatment. The organic foods relevant to our studies were used without further treatment and endured multiple cycles of ozone exposure.

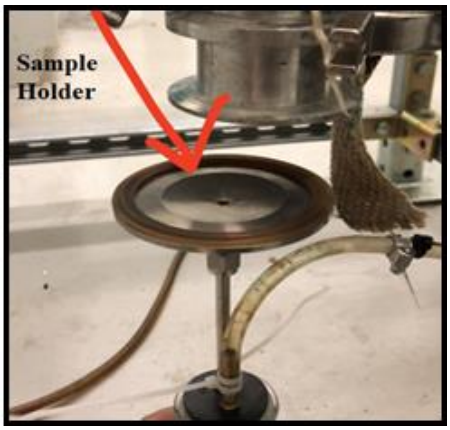

Figure 1: Specimen holder in the quartz reactor.

Initially, the N95 masks were cut into small pieces and later soaked into organic food colour. Before injection of the ozone into the reactor, the reactor was tightly sealed, and it was assured that there was no gas leakage by supplying the Ar gas. Next, the ozone gas was injected from the ozone generator into the reactor for 15 seconds before the sample was collected for analysis. The same procedure was repeated for all the other organic colours (purple, black, yellow, and green).

In the quantitative set of experiments, the N95 mask was cut into ten small pieces and soaked in different colourless 4000 ppm diphenylamine (C6H5)2NH) solutions under the different intervals from 1 to 2 hours, as shown in Table 1.

Later, the soaked samples were individually introduced into the quartz reactor, and the ozone gas was injected into the reactor with the O2 flow rate of 500mL/min until the samples were fully oxidized and returned yellow. Next, the oxidized sample from the reactor was placed under the known amount (15 ml) of methanol until the sample was restored (white) as shown in Figure 3.

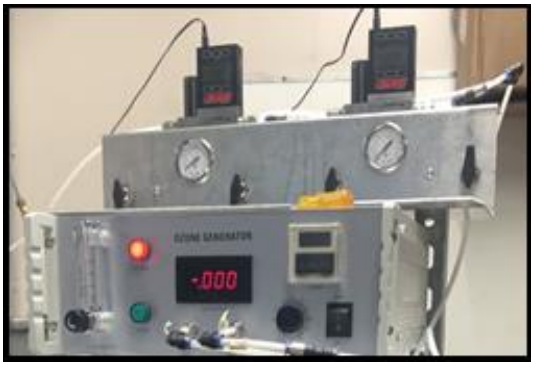
Figure 2. Ozone generator

Table 1: Details of the preparation tests (1 to 9)

Test number	Volume of stock solution (ml)	Number of masks pieces	Ozone exposure time (seconds)	Methanol volume (ml)
1	3	2	120	15
2	2	1	80	15
3	2	1	40	15
4	2	1	20	15
5	2	1	10	15
6	2	1	5	15
7	2	1	3	15
8	2	1	2	15
9	2	1	1	15

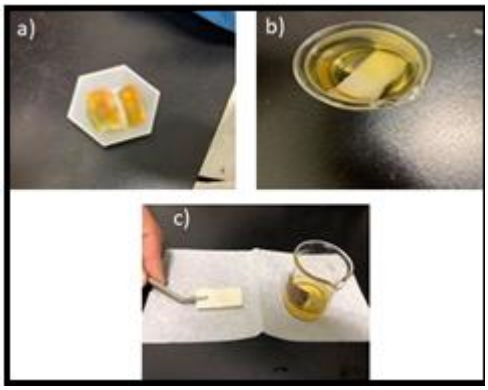

Figure 3. (a) two pieces of oxidized mask initially soaked in 3mL of a 4000 ppm diphenylamine solution (b) oxidized mask soaked in 15 ml of methanol (c) discolouration of the mask after soaking in methanol solution.

Finally, to quantify the amount of oxidized compounds in the methanol, the different known quantities of the standard solution of the methanol and diphenylamine were calibrated, as sown in Figure 4, and the oxidized amount in the methanol sample was quantified using spectrometry characterization. A similar procedure was repeated for all the ten samples reported in Table 1.

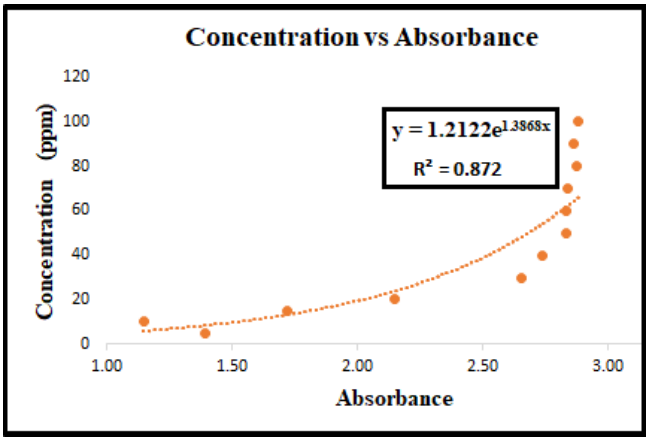

Figure 4. Standard concentration curve as a function of absorbance

RESULT

Figure 5 shows the images of the samples before and after the oxidation with ozone for 20 seconds. Changes in the colour sample after the oxidation validates the successful sterilization of the organic contaminants in the mask samples. It is essential to mention that there was no fabric degradation and elastics loss in the mask strap as shown under the blue arrow in figure 6, except some decline in rigidity and enhancement in the elasticity was observed in the nose wire.

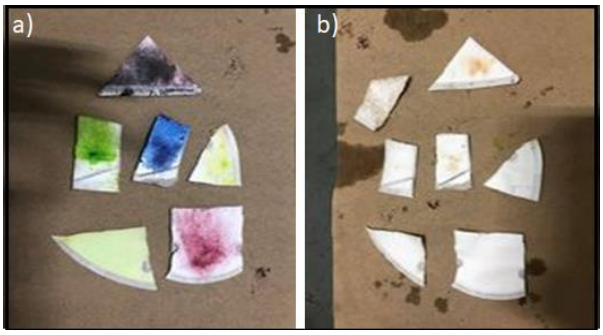

Figure 5. (a) Mask colours before the oxidation and (b) after oxidation (20 seconds)

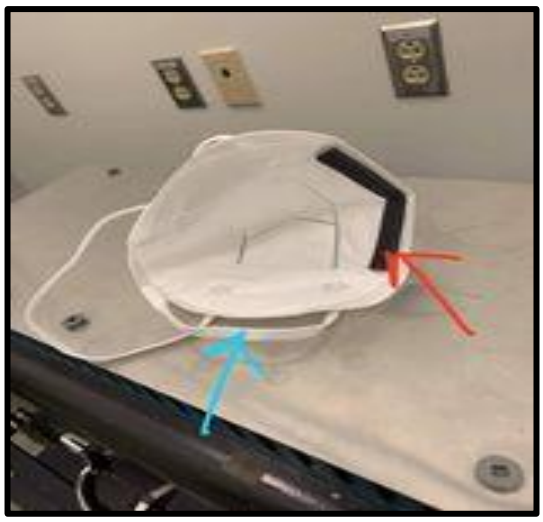

Figure 6. Mechanical test of the mask after the oxidation

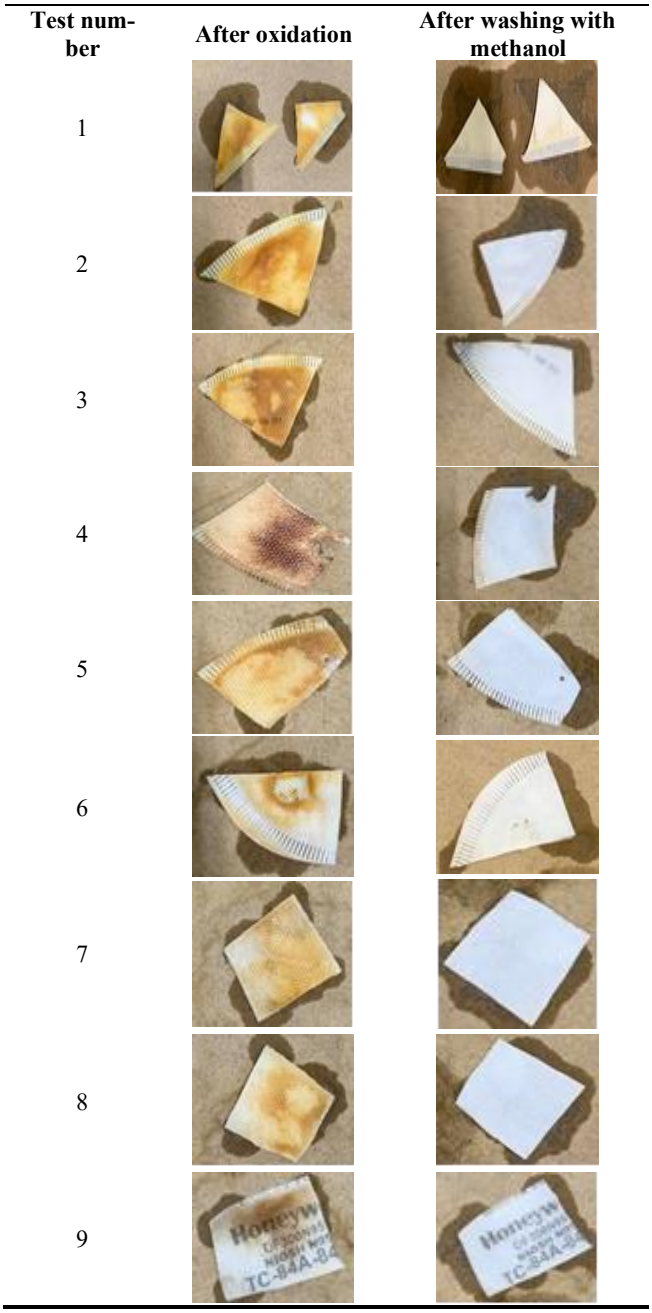

Figure 7. Colours of the masks samples under the oxidized diphenylamine and after the immersion in pure methanol.

Similarly, Figure 7 represents all the nine oxidized mask samples initially soaked in the diphenylamine and later in the methanol solvent. Variation of colour in all the samples indicates that all the oxidized diphenylamine has been absorbed by methanol solvent efficiently. Besides, the yellow colour of the methanol solvent is another indication that methanol solvent has fully absorbed the diphenylamine. Moreover, it is essential to mention that only three samples out of these nine samples were exposed to ozone gas in the quartz reactor under a different period, such as 1, 5 and 10 seconds, to observe the time effect on the quantity of oxidized amount in the methanol solvent. The results show that by increasing the oxidation

time from 1 to 5 seconds, the oxidized amount (diphenylamine) was increased from 46.64 ppm to 55.7 ppm. However, with further increases in oxidation time, such as 10 seconds, the oxidized amount declined to 51.33 ppm. Hence it was observed that the optimum combination of sample exposure time under the ozone and the accuracy of the standard method to calibrate the concentration of methanol and diphenylamine are vital to identify the oxidized amount accurately.

CONCLUSION

We have demonstrated the potential of ozone sterilization, intending to reuse the N95 mask at a lower price and counter the shortage of the facemask across the globe. The quantitative analyses have confirmed the ozone's effective utilization as an oxidant to damage organic components present in the food colours. When ozone gas was passed from the sample, the flow configuration in the quartz reactor demonstrated excellent performance to sterilize the colour samples. However, careful handling of the reactor, such as to protect the ozone leakage, is vital to protect the health and environmental damage. In the second part, a colourless organic compound, diphenylamine, was successfully oxidized with ozone gas. An amine bonded with two phenyl groups completely turned yellow once oxidizes with ozone gas. A spectrometric characterization with the aid of a standard calibration method based on lower concentration (from 10 to 100 ppm) was used to quantify the oxidized amount in the methanol solvent accurately. It was observed that the standard method's accurate concentration and sample oxidation time are vital to analyze and quantify the oxidized amount correctly.

ACKNOWLEDGEMENTS

The authors are indebted to the Ministère de l'Economie et de l'Innovation (MEI) du Québec (project No. 39096) and KWI polymers for funding this project. We gratefully acknowledge: J. Blanchard, E Gilbert-Chouinard and S. N. Ardeh for the technical support.

REFERENCES

1. N95 Respirators, Surgical Masks, Face Masks, and Barrier Face Coverings | FDA Available online: ol/ n95- respi rators- and- surgi cal- masks- face- masks (accessed on Oct 9, 2021).
2. Schwan J, Alva TR, Nava G, Rodriguez CB, Dunn ZS, Chartron JW, Morgan J, Wang P, Mangolini L. Efficient facemask decontamination via forced ozone convection. *Sci Reports* 11:12263 (2021)
3. *ISS Working Group on Biocides*. Interim recommendations on cleaning and disinfection of non-healthcare settings during COVID-19 health emergency: Surfaces, indoor environments and clothing. In Rapporto ISS COVID-19; Rome, Italy, 2020.
4. Manjunath SN, Sakar M, Katapadi M, Geetha Balakrishna R. Recent case studies on the use of ozone to combat coronavirus: Problems and perspectives. *Environ Technol Innov* 21:101313 (2021)
5. REGULATION (EU) 2016/ 425 OF THE EUROPEAN PARLIAMENT AND OF THE COUNCIL - of 9 March 2016 - on personal protective equipment and repealing Council Directive 89/ 686/ EEC.
6. Cai C, Floyd EL. Effects of Sterilization With Hydrogen Peroxide and Chlorine Dioxide Solution on the Filtration Efficiency of N95, KN95, and Surgical Face Masks. *JAMA Netw Open* 3:e2012099–e2012099 (2020)
7. Rubio-Romero JC, Pardo-Ferreira MDC, Torrecilla-García JA, Calero-Castro S. Disposable masks: Disinfection and sterilization for reuse, and non-certified manufacturing, in the face of shortages during the COVID-19 pandemic. *Saf Sci* 129:104830 (2020)
8. Manning EP, Stephens MD, Patel S, Dufresne S, Silver B, Gerbarg P, Gerbarg Z, Cruz CD, Sharma L. Disinfection of N95 Respirators with Ozone. *medRxiv* **2020**, 2020.05.28.20097402, doi:10.1101/2020.05.28.20097402.
9. Merks P et al. Ozone disinfection of community pharmacies during the COVID-19 pandemic as a possible preventive measure for infection spread. *Medycyna Pracy* 2021:72 (2021)
10. Xu XW, Wu XX, Jiang XG, Xu KJ, Ying LJ, Ma CL, Li SB, Wang HY, Zhang S, Gao HN, et al. Clinical findings in a group of patients infected with the 2019 novel coronavirus (SARS-Cov-2) outside of Wuhan, China: retrospective case series. *BMJ* 368:m606 (2020)
11. Grignani E, Mansi A, Cabella R, Castellano P, Tirabasso A, Sisto R, Spagnoli M, Fabrizi G, Frigerio F, Tranfo G. Safe and Effective Use of Ozone as Air and Surface Disinfectant in the Conjuncture of Covid-19. *Gases 1*, 1:19–32 (2020)
12. Rutala WA, Weber DJ. Guideline for Disinfection and Sterilization in Healthcare Facilities, 2008.
13. Tseng CC, Li CS. Ozone for Inactivation of Aerosolized Bacteriophages. *Aerosol Sci Technol* 40:683–689 (2006)
14. Gorito AM, Pesqueira JFJR, Moreira NFF, Ribeiro AR, Pereira MFR, Nunes OC, Almeida CMR, Silva AMT. Ozone-based water treatment (O3, O3/UV, O3/H2O2) for removal of organic micropollutants, bacteria inactivation and regrowth prevention. *J Environ Chem Eng* 9:105315 (2021)
15. Rojas-Valencia MN. Research on ozone application as disinfectant and action mechanisms on wastewater microorganisms. **2012**.
16. Dennis R, Pourdeyhimi B, Cashion A, Emanuel S, Hubbard D. Durability of Disposable N95 Mask Material When Exposed to Improvised Ozone Gas Disinfection. *J Sci Med* 2:37 (2020)
17. Hudson JB, Sharma M, Vimalanathan S. Development of a Practical Method for Using Ozone Gas as a Virus Decontaminating Agent. *Ozone Sci Eng* 31:216–223 (2009)

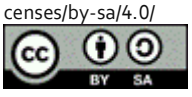

CSChE Systems & Control Transactions

Open Access | Original Research

Conference Proceedings
Canadian Chemical Engineering Conference 2021
October 24-27, Montréal, Québec, Canada

PSEcommunity.org/LAPSE:2021.0790

PSE PRESS

A Study of Factors Affecting Iron Uptake from a Functionalized Hibiscus Beverage

Ade. O. Oyewole* and Levente L. Diosady

University of Toronto, Department of Chemical Engineering and Applied Chemistry, Toronto, Ontario, Canada
* Corresponding Author: folake.oyewole@mail.utoronto.ca

ABSTRACT

Iron deficiency accounts for over 50% of the world's anaemia burden and it is widely prevalent in low- and middle-income countries. In response to the menace of iron deficiency in Sub-Saharan Africa, a commonly consumed beverage, the vibrantly red aqueous extract of the calyces of Hibiscus sabdariffa, has been functionalized. To determine the conditions that could potentially result in the most iron uptake by consumers of the functional beverage, the present study evaluated the effect of the factors that could influence the bioaccessibility of its iron content in the gastrointestinal (GI) tract.

Hibiscus beverage was fortified to contain, 6 mg iron per 250 mL of the beverage, by adding O.358 mM solution of ferrous sulphate salt to top up the native iron content determined to be 0.93±0.19 mg/ 250 mL. Also, a competing chelating agent - disodium EDTA was added to increase the bioaccessibility of iron from the beverage. Previous results showed the feasibility of releasing iron from the iron-polyphenol complex formed during the digestion of plant "foods", with the addition of disodium EDTA.

The effect of changes in pH values of the beverage, to mimic different parts of the GI tract (pH 1.5 to 7.5 in incremental steps of 1), on the iron-polyphenol complex formed and the release of the iron with added disodium EDTA was investigated. Next, the molar concentration ratio of the iron to disodium EDTA was varied at 1:0, 1:1, 1:2 and 1:3 to evaluate the effect of the concentration of the competing chelating agent on the quantity of iron that was released. Absorbance peaks at 550 nm, corresponded to the iron-polyphenol complex formed. Complex formation that occurs at elevated pH was reduced by added disodium EDTA, indicating iron release, which made iron more bioaccessible. A 1:2 molar ratio of EDTA to iron gave the optimum increase in iron bioaccessibility from the Hibiscus beverage.

Keywords: iron deficiency, *Hibiscus sabdariffa*, iron bioaccessibility

Date Record: Original manuscript received October 21, 2021. Published October 21, 2021.

INTRODUCTION

Iron deficiency (ID) remains a very common nutritional deficiency around the world [1], and its prevalence is widespread among many vulnerable groups including children under the age of 5 and women of reproductive age, particularly those in low- and middle-income countries (LMICs) [1] [2] [3]. ID is a leading cause of anemia, it accounts for 50% of anemia cases globally [1] and in 2019, the prevalence of anemia worldwide was reported to be 22.8% (about 1.74 billion people) with Western and Central Sub-Saharan Africa (SSA) as well as South Asia regions baring most of the burden [4] [5]. This suggests that to meet the Global Nutrition Target 2: halve the prevalence of anemia among vulnerable groups by 2025 [4], there must be targeted interventions within these high-burden regions. Consequently, the target population for this study is Sub-Saharan Africa, more so because groups vulnerable to IDA remain disproportionately represented within the region and by extrapolation these numbers are only expected to grow over the years [3] [6].

The effects of iron deficiency anemia (IDA) on affected populations can be quite devastating, both IDA and ID are leading contributors to the global disease burden [2]. The consequences of ID and IDA include impaired cognitive development in children, unwanted pregnancy outcomes, higher incidences of infant and maternal mortality and decreased physical and mental work capacity which have serious implications on the economic situation of families and populations [2] [7] [8].

Among every population group, inadequate dietary iron intake has been identified as a primary cause for ID [9] however, in LMICs the prevalence of ID can also be attributed in part to reduced iron uptake from their predominantly plant-based diet [3] [8]. This diet is characterized by low iron absorption/ low iron bioaccessibility owing to the presence of inhibitors like phytates and polyphenols which are reportedly

abundantly present in the plants [9] that are the major ingredients in their staple foods. These inhibitors form chelation complexes with the non-heme iron associated with plant-food sources which makes them unavailable to be absorbed by the body [10]. Therefore, to successfully address the prevalence of ID and IDA in Sub-Saharan Africa, a region made up of LMICs, there is a need to tackle both issues: inadequate dietary iron intake and reduced iron uptake stemming from the dependence of most of the population on plants as their primary food source.

The Copenhagen consensus declared the fortification of stable foods as the most cost-effective strategy to curb the prevalence of micronutrient deficiencies in LMICs and thus improve the economies of these countries [11]. Consequently, there are many studies and interventions that have focused on addressing the challenge of inadequate dietary iron intake to combat ID and IDA through the large-scale fortification of staple foods in Sub-Saharan Africa [7] [12] [13]. There are also some studies that have focussed on increasing iron uptake from plant-based staple foods consumed within the region though most were not large-scale ID/ IDA interventions. However, there are very few studies that have focused on both inadequate iron intake and reduced iron uptake from these staple foods specifically for large-scale ID/IDA interventions in Sub-Saharan Africa [13]. In response therefore, the overarching objective of this study is to functionalize a Sub-Saharan African staple food so that it can provide 30% of the recommended daily allowance (RDA) for women of reproductive age: 18 mg/day, to consumers and ensure also that the iron in the food is bioaccessible during digestion.

Indeed the epidemiology of IDA within the Sub-Saharan African context is particularly unique due to factors such as overpopulation, dietary preferences, poor infrastructure, limited resources, conflict, HIV and limited access to health services which predisposes the region to this deficiency, other micronutrient deficiencies and indeed all forms of malnutrition [3] [6] [14] [15]. Consequently, as recommended in the report of an expert workshop – Iron for Africa in 2017, iron fortification initiatives which are adapted to the local context and consumption patterns of the targeted population groups could be a more successful approach to reduce the prevalence of ID within the region [15]. For this study, a commonly consumed beverage in Sub-Saharan Africa, the bright red aqueous extract of the calyces of Hibiscus sabdariffa, is considered for its potential as a viable, logical, and sustainable intervention strategy to cover gaps in other iron fortification initiatives within the target region.

The Food Vehicle

Hibiscus sabdariffa plant which is also known as roselle, is believed to be indigenous to West Africa but it can be found in many countries in the tropical and sub-tropical regions of the world [16] [17]. Recently, the plant has gathered some interest because of its economic potential, since almost every part of the plant is useful [17]. The calyces are considered its most useful part with beneficial products including food colorants, jellies, juices, and jam [17] [18]. The cold beverage which is extracted from the calyces is regarded as a staple in homes in many countries in Sub-Saharan Africa as well as other tropical countries [17] [19], it is also commercially produced as a substitute to conventional beverages because of its refreshing taste and the recent high demand for natural products [18]. The plant parts have demonstrated medicinal and nutritional characteristics [18] [19], and have even been considered as a potential source of iron to fight ID and IDA [20] [21]. However, like many of the staple foods in SSA, Hibiscus sabdariffa has also been reported to have iron inhibitors inherently present within it, the plant is rich in polyphenols which also impart therapeutic benefits to the plant [19] [22]. Consequently, the process of functionalizing the Hibiscus beverage offers an opportunity to address the two factors that were highlighted earlier as contributors to the prevalence of ID and IDA in Sub-Saharan Africa: low iron intake and reduced iron uptake from plant food sources. Furthermore, this process could then be adapted/adopted to fortify other plant-based foods that are rich in polyphenols with iron.

The Strategy

The Hibiscus beverage was functionalized by fortification to provide 6 mg/day of iron which is 30% of the targeted iron RDA of 18 mg/day. Thereafter, the beverage's functionality was further enhanced by increasing the bioaccessibility of its iron content (iron uptake). Some earlier studies reported an increase in iron bioaccessibility after a competing chelator was introduced into a fortified plant-food system [23], however, in these studies the focus was on the prevention of iron-phytate chelation complex formation not iron-polyphenol chelation complex formation. In a comparable study to the present study, McGee and Diosady (2017) demonstrated the effectiveness of using a competing chelator, disodium EDTA (Na_2EDTA), to increase the iron uptake from an iron fortified black tea with a very high polyphenolic content [10]. A similar approach is adopted in this study, however, in this study added iron as well as native iron are considered. Specifically, the objective in this paper is to study the factors that might influence iron uptake form the functionalized Hibiscus beverage system.

MATERIALS AND METHODS

Materials

Plant Samples

Hibiscus sabdariffa calyces were sourced from the National Horticultural Research Institute, Ibadan, Oyo State, Nigeria. Samples were air dried and milled from source, they were then kept in airtight containers pending use.

Reagents and Chemicals

For this study, unless otherwise stated, all chemicals used were reagent grade. The competing chelator, disodium EDTA, was purchased from BioShop Canada Inc. (Burlington Ontario, Canada). The gallic acid used for the model reaction and the fortificant, ferrous sulphate heptahydrate, were purchased from Sigma-Aldrich Canada Co. (Oakville Ontario, Canada). For pH adjustments, sodium hydroxide and hydrochloric acid (1N) were purchased from Caledon Laboratories (Caledon Ontario, Canada) and BioShop Canada Inc. (Burlington Ontario, Canada) respectively. Reverse osmosis purified (RO) water was used for all experiments.

Methods

Hibiscus Calyces Extraction Process

The following procedure had previously been confirmed by benchmarking as one that produced a sample closest in consistency and taste to a commercially available Hibiscus beverage in Nigeria, West Africa. Briefly, to make a 100 mL of the beverage, 12.5 g of the dried and milled calyces was dispersed in 87.5 mL of reverse osmosis (RO) water. Next, the mixture was brought to a boil in about 30 minutes. The sample was allowed to cool down before straining using a 3-inch mini-strainer. Collected samples were then vacuum filtered using a vacuum filtration setup which included a 250 mL Pyrex Buchner flask, a porcelain Buchner funnel to hold 11 mm filter papers and a set of filter cones to create an airtight sealed connection between the flask and the funnel. Filtrates were made up to 100 mL with RO water in a volumetric flask. Using a VWR scientific model 8000 pH meter the pH value of the Hibiscus beverage was determined to be 2.62± 03. The beverage samples were stored in a refrigerator pending analysis.

Iron Fortification by Direct Mixing

To meet the target of supplying 30 % of the recommended daily allowance (RDA) of iron for women of reproductive age, 6 mg was achieved by adding 5 mg (0.358 mM) of ferrous sulphate heptahydrate to in 250 mL of the beverage, since the Hibiscus extract naturally contained ~4 mgL^{-1} iron (~0.07 mM).

Iron-Polyphenol Complex Quantification

Adapting a traditional colorimetric assay test for phenolic compounds - the ferric chloride test [24], a Tecan infinite 200 pro microplate reader was used to measure the absorbance of prepared samples. NaOH and HCl (if required) were used to adjust all samples to pH 6.5 ± 0.2 to mimic the pH of the site of iron absorption in the small intestine. The absorption was scanned between 400 nm and 800 nm and the absorption of the iron-polyphenol complex peak was measured at 542 nm to 561 nm [25]. Iron-complex calibration curves were generated by preparing standards with a gallic acid concentration of 0.3 g/L to match the phenolic content of the beverage. Standards were adjusted to pH 6.5 ± 0.2.

There were 2 sets of samples, and each set of experiments was performed in triplicates.

Hibiscus beverage pre-fortification

Net absorbances were calculated by zeroing using water as a blank, and ferrous sulphate heptahydrate (used in place of ferric chloride) concentrations of from 0.01 mM to 0.05 mM in steps of 0.01 mM.

Fortified Hibiscus beverage

Similarly, a calibration curve was prepared using 0.1 M - 0.5 M in steps of 0.1 M, to encompass the expected concentration of 0.428 mM. iron in the beverage after fortification.

Effect of Different Na_2EDTA Concentrations on Iron Bioaccessibility

Previously, it had been demonstrated that disodium EDTA is able to release iron from the iron-polyphenol complex, making the iron available for absorption into the bloodstream, where it can potentially influence the iron status of the body. The effect of different concentrations of this competing chelator on the bioaccessibility of iron in the Hibiscus beverage was investigated.

Briefly, two sets of experiments were carried out as follows: aliquots of samples of the Hibiscus beverage before and aliquots of samples of the beverage after fortification were spiked separately with four different concentrations of Na_2EDTA salt to give final iron to Na_2EDTA molar concentration ratios 1:1, 1:2, 1:3 and 1:4.

For Hibiscus beverage with no added iron, the final concentrations of NA_2EDTA in the different aliquots were 0.07 mM, 0.14 mM, 0.21 mM and 0.28mM, while for the fortified beverage, the final NA2EDTA concentrations for the aliquots were 0.43 mM, 0.86 mM, 1.28 mM and 1.71 mM. Samples were analysed as described above.

From the absorbance scans generated, the effect of varying the concentration of the competing chelator – disodium EDTA on the iron-polyphenol peaks was evaluated.

Effect of pH Variation on Iron Bioaccessibility

Another factor of interest is the effect of pH on the bioaccessibility of iron in the beverage, as an indication of iron bioavailability in the GI tract

Four different samples were prepared, unfortified Hibiscus beverage, unfortified Hibiscus beverage with added disodium EDTA (x3 the molar concentration of the native iron), fortified Hibiscus beverage and fortified beverage with added disodium EDTA (x3 the molar concentration of the total iron content). The pH of an aliquot of each sample was sequentially adjusted using 0.1N NaOH, 1N NaOH, 0.1N HCl and 1N HCl as needed to a preselected pH between 1.5 and 7.5 in steps of 1. A Tecan infinite 200 pro microplate reader was used to measure the absorbance of each aliquot at 550nm. The absorbance of the unadjusted aliquot sample was also determined. The absorbance data were used to estimate the bioaccessibility of iron across the digestive system.

RESULTS AND DISCUSSION

Iron-Polyphenol Complex Quantification

Figures 1a. and 1b. below are samples of the absorbance scans of the unfortified Hibiscus beverage and the fortified Hibiscus beverages.

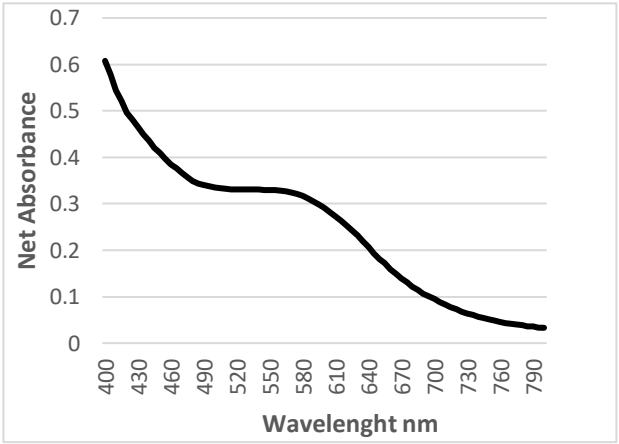

Figure 1a.: A sample absorbance scan of unfortified hibiscus beverage at pH 6.5

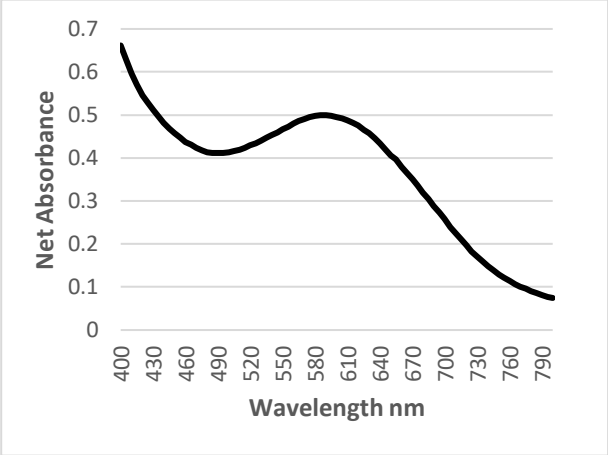

Figure 1b.: A sample absorbance scan of fortified hibiscus beverage at pH 6.5

The peak in Figure 1b. is more pronounced than the peak in Figure 1a. and this could be explained by the fact that the fortified beverage would have more of the iron-polyphenol complex formed than the unfortified beverage. Notably, there was a slight shift of the peak of the fortified beverage which only occurred after the absorbances were zeroed, however, this was similar to what was reported in a previous study [26]. A more simplified and direct form of the method developed by McGee (2018) was used to estimate quantities of the iron-polyphenol complexes formed by both the native and added iron: ferrous sulphate heptahydrate.

Using the calibration curves generated, as a measure of their absorbances, estimates of the iron-polyphenol complexes formed in 3 different samples of each beverage were reported as ferrous sulphate in gallic acid equivalents (mM Fe_2SO_4/GAE), see Table 1a. and Table 1b. below:

Table 1a: Iron-polyphenol complexes formed in Hibiscus beverage (pre-fortification)

Sample	Net Absorbance at 550nm	Iron-polyphenol Complex (mM Fe2SO4/GAE)
1.	0.3121	0.1829
2.	0.3363	0.1970
3.	0.3382	0.1981

Table 1b: Iron-polyphenol complexes formed in fortified Hibiscus beverage

Sample	Net Absorbance at 550nm	Iron-polyphenol Complex (mM Fe2SO4/GAE)
1.	0.5178	0.3118
2.	0.4452	0.2684
3.	0.4566	0.2752

The estimated values recorded in Table 1a. are well above the expected range of 0.07mM for the native iron, this suggests that there are other interactions besides the iron-polyphenol complex which also occur within the targeted wavelength range: 542 nm to 561 nm. However, the values recorded for the fortified beverage are much closer to the expected value of 0.358 mM, these estimates also suggest that since well over two thirds of the added iron is bound in the complex the iron would not be available for absorption. This further supports the need to prevent the interaction between iron and polyphenols. The readings for both beverages were recorded at the same wavelength to allow for better comparison.

Effect of Different Na_2EDTA Concentrations

The absorbances of both set of samples at a pre-selected wavelength of 550nm were used to generate Figures 2a. and 2b.

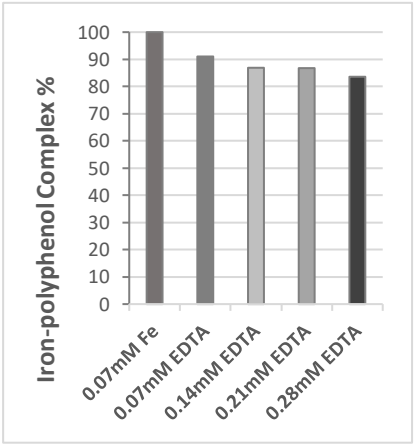

Figure 2a.: Relative percentages of iron-polyphenol complexes in Hibiscus beverage pre-fortification

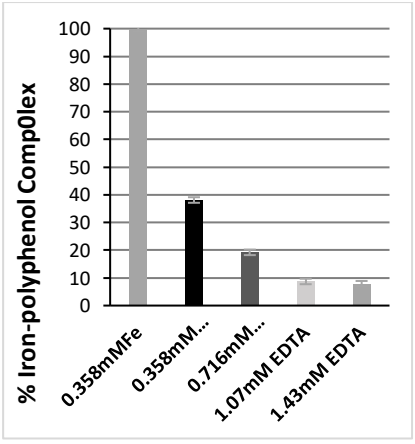

Figure 2b.: Relative percentages of iron-polyphenol complexes in Fortified Hibiscus beverage

Figure 2a. illustrates the effect of spiking the unfortified Hibiscus beverage sample with Na_2EDTA incrementally (1:0; 1:1; 1:2; 1:3 and 1:4). From this figure the most significant drop in the relative percentage of the iron-polyphenol complex present in the samples was at the molar ratio 1:1, thereafter, the drop, which represents iron release, wasn't as significant. It can also be inferred that by the molar concentration ratio: 1:2, equivalent to about 87%, most of the iron to be released had been released, the ratios 1:3 and 1:4 were equivalent to approximately 87% and 84% respectively.

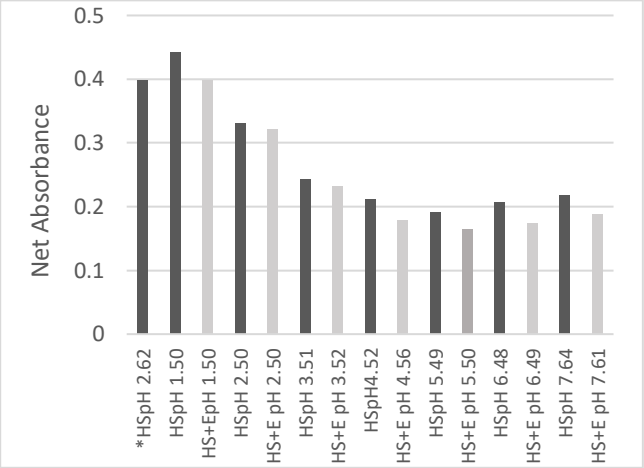

Figure 3a.: Absorbances of unfortified Hibiscus beverages with/without NA_2EDTA due to sequential pH variation at 550nm

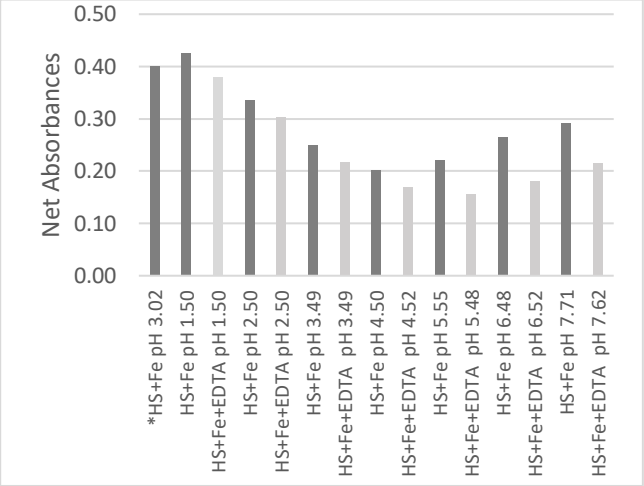

Figure 3b.: Absorbances of fortified Hibiscus beverage with/without Na2EDTA due to sequential pH variation at 550nm

The percentage of iron released is not as high as expected, with only 16% of the iron seemingly made bioaccessible. However, it must be recalled that earlier, it had been suggested that the model being adopted for this study might not accurately quantify the interaction between the native iron present in the beverage and the plant polyphenols. All estimated values are based on the assumption that the only interaction present is that between the native iron and polyphenols.

Figure 2b. shows a more promising result. After the initial spike, only at ratio 1:1, there was already a 62% decrease in the iron-polyphenol complex present which means a lot of iron is more bioaccessible. A continued increase in the molar concentration of Na_2EDTA produced further peak drops. However, from the figure, it can be inferred the relationship is not linear. From Figure 2b, it can also be seen that by adding Na_2EDTA it is possible to release up to 90% of the iron previously bound as iron-polyphenol complexes in the fortified beverage, suggesting that most of the added iron would be more bioaccessible.

Effect of Different Na_2EDTA Concentrations

As earlier stated, understanding the dependence of iron biocessibility is pertinent as this gives some insight into how the iron and the complexes formed might behave in the GI tract.

Figures 3a. and 3b. show a similar trend for both the fortified and unfortified beverage, including an obvious increase in absorbance after the pH value is dropped to 1.5. Thereafter a steady decrease is seen in the absorbances of all four samples within the more acidic pH range. Reportedly, a less acidic environment promotes the formation of iron-polyphenol complexes [10] [25] so it can be inferred that at the lower pH range, 1.5 – 4.5, the absorbances recorded are not as a result of iron-polyphenol complex formation. However, it is worth further investigation to know if the other interactions observed still influence the bioaccessibility of iron. The effect of disodium EDTA is more obvious in the less acidic range suggesting that it can compete more favorably for the iron within this range therefore, by inference, it would influence the bioaccessibility of iron better in this pH range: 5.5-7.5. Also, interestingly both graphs record similar absorbance values until they get to pH 5.5 which might suggest that the added iron doesn't contribute to whatever is happening in the lower pH range.

CONCLUSION

An increase in iron uptake is important to curb the prevalence of ID and IDA in Sub-Saharan Africa because majority of the populace are dependent on a plant-based diet. Therefore, there is the need to develop strategies that are sustainable within the Sub-Saharan African context as well as strategies that could possibly contribute to improving the iron status of the populace, particularly the most vulnerable to ID and IDA.

Functionalizing *Hibiscus sabdariffa* beverage has the potential to fill a gap yet to be filled by other iron-food fortification initiatives targeted at the Sub-Saharan African population. The study of the factors that influence the bio-accessibility of both the native and added iron, ferrous sulphate heptahydrate, has offered a technical understanding of how to prevent the inhibiting actions of the polyphenols inherently present in the Hibiscus beverage on its iron content.

Disodium EDTA added in excess relative to the iron content of the Hibiscus beverage has demonstrated promising results for improving iron bioaccessibilility. The 1:2 molar concentration ratio of iron to the competing chelator releases most of the iron previously bound in the iron-polyphenol complex formed, thus it provides the iron in an absorbable form at the site of iron absorption, the small intestine, during digestion. More statistical studies would be required to state this categorically, but this conclusion confirms the previous findings of McGee and Diosady.

The findings of the pH dependence of the bioaccessibility of the iron as the beverage travels through the GI tract provides information on future work to make the beverage more functional as a viable iron source for the target population.

ACKNOWLEDGEMENT

We appreciate the sponsors of this project, the Schlumberger Faculty for the Future Foundation.

REFERENCES

1. Black MM. Micronutrient Deficiencies and Cognitive Functioning. *J Nutrition* 133:3927S-3931S (2003)
2. Pasricha SR, Tye-Din J, Muckenthaler MU, Swinkels DW. Iron deficiency. *Lancet* 397:233-248 (2021).
3. Mwangi MN, Mzembe G, Moya E, Verhoef H. Iron deficiency anaemia in sub-Saharan Africa: a review of current evidence and primary care recommendations for high-risk groups. *Lancet Haema* 8:e732-e743 (2021).
4. Gardner W, Kassebaum N. Global, Regional, and National Prevalence of Anemia and Its Causes in 204 Countries and Territories, 1990–2019. *Current Developments in Nutrition* 4:830 (2020)
5. Owais A, Merritt C, Lee C, Bhutta ZA. Anemia among Women of Reproductive Age: An Overview of Global Burden, Trends, Determinants, and Drivers of Progress in Low- and Middle-Income Countries. *Nutrients* 13: 2745 (2020)
6. Fanzo J. The Nutrition Challenge in Sub-Saharan Africa. UNDP Africa Policy Notes 2012-012, United Nations Development Programme, Regional Bureau for Africa. (2012)
7. Darnton-Hill I, Neufeld L, Vossenaar M, Osendarp S, Martinez H. Large-scale food fortification: an overview of trends and challenges in low- and middle-income countries in 2017. *Micronutrient Forum*
8. Khoja KK, Aslam MF, Sharp PA, Latunde-Dada GO. In vitro bioaccessibility and bioavailability of iron from fenugreek, baobab and moringa. *Food Chem* 335: 127671 (2020)
9. Food and Agriculture Organization of the United Nations, "Human Vitamin and Mineral Requirements," (2001).
10. McGee EJT, Diosady LL. Prevention of iron-polyphenol complex formation by chelation in black tea. *LWT-Food Sci Technol* 89:756-762 (2017)
11. Horton S, Mannar V, Wesley A. Micronutrient Fortification (Iron and Salt Iodization) (2009)
12. Osendarp SJM, Martinez H, Garrett GS, Neufeld LM, De-Regil LM, Vossenaar M, Darnton-Hill I. Large-Scale Food Fortification and Biofortification in Low-and Middle-Income Countries: A Review of Programs, Trends, Challenges, and Evidence Gaps. *Food and Nutrition Bulletin* 39:315-331 (2018)
13. Ohanenye IC, Emenike CU, Mensi A, Medina-Godoy S, Jin J, Ahmed T, Sun X, Udenigwe CC. Food fortification technologies: Influence on iron, zinc and vitamin A bioavailability and potential implications on micronutrient deficiency in sub-Saharan Africa. *Scientific African* 11:e00667 (2021)
14. Bain LE, Awah OK, Ngia G, Kindong NP, Sigal Y, Nsah B, Tanjeko AT, Malnutrition in Sub - Saharan Africa: Burden, causes and prospects. *Pan African Medical Journal* 15:120 (2013)
15. Mwangi MN, Phiri KS, Abkari A, Gbané M, Bourdet-Sicard R, Braesco VA, Zimmermann MB, Prentice AM. Iron for Africa—Report of an Expert Workshop, *Nutrients* 9:576 (2017)
16. Nguyen QV, Hoang C. Processing of Herbal Tea from Roselle (Hibiscus sabdariffa L.): Effects of Drying Temperature and Brewing Conditions on Total Soluble Solid, Phenolic Content, Antioxidant Capacity and Sensory Quality. *Beverages* 6:2 (2020)
17. Abou-Arab AA, Abu-Salem FM, Abou-Arab EA. Physico-chemical properties of natural pigments (anthocyanin) extracted from Roselle calyces (*Hibiscus subdariff*a). *J Amer Sci* 7:445-456 (2011)
18. Salami SO, Afolayan AJ. Suitability of Roselle-*Hibiscus sabdariffa L*. as Raw Material for Soft Drink Production. *Journal of Food Quality* 2020:8864142 (2020).
19. Sáyago-Ayerdi SG, Arranz S, José S, I. Goñi I. Dietary Fiber Content and Associated Antioxidant Compounds in Roselle Flower (*Hibiscus sabdariffa L.)* Beverage. *J Agric Food Chem* 55:7886–7890 (2007)
20. Peter EL, Rumisha SF, Mashoto KOMOM, Mfinanga S. Efficacy of standardized extract of *Hibiscus sabdariffa L.* (*Malvaceae*) in improving iron status of adults in malaria endemic area: A randomized controlled trial. *Journal of Ethnopharmacology* 209:288-293 (2017).
21. Kubuga CK, Hong HG, Song WO. *Hibiscus sabdariffa* Meal Improves Iron Status of Childbearing Age Women and Prevents Stunting in Their Toddlers in Northern Ghana. *Nutrients* 11:198 (2019)
22. Bergmeier D, Berres PHD, Filippi D, Bilibio D, Rodrigo V, Bettiol PWL. Extraction of total polyphenols from hibiscus (*Hibiscus sabdariffa L*.) and waxweed / 'sete-sangrias' (*Cuphea carthagenensis*) and evaluation of their antioxidant potential. *Acta Scientiarum. Technology* 36:545-551 (2014)
23. WHO/ FAO, Guidelines on food fortification with micronutrients, B. d. B. O. D. R. H. L. Allen, Ed., 2006.
24. Pavia DL, Lampman GM, Kriz GS, Engel RG, A microscale approach to organic laboratory techniques, Fifth, Ed., Belmont, CA: Brooks/Cole (2013)
25. Perron NR, Wang HC, DeGuire SN, Jenkins M,. Lawson M, Brumaghim JL. Kinetics of ironoxidation upon polyphenol binding. *Dalton Trans* 39:9982-9987 (2010)
26. McGee EJT, Diosady LL. Development of Spectrophotometric Quantification Method of Iron-Polyphenol Complex in Iron-Fortified Black Tea at Relevant pH Levels. *Food Analytical Methods* 11:1645–1655 (2018)

This conference proceeding has not been peer reviewed.

CSChE Systems & Control Transactions

Open Access | Original Research

Conference Proceedings
Canadian Chemical Engineering Conference 2021
October 24-27, Montréal, Québec, Canada

PSEcommunity.org/LAPSE:2021.0791

PSE PRESS

Lessons Learned from Three Decades of Global Automation Experience Across Five Industries

Lane Desborough

Nudge BG, Inc., Thousand Oaks, California, USA Lane@NudgeBG.com

ABSTRACT

My current work on Automated Insulin Delivery (the so-called "artificial pancreas") directly benefits from two decades of experience gained implementing and remotely monitoring automation in complex and challenging industrial cyberphysical systems all over the world; systems upon which society depends. This talk will cover topics including experimentation, modeling, simulation, and outcome measure sample statistics, as well as controller design considerations including human factors, objective functions, and final control element challenges.

Keywords: automated insulin delivery, artificial pancreas, diabetes

Date Record: Original manuscript received October 20, 2021. Published October 21, 2021

INTRODUCTION

In 1921 insulin was discovered by Banting, Best, Collip, and Macleod at the University of Toronto. For the first time, a diabetes diagnosis was not a death sentence; people with insulin-requiring diabetes (all people with Type 1 Diabetes and some people with Type 2 Diabetes) were able to control this incurable condition by injecting insulin to lower their blood glucose.

In the intervening hundred years, insulin and its delivery methods, together with blood glucose sensing technology have made tremendous advances, however for people living with insulin-requiring diabetes a substantial cognitive burden remains: every few hours they must decide how much insulin to deliver to compensate for the myriad sources of variation in blood glucose – for their entire life.

In parallel, in the same intervening hundred years, automation has fundamentally transformed other domains including the continuous process and power generation industries.

If the purpose of control is to safely transfer variability from a place where it hurts (the controlled variable) to a place where it doesn't hurt as much (the manipulated variable) in order to make a human's job easier, then the majority benefit of automation these past hundred years has accrued to humans in industry, not humans with chronic diseases such as diabetes.

In the past decade, contemporary automation methods first developed for process automation have finally begun to be applied to the automation of insulin delivery. The so-called artificial pancreas holds great promise to reduce burden for those living with insulin-requiring diabetes.

LESSONS FROM INDUSTRIAL AUTOMATION

Early in my career I was fortunate to develop a strong academic and industrial foundation in process control from my supervisor Dr. Tom Harris at Queen's University and from my colleagues at Nova Chemicals Joffre Alberta, respectively.

From 1988 through 2010, I had the privilege of traveling all over the world to implement and remotely monitor automation at chemical plants, mines, oil refineries, paper mills, and power plants while employed at Honeywell and General Electric.

This diversity of experience exposed me to dozens of concepts, principles, methods, tools, and practices used to design, develop, implement, operate, and maintain automation (Table 1).

TYPE 1 DIABETES: A BROKEN LOOP

When our ten year old son was diagnosed with Type 1 Diabetes in 2009, I knew very little about the disease. I was shocked to learn that despite the availability of continuous glucose monitor (CGM) and insulin pump technology, the "loop" had not been closed. People with diabetes were performing open-loop control.

Our family quickly learned that management of insulin-requiring diabetes, while seemingly simple (one input, one output), is actually an incredibly complex interplay of algorithms, hardware, behaviors, and physiology (Figure 1).

adaptive control	control hazard analysis	hierarchical control	remote monitoring and diagnostics
advanced alarm management	control objective	high fidelity simulation	requirements management
alarm design	correlated observations	inferred properties	resilience engineering
alarm standards	coupling and complexity	interoperability i.e. OPAF, OPC	robust control
anomaly detection	cybersecurity	job task analysis	Operator role transformation
automated code generation	DevOps	lean / agile development	safety driven design i.e. STAMP
automated decision support	display guidelines	mode confusion	sensor issues
automation benchmarks	dynamic design of experiments	model-based design	sensor validation
automation trust	dynamic modeling	feedforward control	standards management
batch control	emergency shutdown systems	nonfunctional requirements	state estimation
behavioral economics	empirical modeling	nonlinear control	statistical process control
closed-loop identification	ethnography	operator training	systems engineering
configuration management	Firmware/software updating	performance monitoring	testing
constraint control	functional safety	procedural automation	valve cams, strapping tables
control algorithms (PID, MPC)	gain scheduling	real time optimization	wireless systems

Table 1: Proven concepts for controlling time varying, poorly modeled, complex, nonlinear, interacting stochastic systems

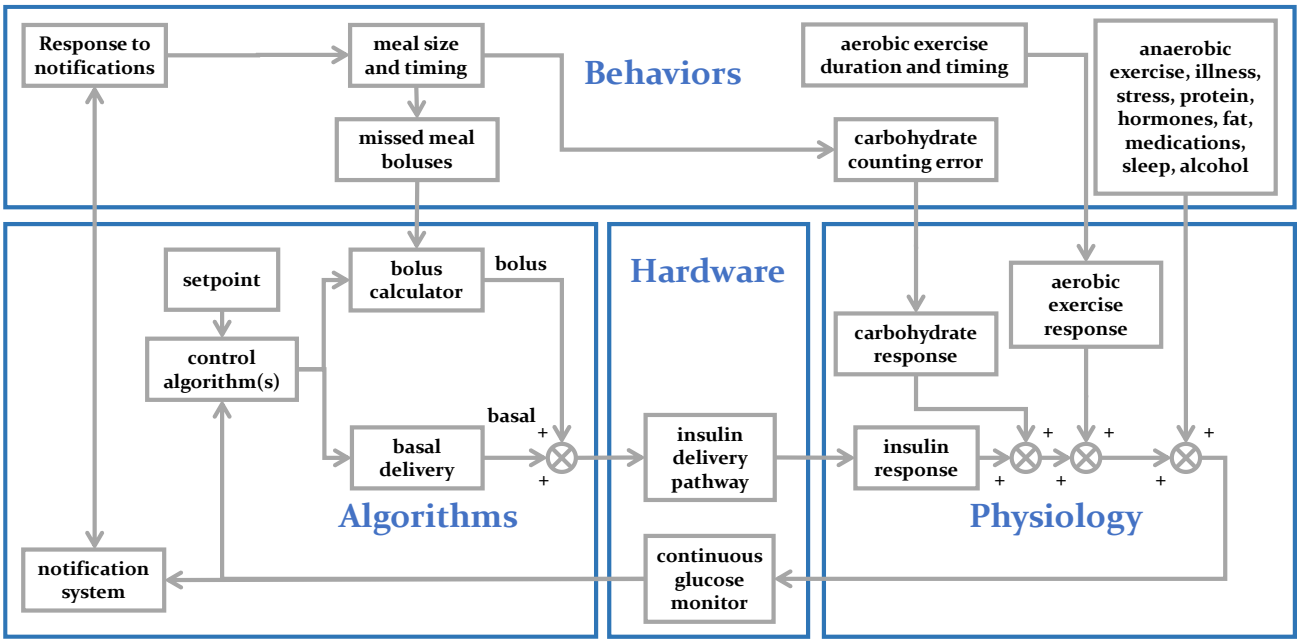

Figure 1. Automated Insulin Delivery: a complex interplay of algorithms, hardware, behaviors, and physiology

CONCLUSION AND RECOMMENDATION

Within months of my son's diagnosis I found myself at Medtronic Diabetes, leading the team responsible for commercializing Medtronic's next step towards automated insulin delivery (AID).

Twelve years and three companies later, I still believe that many of the challenges confronting AID have already been overcome in other domains. More work remains to apply the concepts in Table 1 to AID in order to reduce the burden for those who live with diabetes.

This conference proceeding has not been peer reviewed.

CSChE Systems & Control Transactions

Open Access | Original Research

Conference Proceedings
Canadian Chemical Engineering Conference 2021
October 24-27, Montréal, Québec, Canada

PSEcommunity.org/LAPSE:2021.0792

PSE PRESS

Detection and Diagnosis of Ring Formation in Rotary Lime Kilns

Lee D. Rippon[a]*, Barry Hirtz[b], Carl Sheehan[c], Travis Reinheimer[d], Cilius van der Merwe[d], Philip Loewen[e], and Bhushan Gopaluni[a]

[a] University of British Columbia, Department of Chemical and Biological Engineering, Vancouver, B.C., Canada
[b] Cool Cameras, Prince George, B.C., Canada
[c] Spartan Controls, Burnaby, B.C., Canada
[d] Canfor Pulp, Vancouver, B.C., Canada
[e] University of British Columbia, Department of Mathematics, Vancouver, B.C., Canada
* Corresponding Author: leeripp@chbe.ubc.ca

ABSTRACT

Rotary lime kilns are large-scale, energy-intensive unit operations that serve critical functions in a variety of industrial processes including cement production, pyrometallurgy, and kraft pulping. As massive expensive vessels that operate at high temperatures it is imperative from economic, environmental, and safety perspectives to optimize preventative maintenance and production efficiency. To achieve these objectives rotary kilns are increasingly outfitted with more sophisticated sensing technology that can provide additional operating insights. Although increasingly intricate data is collected from industrial operations the extent to which value is extracted from this data is often far from optimal. Our research aims to improve this situation by developing data analytics methods that leverage advanced industrial sensor data to address outstanding process faults. Specifically, this research investigates the use of infrared thermal cameras to detect and diagnose ring formation in rotary lime kilns. The formation of rings is described in literature as the most troublesome problem for lime kiln operation as it can severely limit production, cause millions of dollars in equipment damage, and lead to unplanned shutdowns. In this work we propose a strategy to detect and diagnose ring formation with industrial thermal camera data. While implementing this strategy with an industrial case study we develop a novel process visualization technique and obtain important process insights that enable better data collection. These contributions are presented in this work along with preliminary results from ring detection and diagnosis, ongoing challenges, and suggestions for future research directions.

Keywords: process monitoring, fault detection and diagnosis, data visualization, pulp and paper, rotary kiln

Date Record: Original manuscript received October 18, 2021. Published October 21, 2021

INTRODUCTION

As the digital transformation of industrial processes progresses it becomes increasingly important to develop application specific data analytics techniques that maximize the value extracted from process data. The global emergence of digitalization has placed data in a central role in modern society. The vital role of data has drawn increased attention to data analytics fields such as artificial intelligence, machine learning, and process systems engineering. This increased attention has manifested in process monitoring literature in the form of increasingly sophisticated fault detection and diagnosis algorithms. From traditional techniques such as principal component analysis (PCA) to advanced deep learning architectures such as generative adversarial networks (GANs), new state-of-the-art results are frequently published on popular simulated benchmarks such as the Tennessee Eastman process [1,2]. Unfortunately, in many industries the advances in process monitoring algorithms have not necessarily translated to increased uptake and successful implementation.

This research aims to develop and apply data analytics techniques to address a specific outstanding industrial fault, i.e., ring formation in rotary lime kilns. Ring formation is a significant industrial fault that contributes to immense economic and environmental losses. It deserves and has received attention in literature [3-5], but it has not received significant attention from the relevant data analytics communities, e.g., process monitoring [6]. By centering our data-driven investigation around a specific fault with real historical data we must directly address many of the practical constraints and implementation challenges. Fortunately, these challenges also provide opportunities to develop techniques for learning valuable process insights from the often-undervalued raw data [7].

In this paper we present the findings of our investigation into using historical process data to detect and diagnose ring formation in a rotary lime kiln. After providing process knowledge for context, we present our proposed approach for detecting and diagnosing ring formation. Data visualization and monitoring tools are developed to enhance our

investigation and obtain valuable process insights. Preliminary results reveal unique challenges associated with ring detection which inform enhanced data collection techniques and opportunities for future research.

BACKGROUND

The process monitoring techniques presented in this work are relevant to a variety of industries where rotary kilns collect real-time kiln shell temperature (KST) measurements along the length of the kiln. However, investigating ring formation requires specific domain knowledge so the remainder of this work will focus on a particular application, i.e., rotary lime kilns in the recovery circuit of kraft pulp mills. The rest of this section provides context into the role of the lime kiln in the recovery circuit, describes the problem of ring formation, and presents the available resources to help set the stage for our investigation.

Kraft Pulping and Rotary Lime Kilns

As Figure 1 illustrates, rotary lime kilns (outlined in red) are part of the larger integrated forest products industry. Pulp mills are a key component of the integrated forest products industry as the profitability of sawmills depends on revenue generated through selling chips to pulp mills [8]. The kraft pulping process relies upon a strong alkaline solution known as white liquor. Kraft pulp mills also rely on a recovery circuit to recover expensive chemicals (e.g., white liquor) and minimize their environmental impact. Central to chemical recovery is the recausticizing area which produces white liquor by reacting green liquor with slaked lime. This causticizing reaction produces lime mud as a by-product. The rotary lime kiln is essential for regenerating burnt lime from this lime mud [9].

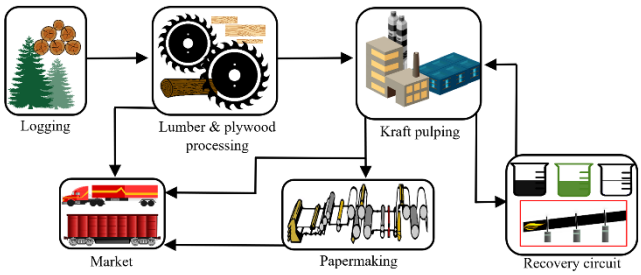

Figure 1. The role of the lime kiln (outlined in red) in the context of the integrated forest products industry.

Rotary lime kilns are massive cylindrical vessels consisting of a slightly inclined steel shell that can be over 100 m in length and over 4 m in diameter [10]. The steel shell is lined with protective refractory bricks, supported by external bracing, and rotated by a drive gear at roughly 1 rpm [9]. The kiln is responsible for converting calcium carbonate ($CaCO_3$) into calcium oxide (CaO) according to the following endothermic calcination reaction:

$$CaCO_3(s) \rightarrow CaO(s) + CO_2(g). \quad (1)$$

The calcination reaction proceeds at roughly 870°C [3]. As Figure 2 illustrates, wet lime mud ($CaCO_3$) enters the lime kiln where it dries into a powder in the drying zone before agglomerating into nodules in the preheating zone. The energy required for drying, preheating, and calcining the lime mud is provided by a burner flame at the bottom of the inclined shell. The burner often uses natural gas and is the largest source of fuel consumption in pulp manufacturing [11]. Given the high fuel demand and the nature of calcination the lime kiln is a very carbon intensive unit operation so there is a strong environmental motivation for minimizing production inefficiencies.

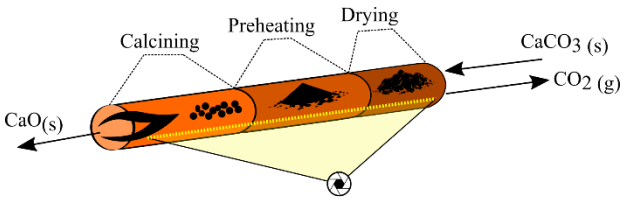

Figure 2. Simplified illustration of a rotary lime kiln with a thermal camera measuring shell temperatures.

Another detail illustrated in Figure 2 is the use of a thermal camera to provide real-time KST measurements along the length of the kiln. As thermal imaging technology has matured it has become less expensive while offering better performance and functionality. Consequently, kilns have become increasingly equipped with infrared cameras which are primarily used to monitor shell temperatures for potentially dangerous hot spots [12]. As more kilns are equipped with thermal cameras it becomes increasingly important to maximize the value extracted from this supplementary data. This work aims to leverage this data to address a major outstanding process fault that many kilns suffer from, i.e., the formation of rings.

Kiln Fouling and Ring Formation

Reaction materials flow through the kiln because of the slope and rotation speed of the kiln. Apart from a thin coating that is applied to the refractory during start-ups there should be no accumulation of material in the kiln. Fouling occurs when reaction material accumulates in the kiln. Two distinct types of fouling are shown in Figure 3, i.e., soda balls (left) and rings (right). Ring formation has been described in literature as the most troublesome problem for lime kiln operation [13]. Rings form when lime mud and product lime particles adhere to the refractory wall of the kiln and begin to accumulate. Although the exact mechanisms of ring formation are not completely understood, distinct types of rings have been observed and causal mechanisms have been proposed [3].

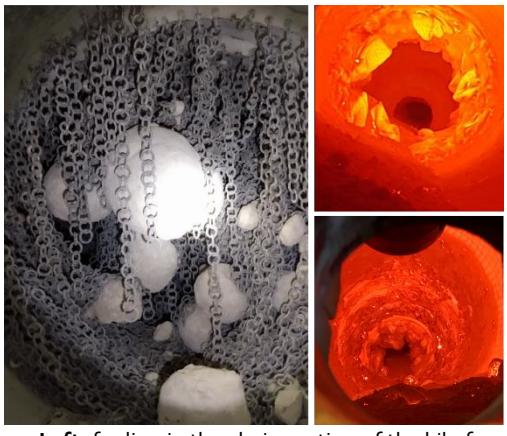

Figure 3. Left: fouling in the chain section of the kiln from soda balls. **Right:** two distinct cases of ring formation.

A survey of Swedish kraft pulp mills showed that approximately 70% of mills suffered from ring formation and many did not know why [14]. As rings grow, they can obstruct the flow of reaction materials in the kiln which can result in reduced production of lime. To compensate for this lost production mills must purchase fresh lime which can cost over $50,000 USD per day. In severe cases the rings can result in damage to the kiln refractory which can cost over $3 million USD per event [3]. Perhaps the costliest consequence of ring formation is that it can regularly lead to unscheduled downtime. Mills attempt to mitigate ring formation by using industrial shotguns to blast out the ring, thermal cycling to cause stress fractures, and adding water to the kiln to slake out the ring. These temporary measures can help prolong operation of a fouled kiln, but ultimately a full shut-down is typically required for someone to enter the kiln and use a pneumatic jack hammer to physically remove the ring.

Objectives and Available Resources

The objectives of this work are two-fold:

1. **Detect ring formation:** early onset detection of ring growth and decay. Estimating the extent and rate of ring formation to enable preventative maintenance and avoid refractory damage.
2. **Diagnose potential causes:** analyze process data to identify significant associations between ring formation and operating conditions. Determine improved operating policies that can extend the time between unplanned shutdowns.

Historical process data from a lime kiln with known fouling problems is the primary resource available to achieve these objectives. Hourly averaged samples over five years of operation are taken from the process historian. The data includes over sixty relevant process variables (PVs) (e.g., firing rates, feed rates, moisture content, etc.) of which thirty are from three different thermal cameras. Raw thermal camera images, such as the one shown in Figure 4, are available at four-hour intervals. The KST profile is constructed from twenty-four measurement areas, such as those shown in Figure 4. Each of the three thermal cameras provides ten measurements; eight measurement areas for the KST profile and two measurements related to exterior bracing. Communications with engineers and a mill personnel is another important resource.

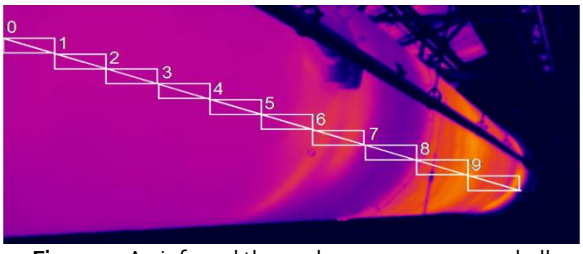

Figure 4. An infrared thermal camera measures shell temperatures along the length of a rotary lime kiln [7].

METHODOLOGY

In this section we describe the proposed methodology for using the available resources to accomplish our ring detection and diagnosis objectives. First, specific strategies for detection and diagnosis are presented. This is followed by a description of our novel approach to process visualization which is instrumental to our ongoing investigations.

Detecting and Diagnosing Ring Growth

In literature fault detection is often reduced to binary classification, i.e., whether or not a fault has occurred. Likewise, diagnosis is often reduced to multi-class classification, i.e., which fault occurred. These experiments are dependent on idealistic labelled datasets where there is no ambiguity regarding the ground-truth of the class labels [15]. In practice, when dealing with outstanding industrial faults and real historical process data, the situation is often far less ideal. In our case, there is no labelled dataset that says where and when faults occurred and what the exact cause was. Instead, as we discuss in what follows, most of the work involves developing techniques to reliably label the historical data.

Residual monitoring and ring detection

The primary objective of ring detection is to provide early indications of ring formation so corrective actions can be taken by operators. A secondary objective of ring detection is to label five years of historical data such that supervised learning methods can be used for identifying high-risk operating conditions and diagnosing ring formation. To accomplish both objectives we develop a validated ring detection algorithm that can automatically identify rings (and therefore provide labels) with new process data.

The proposed ring detection algorithm is based on monitoring residuals (e) between estimated temperatures ($\hat{T}$) and observed temperatures (T). Consider a sample time t as an element of a sequence of sample times $\boldsymbol{t} = (t_1, \cdots, t, \cdots, t_\tau)$ and a specific position x along the KST profile $\boldsymbol{x} = (x_1, \cdots, x, \cdots, x_N)$ measured in terms of distance from the firing end of the kiln. The residual is computed as follows:

$$e(x,t) = \hat{T}(x,t) - T(x,t), \tag{2}$$

where high positive values of the residual indicate a lower-than-expected measured temperature (i.e., potential ring growth), and high negative values indicate a higher-than-expected measured temperature (i.e., potential ring decay). Attributing these residuals to ring formation assumes the mismatch between estimated and actual temperatures is entirely due to rings causing changes in the thermal resistance of the kiln shell wall. The presence of confounding variables (e.g., refractory wear) and disturbances (e.g., measurement noise) make this a precarious assumption. Therefore, to help control for these factors, special consideration must be given to preparing the data and generating temperature estimates.

Two distinct approaches to developing the residual are considered: i) a simple algebraic approach based on a reference start-up profile and *a priori* process knowledge, and ii) an approach based on statistical forecasting. For this work we elaborate on the second approach. Consider a model where the endogenous response variable, $T(t)$, is a vector of the entire KST profile at time t, i.e., $\boldsymbol{T}(t) = (T(x_1,t), T(x_2,t), \cdots, T(x_N,t))^T$. Furthermore, consider a model with variable auto-regressive (AR) order (p), a moving-average (MA) component of variable order (q), and exogeneous regressors (e.g., natural gas feed, mud feed, etc.). This is known as a VARMAX(p,q) model and it models the KST profile at time t as

$$\boldsymbol{T}(t) = \boldsymbol{\varphi_0} + \sum_{i=1}^{p} \boldsymbol{\Phi}_i \boldsymbol{T}(t-i) + \sum_{i=1}^{q} \boldsymbol{\theta}_i \boldsymbol{\varepsilon}(t-i) + \sum_{i=0}^{b-1} \boldsymbol{B}_i \boldsymbol{X}(t-i) + \boldsymbol{\varepsilon}(t), \quad (3)$$

where $\boldsymbol{\varphi_0}$ is a vector of unknown constants, $\boldsymbol{\Phi}_i$ is a matrix of AR coefficients, $\boldsymbol{\theta}_i$ is a matrix of MA coefficients, $\boldsymbol{B}_i$ is a matrix of exogeneous coefficients, and $\boldsymbol{\varepsilon}$ is a vector of error terms. Models of this nature are trained on the historical KST data and temperature forecasts are generated with a rolling origin as demonstrated by Figure 5 below.

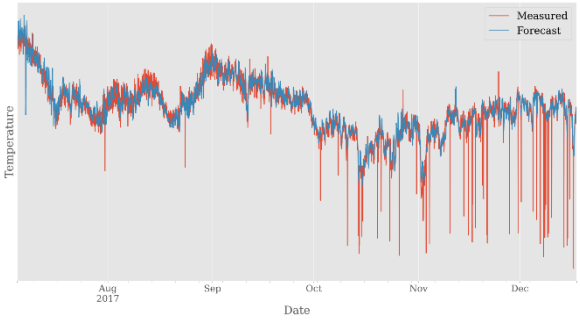

Figure 5. Statistical forecasting of kiln shell temperatures.

Taking the difference of the forecasted and measured temperatures results in a series of residuals. The large drops in measured temperature in Figure 5 demonstrate a problem with the raw camera data, i.e., intermittent obstructions of the camera as shown in Figure 6. Therefore, the series of re siduals requires further processing before it can serve as a ring indicator. A simple thresholding strategy is used to extract residuals that are considered significant.

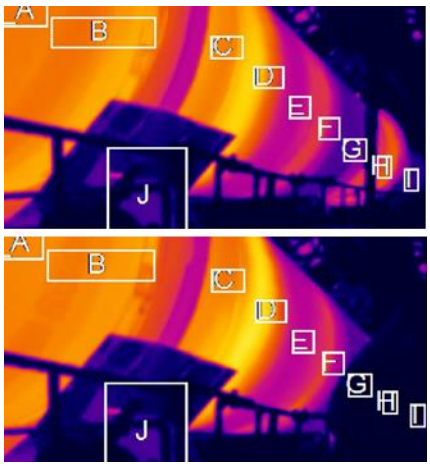

Figure 6. Obstruction of measurement areas G, H and I in the bottom image can corrupt raw data.

Each series of residuals is analyzed as a distribution and the thresholds are based on the first quartile (Q_1), the third quartile (Q_3), and the interquartile range (IQR). Growth residuals, $G(e)$, are extracted as: $Q3 + IQR \leq G(e) \leq Q3 + 3IQR$. Likewise, decay residuals, $D(e)$, are extracted as: $Q1 - 3IQR \leq D(e) \leq Q1 - IQR$. After the significant growth and decay residuals are sampled, daily counts for each growth and decay residual are generated as shown in Figure 7. A final threshold is applied to the daily counts to identify days where ring formation is suspected. Days that are flagged for ring formation are validated with raw data.

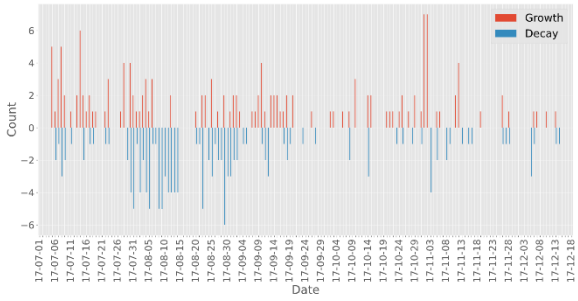

Figure 7. Daily counts for growth and decay residuals.

Supervised learning and ring diagnosis

Once a ring formation indicator has been developed and validated it can be integrated into the historical dataset as a proxy for changes to the state of the ring. Statistical measures, such as cross-correlation with relevant lags, can be quantified to discover significant associations between the ring indicator and relevant PVs. Granger causality tests can be used to determine whether PVs contain information that can help predict ring formation. For non-linear relationships non-parametric statistics such as transfer entropy can be used to quantify transfer of information. Moreover, supervised learning regression models can take PVs as inputs to predict the residuals. If predictions are sufficiently accurate and reliable the models can be interrogated to determine the influence of PVs on ring formation.

As mentioned before, an important prerequisite for using supervised learning to infer causes of ring formation is an accurately labelled dataset. The primary quantitative results in this work involve validating and improving the reliability of ring detection. To supplement for the lack of a high-quality labelled dataset, qualitative insights on diagnosis from research and exploratory data analysis are provided. The exploratory data analysis is enhanced by a novel approach to process visualization as the following subsection describes.

Kiln Monitoring with Interactive Visualization

To detect rings the KST profile needs to be visualized over varying periods of time. A common approach in industry is to overlay KST profiles taken from different periods of interest as demonstrated by the three KST profiles in Figure 8. While this approach to visualizing shell temperatures does

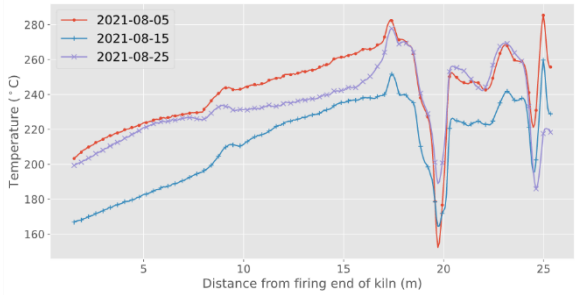

Figure 8. Observing changes in shell temperature profiles by overlaying profiles from ten-day intervals.

provide some insights into KST profile changes over time it is significantly limited. If too few profiles are overlayed, it is uninformative; if too many profiles are overlayed, it is incomprehensible.

To intuitively visualize large quantities of KST profiles in a user-friendly manner we propose the novel visualization strategy presented in Figure 9. This spatiotemporal heatmap shows axial shell temperature variations along the y-axis and continuous temporal shell temperature variations along the x-axis. The y-axis temperatures from Figure 8 are embedded as the uniform, sequential colormap on the right side of Figure 9. Embedding the temperatures as colors enables a clear, intuitive visualization of large quantities of KST data. Previous work demonstrates how the spatiotemporal heatmap is complemented by interactive features to enable visualization of rings over varying timescales and in the context of relevant PVs [7]. This visualization tool has been critical for validating ring detection and exploring the historical data with subject matter experts to extract insights into diagnosis.

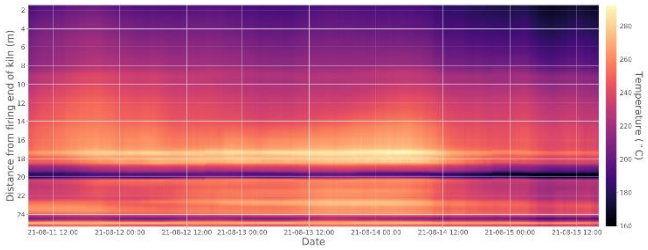

Figure 9. Spatiotemporal heatmap of KST profiles.

RESULTS

The results presented here primarily highlight the efforts made to validate the ring formation indicator. Preliminary insights from manual investigations into ring diagnosis are also presented.

Validating the Ring Formation Indicator

The analysis begins with five years of raw thermal camera data, as shown in the top part of Figure 10. This data contains unwanted data from shutdowns (i.e., black vertical streaks) and sensor failures (i.e., periods with zero variability). The middle plot in Figure 10 shows the result of removing this unwanted data. Extracting periods where the entire KST profile is valid for at least 30 days results in the twelve distinct periods of operation, referred to as experimental trials, shown in the bottom plot of Figure 10.

Although there are 24 measurement positions along the KST profile, for now let us consider just a single position, i.e., 18 m from the firing end of the kiln. A univariate formulation of equation 3 is used to forecast shell temperatures at the 18 m position. The IQR filtering is conducted to sample significant residuals from which daily counts are generated. Figure 5 and Figure 7 demonstrate the forecast and the daily counts at 18 m for the longest experimental trial (i.e., the fifth). This procedure is repeated for each of the twelve experimental trials and a threshold is applied to all 751 days. Days with growth/decay counts greater than 4 are flagged for ring growth/decay, respectively. Ultimately, 24 days are flagged for ring growth and 51 days are flagged for ring decay. Manual validation is conducted for both growth and decay using the raw thermal camera images and other available resources.

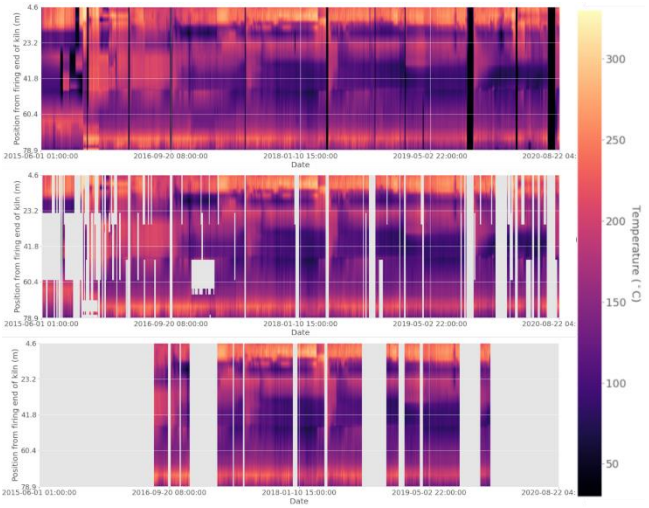

Figure 10. Top: raw KST data from five years of operation. **Middle:** removing invalid data from shutdowns and sensor failures. **Bottom:** Exracting extended periods of clean data for analysis.

Consider the period around 17-11-03 from Figure 7 which shows two high growth days followed by one decay day. To validate these growth and decay events we observe the raw thermal camera images (focusing on measurement area G) and compare the forecast to the measured temperature as shown in Figure 11. The growth indication on 17-11-01 is considered a true positive (TP) given the clear growth from the day prior. For similar reasons the decay indication on 17-11-03 is also considered a TP. However, the growth indication on 17-11-02 is not as certain. The temperature trends indicate potential growth in the first half of the day, but this is not clear from the thermal camera images which are only available every four hours.

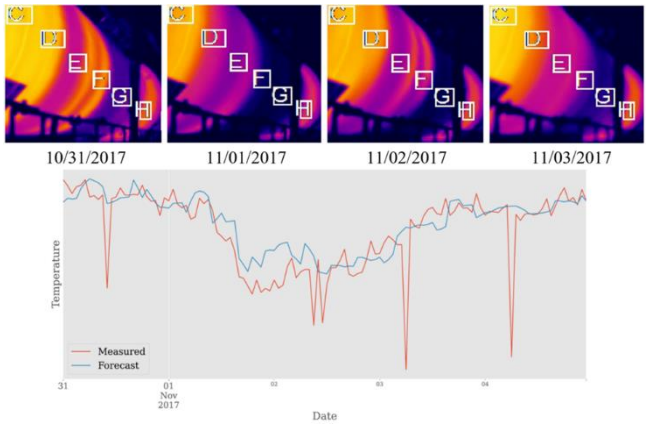

Figure 11. Validating ring formation indications with raw thermal camera images (top) and forecast results (bottom).

A similar manual validation procedure is performed for each of the 75 flagged days. In binary classification terms we are performing two separate binary classifications, i.e., one for ring growth and one for ring decay. The flagged days represent positive events, and the validation of these days is performed to determine the precision of each indicator, i.e., the ratio of TP to all positive events. Table 1 shows the results of the preliminary validation of the ring indicator. To address events with insufficient evidence a second binary label is applied to

each event, i.e., whether the validation assignment is certain. As Table 1 shows, the precision for the growth indicator is 68.2% but only 31.8% of validation labels are considered certain. The results for ring decay are slightly better with a precision of 87.5% and a certainty of 42.5%.

Table 1: Validating growth and decay indications for precision.

Indication	Precision	Certainty
Growth	68.2%	31.8%
Decay	87.5%	42.5%

The major sources of uncertainty are insufficient raw data (e.g., thermal images are too infrequent) and rotational aliasing. Rotational aliasing was discovered as a direct result of the manual validation procedure, and it results in the high frequency KST variations demonstrated in Figure 12. It occurs because the KST measurements are taken as snapshots every minute while the kiln rotates at a speed of approximately 1 rpm, i.e., the KST data does not meet the Nyquist rate [16]. Aliasing causes averaged KST measurements that are not representative of the entire circumference of the kiln. When there is non-uniform build-up of ring material along the circumference the aliasing can cause biased measurements which can result in the high frequency temperature variations demonstrated in Figure 12. This can in turn lead to false positives and high uncertainty of ring indications.

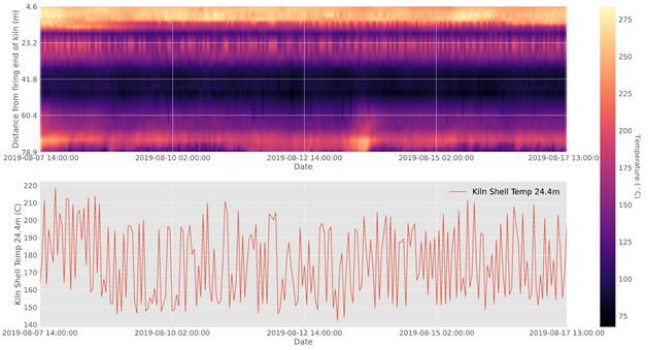

Figure 12. High frequency KST variations changing over 50°C per hour are suspected to be a result of rotational aliasing.

Given this untenable degree of uncertainty, improvements are required to proceed with ring indicator development. One such improvement is enhanced KST measurements to address aliasing. Instead of using 24 measurement areas to collect KST data, a continuous profile line like that shown in Figure 4 is used to collect temperature readings at every pixel. Moreover, instead of taking snapshots every minute, snapshots are now taken every five seconds. These higher frequency snapshots are then averaged into a KST measurement that is more representative of the entire kiln circumference. The plot on the left side of Figure 13 shows the correlation coefficient for each of the profile line positions surrounding the 18 m measurement area. A maximum correlation coefficient of 0.972 is obtained at x-coordinate 325. The plot on the right side of Figure 13 shows the comparison of the measurement area data (red) with the profile line data (blue) which demonstrates the successfully reduced high frequency variability, especially after 2021-08-21.

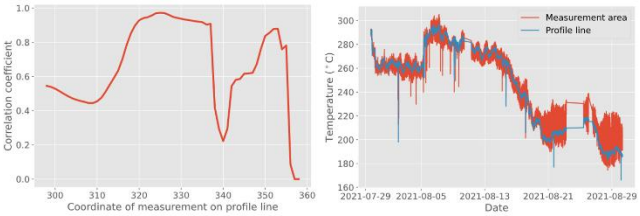

Figure 13. Left: the correlation coefficient between KST data from a measurement area and KST data from various profile line positions denoted by their x-coordinate. **Right:** profile line data with the highest correlation (blue) is plotted with measurement area data (red) to demonstrate improved noise reduction.

Preliminary Insights on Diagnosis

Without a validated ring formation indicator, we are unable to provide rigorous quantitative results on ring diagnosis. However, during this work a great deal of exploratory analysis was conducted whereby we manually diagnose individual ring events. Figure 14 shows an example where the interactive process visualization tool is used to discover mud solids content as a potential cause of ring formation. Given the fact that rings can form gradually over a matter of months, diagnosing a root cause can be very difficult. In addition to mud solids content, other variables of interest are alkali content in the mud (e.g., white liquor clarifier performance), operational instability (e.g., sheet drops), and unmeasured variables such as the amount of dust in the kiln.

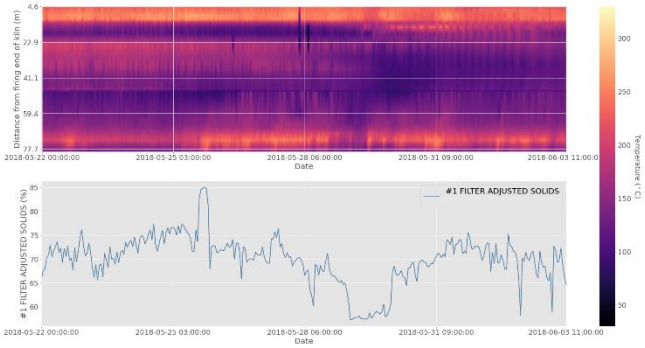

Figure 14. Sustained drop in mud solids content after 2018-05-28 is suspected to cause a mid-kiln ring that persists for weeks.

CONCLUSIONS AND FUTURE WORK

This paper presents our work on detecting and diagnosing ring growth in a rotary lime kiln. A novel approach to visualizing the KST data was developed to enhance our investigation. Although the precision of the proposed ring indicator is fair, the resources available for manual validation are insufficient to be certain. Rotational aliasing was discovered and addressed with an improved KST measurement strategy. Future work will involve another round of manual validation with high frequency data and improved measurements. Finally, future work will leverage the validated indicator to generate quantitative insights into ring diagnosis.

ACKNOWLEDGEMENTS

The authors thank Spartan Controls, the National Science and Engineering Research Council of Canada, and the Izaak Walton Killam Memorial Fund for funding this research.

REFERENCES

1. Russell EL, Chiang LH, Braatz RD Fault detection in industrial processes using canonical variate analysis and dynamic principal component analysis. *Chemometrics and intelligent laboratory systems* 51:81-93 (2000)
2. Spyridon P, Boutalis YS. Generative adversarial networks for unsupervised fault detection. *In 2018 European Control Conference (ECC)* (pp. 691-696). IEEE (2018)
3. Gorog JP, Leary W. Ring removal in rotary kilns used by the pulp and paper industry. *TAPPI J* 15:205-213 (2016)
4. Barham D, Tran HN. An overview of ring formation in lime kilns. *TAPPI Proceedings, 1990 Pulping Conference*, (1990)
5. Tran H, Mao X, Barham D. Mechanisms of ring formation in lime kilns. *J Pulp Paper Sci* 19:J167 (1993)
6. Ribeiro B, Costa E, Dourado A. Lime kiln fault detection and diagnosis by neural networks. *Artificial Neural Nets and Genetic Algorithms* (pp. 112-115). Springer, Vienna (1995).
7. Rippon L, Hirtz B, Sheehan C, Reinheimer T, Loewen P, Gopaluni B. Visualization of multiscale ring formation in a rotary kiln. *Nordic Pulp & Paper Research J.* AOP (2021).
8. Bogdanski BE. The rise and fall of the Canadian pulp and paper sector. *The Forestry Chronicle*, 90:785-793 (2014)
9. Smook GA, Kocurek MJ. Handbook for pulp & paper technologists. *Canadian Pulp and Paper Association* (1982).
10. Dernegård H, Brelid H, Theliander H. Characterization of a dusting lime kiln–A mill study. *Nordic Pulp & Paper Research Journal* 32:25-34 (2017)
11. Natural Resources Canada Office of Energy Efficiency. Benchmarking energy use in Canadian pulp and paper mills. *Ottawa – Ontario: Natural Resources Canada* (2008)
12. Hirtz B, Marshman D, Sheehan C. Kiln Infra-Red Cameras for Abnormal Situation Detection and Residual Carbonate Control. *JFOR: J Sci Technol For Prod Process*, 6:28-36 (2017)
13. Tran H. Lime kiln chemistry and effects on kiln operations. *Pulp & Paper Centre and Department of Chemical Engineering and Applied Chemistry, University of Toronto*, Toronto, Canada (2007)
14. Lindblom J, Theliander H. The Influence of Carbon Dioxide on Ring and Ball Formation in a Pilot-Scale Rotary Kiln. *KONA Powder Particle J*, 19:109-117 (2001)
15. Lv F, Wen C, Bao Z, Liu M. Fault diagnosis based on deep learning. *In 2016 American control conference (ACC)* (pp. 6851-6856). IEEE (2016)
16. Shannon CE Communication in the presence of noise. *Proceedings of the IRE*, 37:10-21 (1949)

This conference proceeding has not been peer reviewed.

CSChE Systems & Control Transactions

Open Access | Original Research

Conference Proceedings
Canadian Chemical Engineering Conference 2021
October 24-27, Montréal, Québec, Canada

PSEcommunity.org/LAPSE:2021.0793

PSE PRESS

Constant Power Generation by Scheduling Installation of SOFC Modules Operating in Varying Power Mode

Mina Naeini[a], Thomas A. Adams II[a]*, and James S. Cotton[b]

[a] McMaster University, Department of Chemical Engineering, Hamilton, Ontario, Canada
[b] McMaster University, Department of Mechanical Engineering, Hamilton, Ontario, Canada
* Corresponding Author: tadams@mcmaster.ca.

ABSTRACT

In this paper, producing constant power load of 550 MW from systems of Solid Oxide Fuel Cells (SOFCs) operating in varying power output mode was investigated. This is useful because previous research has shown that individual cells can have significant lifetime extensions when operated according to certain dynamic trajectories in which power production decreases over time. In this study, we determined that a constant net power output of a system comprised of many individual SOFC modules can be achieved by scheduling the installation and operation of each SOFC module in a particular manner. All the modules were operated under the optimal operating conditions obtained in our previous optimization study where power output of each module declined over time. The dynamic degradation of SOFCs was taken into account by using a detailed mathematical model of long-term performance degradation as a function of operating conditions. The result is a system in which every 5 days, one new SOFC module is brought online, replacing one module near the end of its useable life at the same time. With this staggered approach, the overall power output of the system can be maintained at an almost constant level at all times (550 MW for our example). The new module then gradually reduces its power output over time according to an optimal trajectory. With this approach, the overall system can produce an essentially constant supply of power at lower costs than a traditional approach where all SOFC modules within a large system are each operated at constant power.

Keywords: SOFCs, performance degradation, optimal operating conditions, optimal operating mode, constant power output.

Date Record: Original manuscript received October 15, 2021. Published October 21, 2021

INTRODUCTION

Solid Oxide Fuel Cells (SOFCs) are known for their high electrical efficiency and low environmental burdens, but they are yet to be commercialized in large-scale [1]. The degradation of these fuel cells is one main barrier for adoption [1]. SOFCs degrade due to a confluence of multiple phenomena which occur under normal operating conditions [2]. Several research studies focused on overcoming this issue by developing novel materials for different components of SOFC or by changing the structure [3–5]. But none of these new technologies had the required technical or economical feasibility for widespread commercialization. The focus of our research however is to overcome this barrier by understanding the degradation mechanisms through mathematical models and using them to determine operating strategies which reduce the rate of degradation.

In our prior study, we constructed a dynamic mathematical model of degradation by integrating six different models which each represent a different degradation reaction into thermodynamic models of overpotentials [6]. The developed model is capable of accurate prediction of long-term performance decline in SOFCs as a function of operating conditions, most importantly current density. This model allows investigators to extend the lifetime of SOFCs and operate them more economically by avoiding detrimental conditions that accelerate SOFC breakage. This can be easily achieved by adjusting the operating conditions and running SOFCs with an appropriate operating trajectory that involves slow and gradual changes over the course of its lifetime.

The findings of a techno-economic analysis (TEA) performed in our previous study using this model showed that conventional SOFCs can operate as long as 14 years economically if run at optimal operating conditions and with optimal dynamic trajectories [7]. The results also indicated that the optimal strategy for long-term operation of SOFCs is to gradually decrease the current density drawn from the fuel cells and let the power output drop over time. According to those findings, operating an SOFC in constant power mode (i.e. baseload power generation mode) is undesirable, because to achieve constant power one must continually increase the current density to compensate for degradation over time. This

increasing current density in turn further accelerates the degradation of the fuel cells and thus should be avoided. Thus, even though constant power mode is often used in practice, the prior work shows that it is significantly more expensive than operating in a mode in which power gradually drops over time.

However, constant power output is nonetheless required for some applications and so gradually decaying power production is not useful or desirable. However, we can overcome this challenge by recognizing that some SOFC systems consist of many individual cells bundled into stacks, which are in turn bundled into modules, and the system itself can contain many modules. Thus, depending on the size of the system, modules, stacks, or even individual cells can be independently operated in varying power mode under optimal conditions, but the modules, stacks, or cells are installed gradually at different points of time such that the overall SOFC system delivers a constant amount of power.

DEMOSTRATION OF THIS WORK

For this study, we used the optimal sizes and operating trajectories obtained for SOFCs in varying power mode in our previous TEA study [7]. In other words, we assume that once an SOFC is started, its current density and power should follow a particular declining trajectory that has been predetermined by economic optimization as presented in the previous work (see Figure 1). One key parameter is the desired replacement schedule of the cell modules. The designer can choose the scheduled replacement time of a cell module (between 1 and 10 years in our study), and as long as the cell does not experience unexpected catastrophic failure, there will be some optimal way of operating that cell module within the desired lifetime.

As noted in the previous work, targeting shorter replacement times means it is optimal to use the cell more aggressively, drawing more power out of it but causing significant degradation such that the cell erodes quickly. Longer target replacement times (up to 14 years) are possible but it is optimal to operate much less aggressively and in a fashion which avoids decay. The previous work shows that longer lifetimes are more economical but the target replacement time in practice will depend on factors such as the risk of catastrophic failure, which the model cannot predict and may be unique to each specific manufacturer. Therefore, the target replacement time is taken as a parameter in this work, with two extremes considered for brevity (1 year and 10 year).

In the prior work, the SOFC systems were constrained to produce an average of 550 MW electrical power output during their lifetime, and the optimal size of SOFC active membrane area (A_m) for production of this power was found. The optimal cumulative power profile which minimizes levelized cost of electricity (LCOE) for a given target cell lifetime and has this average of 550 MW power produced is shown in Figure 1b. It is assumed that the fuel cells are identical, and each SOFC module contains multiple stacks of identical fuel cells. At the end of lifetime of the SOFCs (which all occur simultaneously), they are all replaced with identical fuel cells of the same size. This procedure is repeated during the 20 years life of the plant.

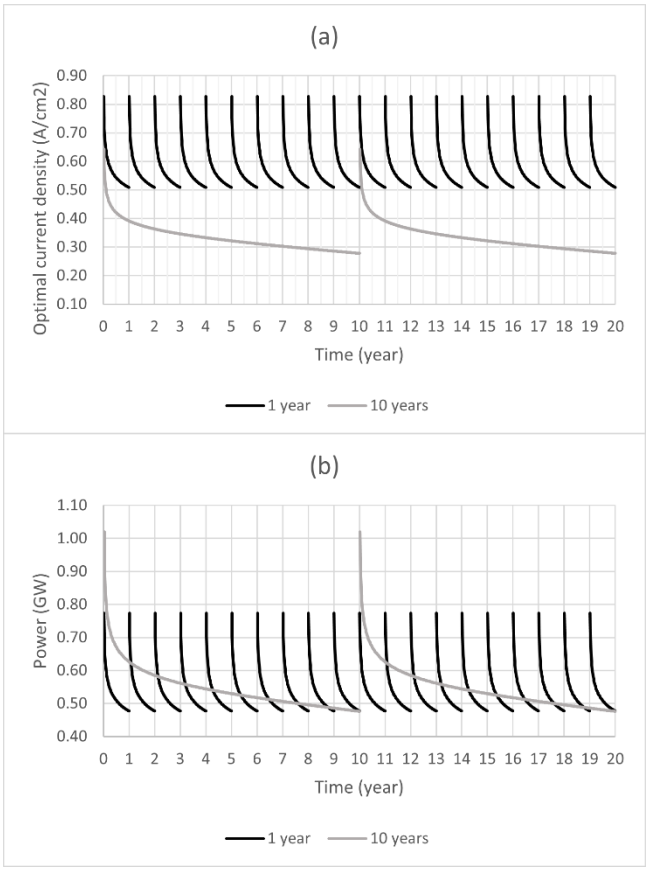

Figure 1. a) Optimal current density and b) power output of SOFCs with 1- and 10-year lifetimes during 20 years life of the plant [7].

In this study, instead of installing all the fuel cells at once, we install one module every 5-days. A module consists of a group of 1 or more stacks. It should be noted that all the modules have the same size and all individual SOFCs follow the same optimal trajectories found in our prior work (Figure 1) [7]. With this approach every 5 days a new module is brought online and at the same time a module that has reached end of its life is replaced. In this scheduled system, even though the SOFC modules in operation degrade and provide less power over time, the brand-new modules, brought online later, provide higher power, and compensate for the performance decline of the older modules. As a result, the system reaches steady state after a while and can provide constant power regardless of the performance drop of individual modules.

Figure 2 shows the net power output of staggered systems with individual SOFCs in varying power mode with 1- and 10-year lifetimes.

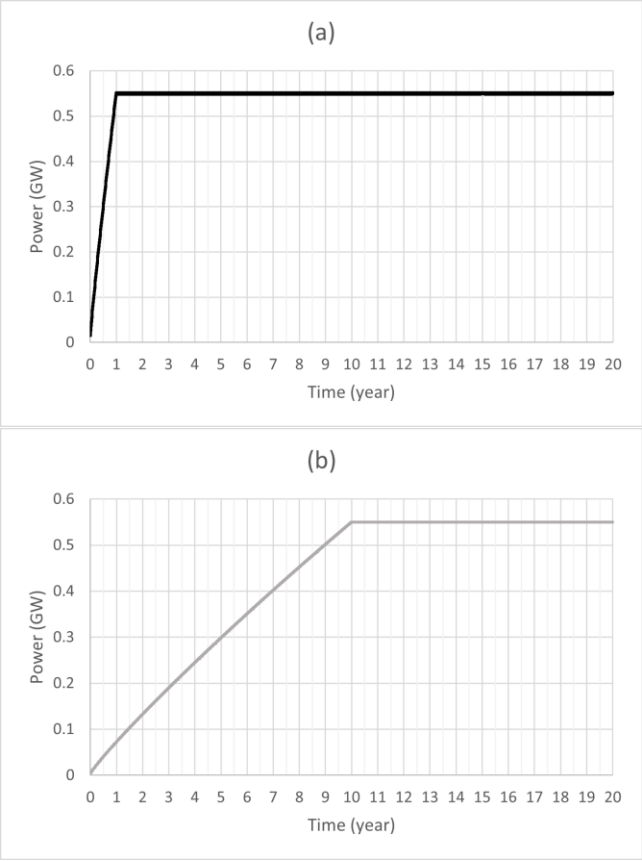

Figure 2. Net power output of systems in which modules are installed every 5 days and individual SOFCs are allowed to have variable power with a) 1- and b) 10-year lifetimes.

With this methodology, the system does not reach steady state instantaneously. Depending on the size of the modules and the optimal trajectories, different systems reach constant net power output at different times. For instance, with the given scheduling plan and optimal trajectories, the system of SOFCs with a 1-year replacement plan reaches almost constant power of 550 MW after 1 year of operation, while the system of SOFCs with a 10-year replacement plan provides nearly constant power of 550 MW after 10 years of operation.

This is a critical finding as it indicates that to get a constant net power from SOFC systems, individual SOFCs in the system should not necessarily be operated in baseload power generation mode. Instead, they can have variable power and constant net system power can be achieved by installing SOFC modules on a scheduled basis. The importance of the current methodology is in enabling constant net power generation with lower costs comparing to traditional baseload power generation mode. The characteristics and economics of systems in current methodology and traditional baseload power generation mode are shown in Table 1.

Table 1: Characteristics and economics of SOFC systems with constant power output. Project lifetime is 20 years.

	Individual SOFCs operated in varying power mode. (Modules are staggered every 5 days.)		**Individual SOFCs operated in baseload power mode. (All stacks are installed at once.)**	
Replacement Schedule:	**1 yr**	**10 yr**	**1 yr**	**10 yr**
Area of individual SOFC (cm^2)	414	414	414	414
Average lifetime power produced by one SOFC (W)	123	85	106	79
SOFCs per stack	259	259	259	259
Average lifetime power produced by one stack (kW)	32	22	27	20
Total size needed (m^2)	184,555	267,690	215,637	289,657
Total stacks needed	17,212	24,965	220,111	120,275
Stacks per module	236	34	N/A	N/A
Total lifetime average power (MW)	537.9	424.3	550	550
Steady state power (MW)	550	550	550	550
System power at beginning of replacement cycle (MW)	789	1014	550	550
System power at end of replacement cycle (MW)	477	476	550	550
Time to reach steady state	1 yr	10 yr	immediate	immediate
LCOE ($/kWh)	0.357	0.131	0.409	0.143

FUTURE STUDY

The major drawback of the current approach is that the net system power does not reach a constant load instantaneously. Future work can focus on generation of constant power throughout the entire life of the plant from an SOFC system in which individual SOFCs are allowed to have variable power. This can be achieved using either of the following methods: a) solving a separate problem to find optimal size, installation scheduling, and operation of stacks that should be used before systems shown in Figure 2 reach steady state, such that combination of the system and these additional stacks generate nearly constant load of 550 MW throughout 20 years life of the plant, b) solving a general optimization over 20 years of every individual stack/module to find optimal schedule and operation for each stack/module such that the system produces 550 MW at all times during plant's life. The latter problem may be intractable.

CONCLUSION

This research showed that by using stacking capability of SOFCs a net constant power load can be generated from a system of SOFC modules in which individual fuel cells follow an optimal declining trajectory. By bringing a new module online and replacing a module near end of its life every 5 days, the system can reach steady state and produce a constant power output. This is significant because it enables a steady power output while avoiding using fuel cells in traditional baseload power mode in which fuel cells degrade at high rates. As a result, this approach was shown to be more economical than constant load production by running all fuel cells in baseload power mode.

ACKNOWLEDGEMENTS

We greatly acknowledge the financial support from Natural Sciences and Engineering Research Council of Canada [NSERC CRDPJ 509219-2017] and the Ontario Centre of Excellence [OCE 27851-2018].

REFERENCES

1. V Zaccaria V, Traverso A, Tucker D. A real-time degradation model for hardware in the loop, in: *Proc. ASME Turbo Expo 2015 Turbine Tech. Conf. Expo*. GT:1-8, (2015)
2. T Parhizkar T, Hafeznezami S. Degradation based operational optimization model to improve the productivity of energy systems, case study: Solid oxide fuel cell stacks. *Energy Convers Manag* 158:81-91 (2018)
3. Niemczyk A, Świerczek K. Development of novel air electrode materials for the SOFC and SOEC technologies. *E3S Web Conf.* 108 (2019)
4. Patro PK, Delahaye T, Bouyer E. Development of Pr0.58Sr0.4Fe0.8Co0.2O3 – δ–GDC composite cathode for solid oxide fuel cell (SOFC) application. *Solid State Ion* 181:1378-1386 (2010)
5. Tietz F, Mai A, Stöver D. From powder properties to fuel cell performance – A holistic approach for SOFC cathode development. *Solid State Ion* 179:1509-1515 (2008)
6. Naeini M, Lai H, Cotton JS, Adams TA II. A mathematical model for prediction of long-term degradation effects in solid oxide fuel cells. *Ind Eng Chem Res* 60:1326-1340 (2021)
7. Naeini M, Cotton JS, Adams TA II. Economically optimal sizing and operation strategy for solid oxide fuel cells to effectively manage long term degradation. Submitted for publication (2021)

CSChE Systems & Control Transactions

Open Access | Original Research

Conference Proceedings
Canadian Chemical Engineering Conference 2021
October 24-27, Montréal, Québec, Canada

PSEcommunity.org/LAPSE:2021.0794

PSE PRESS

Bypass Control of HEN Under Uncertainty in Inlet Temperature of Hot Stream

Chaitanya Manchikatla, Zukui Li*, and Biao Huang

University of Alberta, Department of Chemical and Materials Engineering, Edmonton, Alberta, Canada
* Corresponding Author: opti

ABSTRACT

The dynamic control of Heat Exchanger Network is significant for developing energy efficient and safe industrial processes. In this project, the hot stream's inlet temperature is considered uncertain because it is common in industries. The cold stream is bypassed around the heat exchanger. This project aims to track the setpoint temperature of the mixed stream by manipulating the bypass fraction of the cold stream around the Heat Exchanger given uncertainty in the inlet temperature of the hot stream. The control is implemented in Nonlinear Model Predictive Control (NMPC) framework. The uncertainty in the optimal control problem (OCP)is dealt by using scenario tree based approximation as well as affine policy based method. The model of the system considered is based on the first principles model, i.e. dynamic model of shell and tube heat exchanger. The Orthogonal collocation technique is used to discretize the first principles model into the system of algebraic equations. The results show that for the possible scenarios of uncertainty, the control variable efficiently tracks setpoint using input from uncertain optimization. The performance of the proposed control method is also demonstrated using step-change in setpoint. In comparison, considering the same scenarios of uncertainty used, the graph of the control variable simulated using input obtained from deterministic optimization shows the control variable deviates from the setpoint as time passes.

Keywords: Uncertain Optimization, Model Predictive Control, Heat Exchanger Network, Affine Control Policy

Date Record: Original Manuscript received October 18, 2021. Published October 21, 2021.

INTRODUCTION

In industries, nearly 80% of the total energy consumption is related to heat transfer [1]. For efficient heat transfer and energy intensified processes, it is obvious that the design and dynamic control of the Heat Exchanger Network (HEN) play an important role [3]. This saves million dollars to the chemical industries. Generally, the outlet temperatures are controlled by manipulating flow rates. But, when the flow rates are set by process requirements in HEN, bypass control is adopted widely [6]. Bypass control provides very tight temperature control since the dynamics of blending a hot stream (stream through the heat exchanger) and a cold stream (bypassed stream) is very fast.

In literature, the bypass control of HEN was formulated using deterministic approaches like LQR [7]. For HENs, the optimal bypass location was selected by calculating the non-square Relative Gain Array [1]. But, the control problem of the Heat Exchanger Network is considerably challenging because of the highly nonlinear dynamics, disturbances in inlet temperatures of streams [5].

This project aims to track the setpoint temperature of the mixed stream by manipulating the bypass fraction of the cold stream around the Heat Exchanger given uncertainty in the inlet temperature of the hot stream. The control is implemented in Nonlinear Model Predictive Control (NMPC) framework. At each sampling instant the uncertain Optimal Control Problem (OCP) is solved for the entire Prediction horizon (tp). The Prediction horizon is divided into N control horizon intervals of uniform length, and the bypass fraction is assumed to be constant in an interval [2]. For bound constraints on input (bypass fraction), the uncertainty is handled by deriving robust counterparts using the Affine Control Policy approach i.e. the input is assumed to be an affine function of uncertainty. The uncertainty in algebraic equations of the model is handled by assuming scenarios of possible uncertainty [4]. The Receding horizon implementation of MPC is implemented using MATLAB and the optimization is done using GAMS.

PROBLEM STATEMENT

The system considered in this research work is Heat Exchanger Network. Generally, for efficient heat integration process streams are used for heat exchange along with utilities in industries. The desired out temperatures of the streams are controlled by using bypasses, and manipulated these bypass fractions around the heat exchanger. The simple Heat

Exchanger Network with single heat exchanger, a hot stream, and bypassed cold stream is given by **Figure 1**. The **Figure 1** also shows the objective of the current research work.

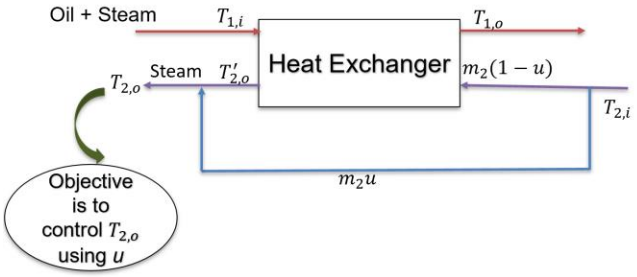

Figure 1. Simple HEN showing bypassed cold stream and objective.

It's common that the inlet temperatures of process streams are corrupted by the disturbances. So, to ensure safe processes and we achieve target out temperatures of the streams the control problem of HEN is formulating considering these disturbances. In this work, we aim to track the setpoint temperature of the mixed stream by manipulating the bypass fraction of the cold stream around the Heat Exchanger given uncertainty in the inlet temperature of the hot stream.

DYNAMIC MODEL OF HEN

The shell and tube dynamic model of the Heat Exchanger i.e., the system considered in this research work is given in this section. Hot stream flows through shell side, and cold through tube side. Counter current flow is assumed. m_1 is the flow rate of hot fluid. If F_2 is the total flow rate of cold fluid, its flow rate through Heat exchanger is given by,

$$m_2 = F_2(1-u) \tag{1}$$

Here u is the bypass fraction. M_1 and M_2 are the flow rates per unit area of hot fluid and cold fluid respectively in Heat exchanger. The model is given by following system of PDEs, and these PDEs denote energy conservation in unit element.

Shell side:

$$\frac{\partial T_1(x,t)}{\partial t} = \frac{m_1}{M_1}\frac{\partial T_1(x,t)}{\partial x} + \frac{\pi d_o K_o}{M_1 C_{P_1}}[T^{wo}(x,t) - T_1(x,t)] \tag{2}$$

Tube outer wall:

$$\frac{\partial T^{wo}(x,t)}{\partial t} = \frac{2\lambda\pi}{M_w C_{P_w} ln(r_2/r_1)}\left[T^{wi}(x,t) - T^{wo}(x,t)\right] + \frac{\pi d_o K_o}{M_w C_{P_w}}[T_1(x,t) - T^{wo}(x,t)] \tag{3}$$

Tube inner wall:

$$\frac{\partial T^{wi}(x,t)}{\partial t} = \frac{2\lambda\pi}{M_w C_{P_w} ln(r_2/r_1)}\left[T^{wo}(x,t) - T^{wi}(x,t)\right] + \frac{\pi d_i K_i}{M_w C_{P_w}}\left[T_2(x,t) - T^{wi}(x,t)\right] \tag{4}$$

Tube side:

$$\frac{\partial T_2(x,t)}{\partial t} = \frac{m_2}{M_2}\frac{\partial T_2(x,t)}{\partial x}1 + \frac{\pi d_i K_i}{M_2 C_{P_2}}[T^{wi}(x,t) - T_2(x,t)] \tag{5}$$

heat transfer coefficient at outer wall:

$$1/K_O = \frac{1}{K_1 m_1} + R_o \tag{6}$$

heat transfer coefficient at inner wall:

$$1/K_i = \frac{1}{K_2 m_2} + R_i \tag{7}$$

In the current work, the above system of PDE is first discretized into system of ODE, and then the system of ODE is discretized into system of nonlinear equations using Orthogonal collocation technique. The Orthogonal collocation technique is given section 0

METHODOLOGY

The methods used to address bypass control of HEN under uncertainty are described in this section. The problem is solved under nonlinear model predictive control framework using multistage uncertain optimization techniques. The Optimal Control Problem is given by ,

$$\min_{\Delta \boldsymbol{u}} \int_{t=0}^{t\_P}\left(T_{2,o}(t,\zeta) - T_{st}(t)\right)^2 + \sum_{n=1}^{N}\alpha(\Delta u\,(n,\zeta))^2 \tag{8}$$

$$s.t.$$

$$\dot{x}(t,\zeta) = f(x(t,\zeta), u(n,\zeta), \theta) \qquad x(0) = x_o \tag{9}$$

The Heat exchanger model is given by $f(x(t), u(t), \theta)$

$$T_{2,o}(t,\zeta) = u(n,\zeta)T_{2,i}(t) - (1-u(n,\zeta))T'_{2,o}(t,\zeta) \tag{10}$$

$$\Delta u_{min} \le \Delta u(n,\zeta) \le \Delta u_{max} \tag{11}$$

$$x_{min} \le x(t,\zeta) \le x_{max} \tag{12}$$

ζ indicates primitive uncertainty in inlet temperature of hot stream. The objective function is given by Equation (8), the first term of objective function indicates setpoint tracking, and second term indicates controller effort term. Here T_{st} is the setpoint of control variable (the mixed stream temperature). Equation (9) represents HEN model, and Equation (10) represents mixed stream temperature constraint. Equation(11) and Equation(12) represent bounds on change in input and states respectively. Here x is vector containing all the states of the model.

The steps involved in converting above intractable (because of the uncertainty considered) optimal control problem to tractable is shown by **Figure 2**.

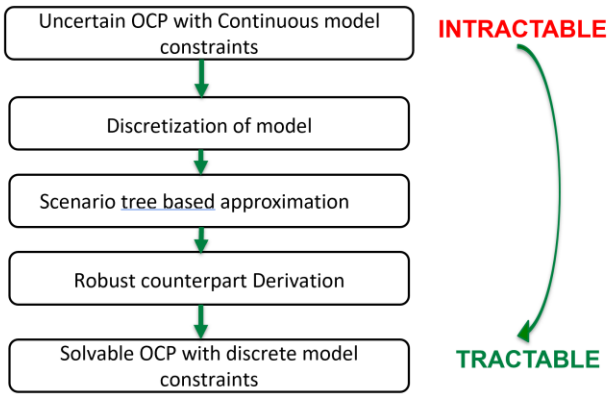

Figure 2. Steps of converting intractable OCP to tractable

Discretization of model

The orthogonal collocation technique is used to discretize the system of ODEs into system of nonlinear equations. The model of the Heat Exchanger Network is represented by this system of nonlinear equations from now on. For demonstration purpose, the Orthogonal collocation technique is applied to single Heat Exchanger model in this section. At each time instant, we assume that the prediction horizon (t_p) is divided into N (control horizon) intervals. The input is assumed to be constant in n^{th} ($n = 1,2,\ldots,N$) interval, and it is denoted by $u(n)$. Each n^{th} interval is divided into $K+1$ intervals using K collocation points. The state vector at $k^{th}(k = 1,2,\ldots,K)$ collocation point, $len^{th}(len = 1,2,,13)$ spatial discretization point, and in n^{th} interval is denoted by $T_{len,n,k}$.

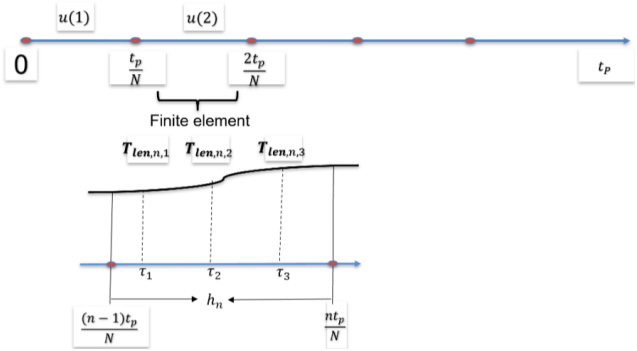

Figure 3. Polynomial approximation of state profile across finite element with 3 collocation points

The states in each finite element are approximated using Lagrange interpolation polynomials. The states are given by,

$$\begin{bmatrix} t = t_{n-1} + h_n\tau \\ T_{len}(t) = \sum_{k=0}^{K} l_k(\tau) T_{len,n,k} \end{bmatrix} \quad \forall t = [t_{n-1}, t_n],\ \tau = [0,1] \qquad (13)$$

$$l_k(\tau) = \prod_{j=0,\ j\neq k}^{K} \frac{(\tau-\tau_j)}{(\tau_k-\tau_j)} \qquad (14)$$

The approximated derivative of states at these collocation points is equated with ODE model, and the HEN model now is given by,

$$\sum_{k=0}^{K} T_{1,\,len,\,n,\,k} \frac{dl_j(\tau_k)}{d\tau} = h_n \left[\frac{m_1}{M_1} \frac{[T_1(len,n,j) - T_1(len-1,n,j)]}{[x_{len} - x_{len-1}]} + \frac{\pi d_o K_o}{M_1 C_{p1}} [T^{wo}{}_{len,\,n,\,j} - T_1(len,n,j)] \right]$$

$$len = 1,2,3,\ldots,13.\ \ n = 1,2,3,\ldots,N.\ \ j = 1,2,3,\ldots,J \qquad (15)$$

$$\sum_{k=0}^{K} T^{wo}{}_{len,\,n,\,k} \frac{dl_j(\tau_k)}{d\tau} = h_n \left[\frac{2\lambda\pi}{M_w Cp_w ln\left(\frac{r2}{r1}\right)} [T^{wi}_{len,n,j} - T^{wo}{}_{len,\,n,\,j}] + \frac{\pi doKo}{M_w Cp_w} [T_{1,len,n,j} - T^{wo}{}_{len,\,n,\,j}] \right]$$

$$len = 1,2,3,\ldots,13.\ \ n = 1,2,3,\ldots,N.\ \ j = 1,2,3,\ldots,J \qquad (16)$$

$$\sum_{k=0}^{K} T^{wi}{}_{len,\,n,\,k} \frac{dl_j(\tau_k)}{d\tau} = h_n \left[\frac{2\lambda\pi}{MwCp_w ln\left(\frac{r2}{r1}\right)} [T^{wo}_{len,n,j} - T^{wi}{}_{len,\,n,\,j}] + \frac{\pi d_i K_i}{M_w Cp_w} [T_{2,len,n,j} - T^{wi}{}_{len,\,n,\,j}] \right]$$

$$len = 1,2,3,\ldots,13.\ \ n = 1,2,3,\ldots,N.\ \ j = 1,2,3,\ldots,J \qquad (17)$$

$$l \sum_{k=0}^{K} T_{2,\,len,\,n,\,k} \frac{dl_j(\tau_k)}{d\tau} = h_n \left[\frac{m_2}{M_2} \frac{[T_2(len,n,j) - T_2(len+1,n,j)]}{[x_{len} - x_{len+1}]} + \frac{\pi d_o K_o}{M_2 C_{p2}} [T^{wo}{}_{len,\,n,\,j} - T_2(len,n,j)] \right]$$

$$\boldsymbol{len = 1,2,3,\ldots,13.\ n = 1,2,3,\ldots,N.\ j = 1,2,3,\ldots,J} \qquad (18)$$

For all the case studies given in the paper, the discretized models as above are used as constraints after applying for all scenarios of possible uncertainty in solving uncertain Optimal Control Problem (OCP).

Scenario tree based approximation

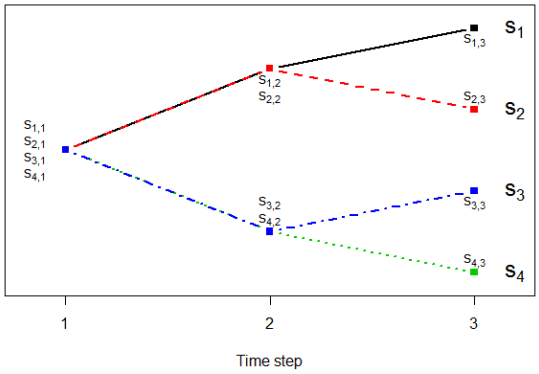

Figure 4. Simple Scenario tree structure

To convert the intractable OCP given by Equations (8)-(12) to tractable, finite number of possible scenarios of uncertainty are considered. For control horizon of N, if S is the possible number of values ζ can take in each interval, total number of scenarios over the entire horizon = S^N.

The constraints of the OCP after applying scenario based approximation are given by,

$$\sum_{j=0}^{K} x_{i,j,s} \frac{dl_j(\tau_k)}{d\tau} = h_i f\left(x_{i,k,s}, t_{ik}\right) \quad (19)$$

$$k = 1,2,..,K \quad i = 1,2,..,N \;\; \forall s \;\; \forall x \in x$$

$$T_{2,o,s} = u_s\left(T_{2,i}\right) - (1-u_s)\, T'_{2,o,s} \quad (20)$$

$$x_{min} \le x_{i,k,s} \le x_{max} \;\; \forall x \in x \quad (21)$$

Robust Counterpart derivation

The constraints given by Equation (11) are modified by deriving robust counterpart after applying affine control policy. The derivation proceeds as following,

The uncertainty in $T_{1,in}$ is modeled as a function of a primitive uncertainty ζ. A and B are bounds of $T_{1,in}$.

$$T_{1,in,i} = A\zeta_i + (1-\zeta_i)B \quad \forall i \quad (22)$$

$$\zeta_i \in [0,1] \;\forall i \quad (23)$$

$$\zeta_i \in \Xi = \{\zeta : W \cdot \xi \ge h^u\} \quad (24)$$

Consider the constraint,

$$\Delta u\,(i,s) \le \Delta u_{max} \qquad i = 1,2,..,N \;\; \forall s \quad (25)$$

Apply Linear Decision rule,

$$\Delta u_i^T \cdot \xi_{i-1} \le \Delta u_{max} \qquad i = 1,2,..,N \quad (26)$$

Here, $\xi_{i-1} = [1; \zeta_1; \zeta_2; \ldots..; \zeta_{i-1}]$
Δu_i^T contains affine rule parameters
To avoid change in dimension of $\boldsymbol{\xi}_{i-1}$ as i changes, the truncate operator is introduced.

$$(\Delta u_i^T \cdot P_i^{\xi}) \cdot \xi \le \Delta u_{max} \quad (27)$$

Robust counterpart and Apply constraint on $\boldsymbol{\xi}$:

$$\left\{ \begin{matrix} \max \\ \xi \\ -W \cdot \xi \le h^u \end{matrix} \left(\Delta u_i^T \cdot P_i^{\xi}\right) \cdot \xi \right\} \le \Delta u_{max} \quad (28)$$

$$i = 1,2,..,N$$

Introduce a dual variable $\boldsymbol{\Lambda}_i$ and apply duality to inner LP problem:

$$\left\{ \begin{matrix} \min \\ \Lambda_i, \Lambda_i \ge 0 \\ -W \cdot \Lambda = \left(\Delta u_i^T \cdot P_i^{\xi}\right)^T \end{matrix} ((-h^u)^T \Lambda_i) \right\} \le \Delta u_{max} \quad (29)$$

$$i = 1,2,..,N$$

Drop the minimization operator

$$\left\{ \begin{matrix} ((-h^u)^T \Lambda_i) \le \Delta u_{max} \\ \Lambda_i \ge 0 \\ -W \cdot \Lambda = \left(\Delta u_i^T \cdot P_i^{\xi}\right)^T \end{matrix} \right\} i = 1,2,..,N \quad (30)$$

Equation (30) is used as constraint in tractable OCP.

Tractable Optimal Control Problem

The final form of Optimal Control Problem, which is tractable is given by,

$$\min_{\boldsymbol{u}} \sum_{i=1}^{N} \sum_{k=0}^{K} \left(T_{2,o,i,k}(\zeta^*) - T_{st}\right)^2 + \sum_{i=1}^{N} \alpha\left(\Delta u\,(\zeta^*, i)\right)^2 \quad (31)$$

s.t.

$$T_{1,in,i} = A\zeta_i + (1-\zeta_i)B \quad (32)$$

$$u(i,s) = \left(u_i^T \cdot P_i^{\xi}\right) \cdot \xi_s^{\,T} \quad (33)$$

$$\sum_{j=0}^{K} x_{i,j,s} \frac{dl_j(\tau_k)}{d\tau} = h_i f\left(x_{i,k,s}, t_{ik}\right) \qquad k = 1,2,..,K$$

$$i = 1,2,..,N \;\; \forall s \;\; \forall x \in \boldsymbol{x} \quad (34)$$

$$T_{2,o,s} = u_s\, T_{2,in} - (1-u_s)\, T'_{2,o,s} \quad (35)$$

$$x(0) = x_o \quad (36)$$

$$x_{min} \le x_{i,k,s} \le x_{max} \;\; \forall x \in x \quad (37)$$

$$\left\{ \begin{matrix} \left((-\boldsymbol{h}^u)^T \boldsymbol{\Lambda}_i^1\right) \le \Delta u_{max} \\ \boldsymbol{\Lambda}_i^1 \ge \boldsymbol{0} \\ -W \cdot \boldsymbol{\Lambda}^1 \le \left(\Delta \boldsymbol{u}_i^T \cdot P_i^{\xi}\right)^T \end{matrix} \right\} i = 1,2,..,N \quad (38)$$

$$\left\{ \begin{matrix} \left((-\boldsymbol{h}^u)^T \boldsymbol{\Lambda}_i^2\right) \le -\Delta u_{min} \\ \boldsymbol{\Lambda}_i^2 \ge \boldsymbol{0} \\ -W \cdot \boldsymbol{\Lambda}^2 \le \left(-\Delta \boldsymbol{u}_i^T \cdot P_i^{\xi}\right)^T \end{matrix} \right\} i = 1,2,..,N \quad (39)$$

The decision variables are Affine rule coefficients. This Optimal Control Problem in solved in receding horizon approach to implement uncertain Model Predictive Control of HEN.

CASE STUDIES

The performance of the proposed control method is demonstrated using two case studies. First is simple Heat Exchanger, and second is a Heat Exchanger Network. The optimization is done in GAMS 25.1.1, and overall MPC is implemented using MATLAB 2020a. The parameters of the Heat Exchanger and the streams are given in

Single Heat Exchanger

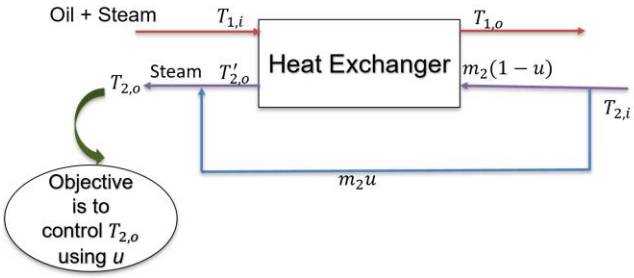

Figure 5. Single Heat Exchanger system

The decision variable (bypass fraction of cold stream) is obtained by optimizing the uncertain OCP given in section 0. Four scenarios of possible uncertainty are used in optimization to obtain the value od decision variable. The prediction-horizon of 20 is divided into 2 finite elements. The scenarios used in optimization i.e. possible scenarios of inlet temperature profiles of hot stream is given by **Figure 6.** Hot stream temperature profiles for the scenarios used in optimization**Figure 6**. The corresponding bypass fraction profiles (decision variables) is given by **Figure 7**. The control variable profiles for the scenarios used in optimization is given by **Figure 8**. It shows that for the scenarios used in optimization, the control variable simulated using optimum input tracks the setpoint efficiently.

To test the performance of the decision variables obtained four random testing scenario profiles of the inlet temperature of the hot stream are considered. These profiles are given by **Figure 9**. The control variable profiles obtained for the testing scenarios simulated using input from uncertain optimization is given by **Figure 10**. As expected, the control variable deviates little from the setpoint because these scenarios are not used in optimization. To compare the performance of the uncertain MPC, the control variable profiles are generated using deterministic input for the testing scenarios. The corresponding graph is given by **Figure 11**. The **Figure 11** shows the control variable deviates from the setpoint as time passes using deterministic input. So the uncertain MPC has advantage over deterministic MPC.

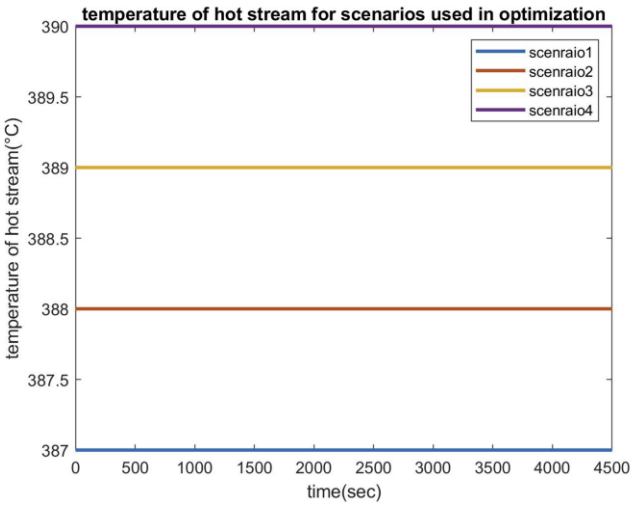

Figure 6. Hot stream temperature profiles for the scenarios used in optimization

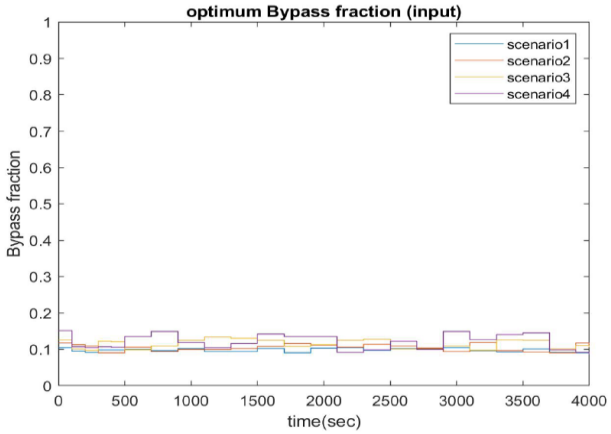

Figure 7. Optimum bypass fraction profiles for the scenarios used in optimization

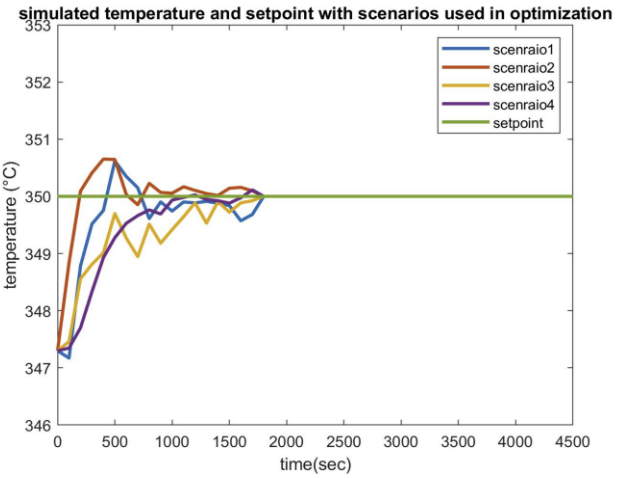

Figure 8. Control variable Profile for the scenarios used in optimization and input of uncertain optimization.

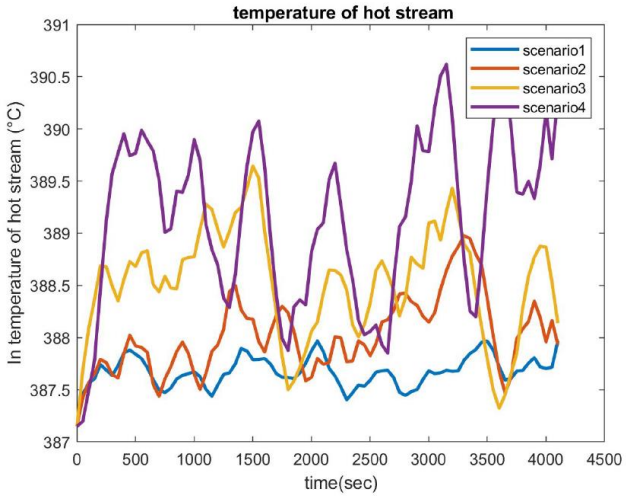

Figure 9. Scenarios used for testing of proposed control method

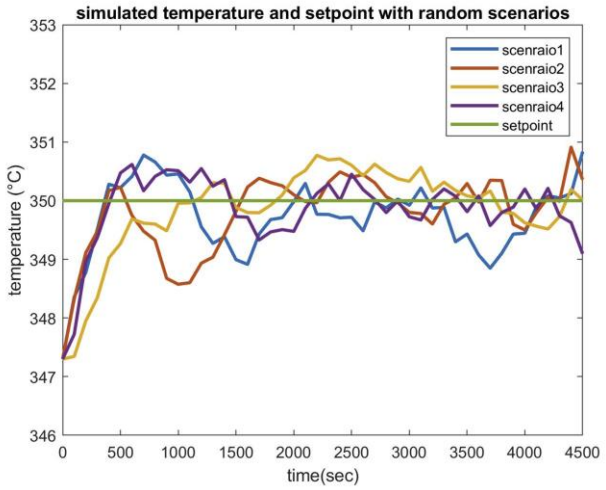

Figure 10. Control variable profiles obtained using testing scenarios and input of uncertain optimization

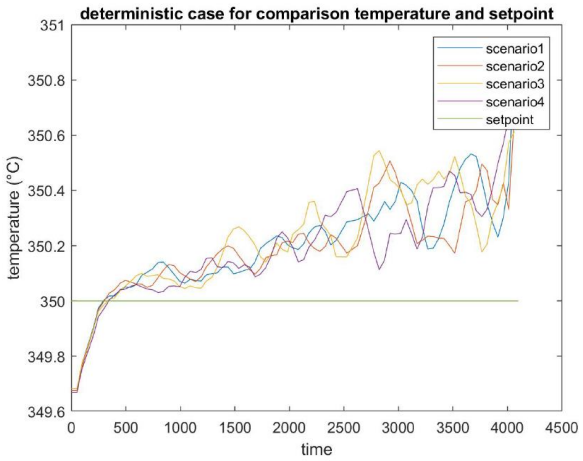

Figure 11. Control variable profiles obtained using testing scenarios and input of deterministic optimization

Heat Exchanger Network

The HEN considered for second case study of the current research work is given by **Figure 12**. This HEN is adopted from [1].

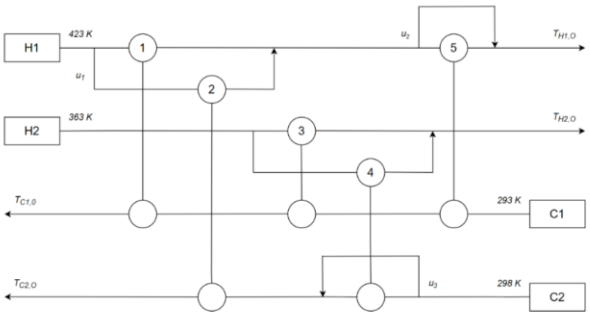

Figure 12. Heat Exchanger Network for the second case study

For the HEN also, four scenarios of possible uncertainty are used in optimization to obtain the value od decision variable. The prediction horizon of 40 is divided into 2 finite elements. For this case study, we consider disturbances in H1 stream, and the control variable is out temperature of C2 stream. The scenarios used in optimization i.e. possible scenarios of inlet temperature profiles of hot stream is given by **Figure 13**. The corresponding bypass fractions profiles are given by **Figure 14**, **Figure 15**, and **Figure 16**. The control variable profiles (the out temperatures of C2 stream) for the scenarios used in optimization is given by **Figure 8**.

To test the performance of the decision variables obtained four random testing scenario profiles are considered, and these profiles are given by **Figure 18**. For a step change in setpoint, the control variable profiles obtained for the testing scenarios simulated using input from uncertain optimization is given by **Figure 19**. For the step change in setpoint, the control variable profiles are generated using deterministic inputs for the testing scenarios. The corresponding graph is given by **Figure 11**, which shows the control variable deviates from the setpoint as time passes using deterministic inputs.

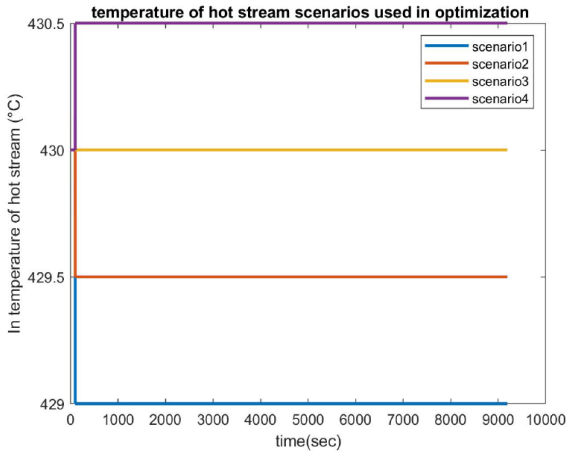

Figure 13. Hot stream (H1) temperature profiles for the scenarios used in optimization

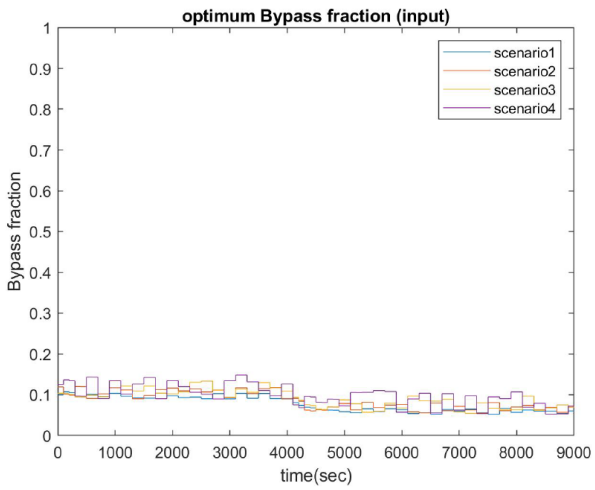

Figure 14. Optimum bypass fraction profiles of u_1 stream for the scenarios used in optimization

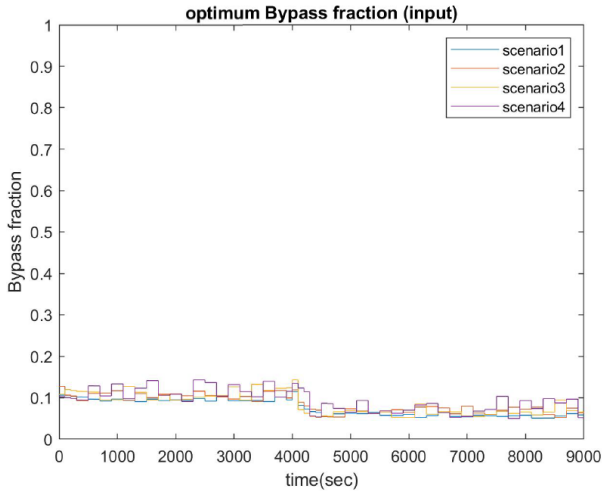

Figure 15. Optimum bypass fraction profiles of u_2 stream for the scenarios used in optimization

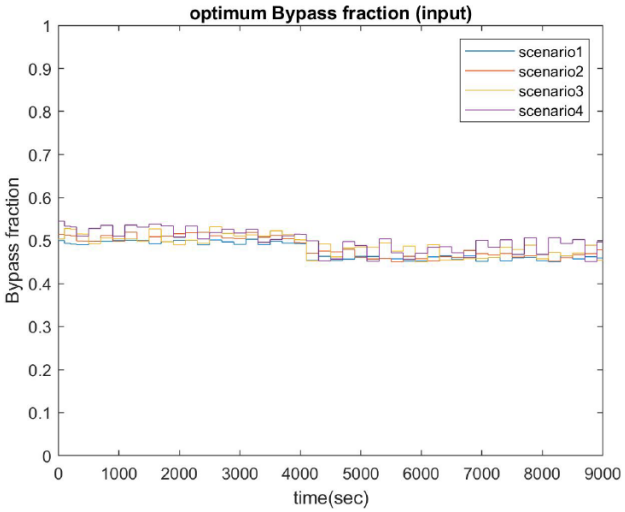

Figure 16. Optimum bypass fraction profiles of u_3 stream for the scenarios used in optimization

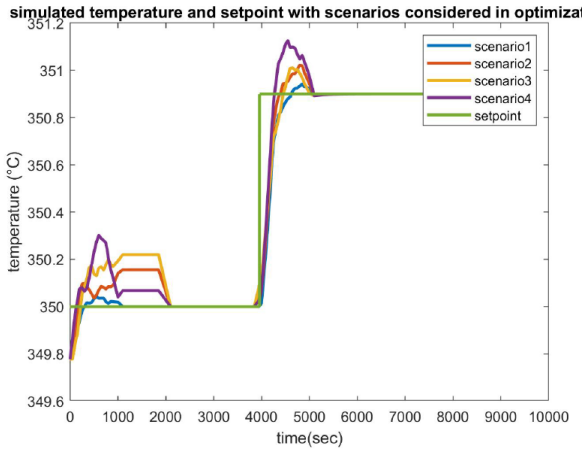

Figure 17. Control variable Profile (C2 out temperature) for the scenarios used in optimization and input of uncertain optimization.

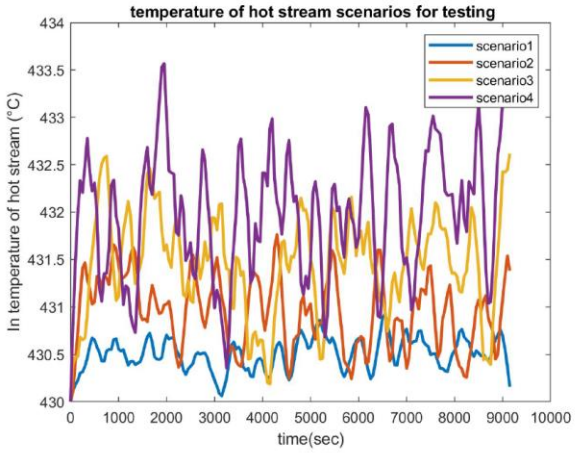

Figure 18. Scenarios used for testing of proposed control method (in temperatures of H1 stream)

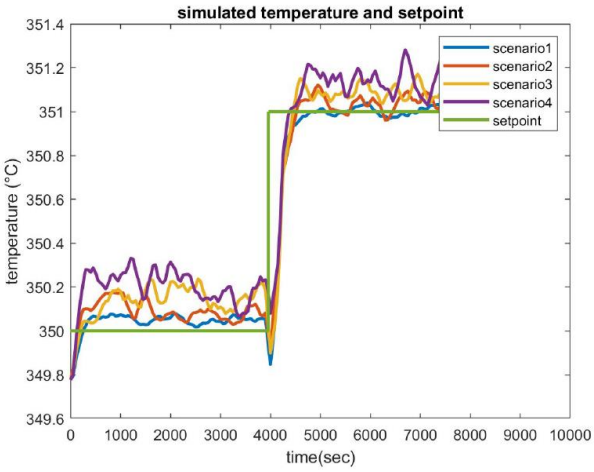

Figure 19. Control variable profiles obtained using testing scenarios and input of uncertain optimization

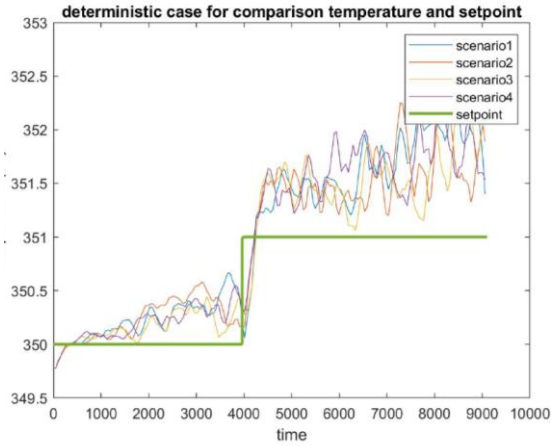

Figure 20. Control variable profiles obtained using testing scenarios and input of deterministic optimization

Table 1: Parameters of the Heat exchanger and the streams.

Parameter	symbol	Value
Hot stream Flowrate	m_1	3.93 (kg/s)
cold stream Flowrate	m_2	30.95 (kg/s)
Specific heat capacity of hot stream	C_{p_1}	4 ((kJ/(kg.K)))
Specific heat capacity of cold stream	C_{p_2}	2.5 (kJ/(kg.K))
heat exchage area	S	230 (m^2)
Outer diameter of tube	d_o	25 (mm)
Inner diameter of tube	d_i	22.5 (mm)

NOMENCLATURE

Name	symbol
heat transfer coefficient at outer wall	k_o
heat transfer coefficient at inner wall	k_i
Overall heat transfer coefficient	K
mass of wall of Heat Exchanger	M_w
Heat transfer rate	Q
fouling resistance of outer wall of Heat Exchanger	R_o
fouling resistance of inner wall of Heat Exchanger	R_i
tube outer radius	r_o
tube inner radius	r_i
temperature of hot stream at inlet of Heat Exchanger	$T_{1,i}$
temperature of hot stream at outlet of Heat Exchanger	$T_{1,o}$
temperature of cold stream at inlet of Heat Exchanger	$T_{2,i}$
temperature of cold stream at outlet of Heat Exchanger	$T'_{2,o}$
temperature of mixed stream	$T_{2,o}$
Temperature of outer wall of Heat Exchanger	T_{wo}
Setpoint of temperature of mixed stream	T_{st}
time coordinate	t
Temperature of inner wall of Heat Exchanger	T_{wi}
Bypass fraction	u
Thermal conductivity of wall	λ
Weighing term for Controller effort	α

ACKNOWLEDGEMENTS

The authors would like to acknowledge the following for sponsoring the research,

- Computer Process Control group, University of Alberta
- Natural Sciences and Engineering Research Council of Canada.

REFERENCES

1. Sun L, Zha X, Luo XL. Coordination between bypass control and economic optimization for heat exchanger network. *Energy* 160:318-329 (2018).
2. Ehlinger V, Mesbah A. Model Predictive Control of Chemical Processes: A Tutorial. In: Coulson and Richardson's Chemical Engineering. Ed: Chhabra Rp, Shankar V. Elsevier. p367-402 (2017)
3. Luo XL, Xia C, Sun L. Margin design, online optimization, and control approach of a heat exchanger network with bypasses. *Computers & Chemical Engineering* 53:102–121 (2013).
4. Mohankumar Y, Li Z, Huang B. Steam allocation and production optimization in SAGD reservoir under steam-to-oil ratio uncertainty. *J Petrol Sci Eng* 183: 106456 (2019)
5. Wang YF, Chen Q. A direct optimal control strategy of variable speed pumps in heat exchanger networks and experimental validations. *Energy* 85: 609-619 (2015)
6. Skorospeshkin MV, Sukhodoev MS, Skorospeshkin VN. An adaptive control system for a shell-and-tube heat exchanger. *J Phys Conference Series* 803:012153 (2016).
7. Delatore F, José J, Fabrizio L, Novazzi L. Multivariable Optimal Control of a Heat Exchanger Network (HEN) With Bypasses. *IASTED Technol Conf* 697-062 (2010)

This conference proceeding has not been peer reviewed.

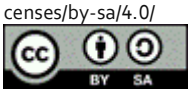

CSChE Systems & Control Transactions

Open Access | Original Research

Conference Proceedings
Canadian Chemical Engineering Conference 2021
October 24-27, Montréal, Québec, Canada

PSEcommunity.org/LAPSE:2021.0795

PSE PRESS

Purification Methods for Captured CO_2 from Petroleum Coke Oxy-Combustion Power Plants

Tia Ghantous.[a], Ikenna J. Okeke[a,b], and Thomas A. Adams II[b]*

[a] Department of Chemical Engineering, McMaster University, 1280 Main St. W, Hamilton, ON, Canada, L8S 4L7.
[b] Department of Civil and Mineral Engineering, University of Toronto, 35 St. George Street, Toronto, ON, Canada, M5S 1A4.

* Corresponding Author: tadams@mcmaster.ca.

ABSTRACT

We present eco-technoeconomic analyses of four processes, including two novel designs, for the purification of captured CO_2 from flue gas for a petroleum coke (petcoke) oxy-combustion power plant operated with carbon capture and sequestration (CCS). A base case petcoke oxy-combustion design obtained from a previous study consisting of flue gas water removal using condensation was used in this study. Other purification processes evaluated consist of a cryogenic distillation petcoke oxy-combustion with CCS, an oxygen deficient petcoke oxy-combustion with CCS and a catalytic dehydration petcoke oxy-combustion via hydrogen conversion with CCS. An eco-technoeconomic analysis considering greenhouse gas (GHG) emissions, levelized cost of electricity (LCOE), thermal efficiency and CO_2 product purity to meet pipeline specifications, was conducted on all purification candidates. This revealed that base case design did not meet the CO_2 pipeline specifications. The highest LCOE was attributed to the cryogenic distillation design, although it produces the purest CO_2 product compared to all other designs. The oxygen-deficient design has the lowest LCOE and GHG emission, proving to be a desirable candidate, however further research is required to determine the feasibility associated with the incomplete combustion of fuels. The catalytic deoxygenation design appears to be a middle ground between the latter two designs, with a lower LCOE than the cryogenic design and a higher purity CO_2 product compared to the oxygen deficient design. In brief, this study presents and performs eco-technoeconomic analyses of four candidates for the purification of captured CO_2 from petcoke oxy-combustion power plants while respecting pipeline specifications, the first of its kind to do so.

Keywords: petroleum coke, eco-technoeconomic analysis, captured CO_2, oxy-combustion

Date Record: Original manuscript received October 18, 2021. Published October 21, 2021.

INTRODUCTION

Oxy-combustion consists of burning fuels in the presence of oxygen at very high concentrations and recirculating the flue gas to produce a flue gas largely composed of CO_2 at a high temperature. The purified CO_2 product is then fed into pipelines and sent to CO_2 sequestration sites to be used for various purposes, namely enhanced oil recovery, etc. An important concern in the transportation of the captured CO_2 is the oxygen specification of the pipeline, which if overlooked, could have detrimental effects on these pipelines. However, in investigating recent studies, it was determined that many fail to consider the oxygen specification of pipelines. By doing so, they generate inaccurate eco-technoeconomic analysis studies which underestimates costs and environmental impacts as well as overshoots the plant's performance and efficiency.

This study considers four designs for the purification of captured CO_2 from a petroleum coke (petcoke) oxy-combustion power plant operated with carbon capture and sequestration (CCS). These four designs are a base case petcoke oxy-combustion with CCS, a cryogenic distillation petcoke oxy-combustion with CCS, an oxygen deficient petcoke oxy-combustion with CCS and a catalytic dehydration petcoke oxy-combustion with CCS. The Kinder Morgan pipeline specifications which indicate a maximum oxygen level of 10 ppm, among other component specifications, will be used as a guideline to avoid pipeline corrosion [1].

Readers are referred to [2] for full details.

METHODS

The purification methods presented are evaluated at a net power output of 550 MWe. All the following designs were simulated using Aspen Plus V10 using the Peng-Robinson with the Boston-Mathias alpha function (PR-BM) property package. However, the property package used to simulate the steam/power generation, CO_2 capture and compression including CO_2-H2O separation, and the CO_2 dehydration via

TEG absorption were Predictive Redlich-Soave (PSRK), STEAMNBS and HYSGLYCO respectively. The properties of the delayed petcoke are displayed in Table 1 was modeled as a solid non-conventional substance pseudo-component.

Aspen Plus APV100 Pure-36 databases were used to model the conventional chemicals while the non-conventional substance pseudo-component model was used for the delayed petcoke, with properties shown in Table 1.

Table 1: Delayed petcoke properties.

	Delayed coke
HHV (MJ/kg)	34.7
Ultimate analysis (wt % dry)	
C	84.9
H	3.9
N	1.3
S	6
Cl	0
Ash	3.1
O (diff)	0.8
Proximate analysis (wt %)	
Moisture	1.8
Volatile matter	11.9
Fixed Carbon	83.3
Ash	3

Base case oxy-combustion

This design and corresponding model is the base case oxy-combustion model from a previous study [3]. Petcoke is crushed and mixed with water to form a petcoke slurry which is then combusted in the oxycombustor in the presence of high purity oxygen, obtained from the air separation unit (ASU), at stoichiometric ratio to obtain the flue gas. A heat recovery steam generator (HRSG) is used to generate electricity from steam at different pressures using a steam cycle accompanied by a cooling tower. Flue gas desulfurization (FGD) utilizing a limestone slurry is also employed in this process to treat the flue gas as a result of the formation of sulfur compounds within the oxycombustor. Following FGD, the flue gas is cooled to 21°C and fed through a cascade of flash drums operating at decreasing pressures to remove water at 99 mol% purity resulting in minimal loses. It is at this point that the following designs will differ from the base case, as the flue gas will undergo further methods of purification. In this case, the flue gas exiting the flash cascade at 9 bar, now largely composed of CO_2 along with minor impurities, is compressed to pipeline conditions of 153 bar. This design, however, does not meet the Kinder Morgan O_2 specifications, therefore it is rejected as a possible purification method. Further details about this design are presented in prior work [3].

Cryogenic distillation purification oxy-combustion

The cryogenic distillation purification model was also acquired from a previous study [3]. This process differs from the base case following the flue gas' exit from the cascade of flash drums at 21°C and 9 bar. The impure CO_2 is compressed to 30 bar and cooled to 9°C using a series of heat exchangers, which minimizes the duty requirements prior to distillation. The impure CO_2 is then fed into a cryogenic distillation column with the desired bottoms output of 10 ppm of oxygen. It is important to note that a greater CO_2 recovery is limited by a greater energy cost, of which a lower energy cost was favoured. Therefore, only 95% CO_2 capture was achieved due to losses with the oxygen distillate stream that was vented into the atmosphere. Further details about this design are presented in prior work [3].

Oxygen deficient oxy-combustion

This design follows a similar structure as the base case design, however it utilizes less oxygen within the oxycombustor, rather than using oxygen at a stoichiometric ratio, to meet the Kinder Morgan pipeline requirement of 10 ppm. Chemical equilibrium was assumed when simulating this design. Alternatively, sub-equilibrium conditions would ensue a greater amount of uncombusted gas in the product as well as lower efficiencies.

Catalytic de-oxygenation oxy-combustion

Another novel design presented in this study is CO_2 purification via catalytic de-oxygenation, presented in Figure 1. The impure CO_2 obtained at 21°C and 9 bar from the flash drum cascade is heated to 150°C and is fed into a de-oxygenation reactor with a hydrogen inlet. The excess oxygen (above 10 ppm) will catalytically react with hydrogen to form water, as shown in Equation 1. A study conducted by Deshpande et al. presented a catalyst ($Ce_{0.83}Ti_{0.15}Pd_{0.02}O_{2-\delta}$) that can achieve a 97% hydrogen conversion at 150°C and atmospheric pressure [4]. Therefore, this reaction was assumed to achieve 97% conversion of hydrogen with this catalyst while operating at 9 bar, since a greater pressure would push the reaction forward. A design specification was used to modify the inlet hydrogen flow rate to allow an outlet concentration of O_2 below 10 ppm within the impure CO_2 gas. This reaction produces a large amount of water, which in turn exceeds the Kinder Morgan specification of 690 ppm and requires further treatment for water removal [1]. The stream is then cooled to 35°C and fed into a flash drum to knock out 99.9 mol% water, however since it still exceeds the pipeline requirements, it is compressed to 41 bar using a multistage compressor with intercoolers and enters the TEG dehydration cycle.

$$O_2(g) + 2H_2(g) \leftrightharpoons 2H_2O\ (g) \quad (1)$$

The TEG dehydration cycle in Figure 2 allows for the removal of excess water in the stream. This dehydration cycle utilizes TEG since it acts as a drying agent on account of its high affinity for water. Impure CO_2 at 41 bar and 35°C enters the bottom of absorption column in which TEG at the same conditions is fed at the top to strip the CO_2 of water. In this column, the TEG absorbs the water from the water rich gas to become rich TEG, exiting from the bottom of the column, and dry gas, exiting from the top. The CO_2 recovered from the top is greater than 98% pure. The water-rich TEG undergoes further processing to recover and recycle TEG, avoiding additional material costs. A valve is used to decompress the water-rich TEG and it enters a flash drum to separate any accompanying gases, containing high purity CO_2. These gases are compressed to match the conditions of the CO_2 product from the

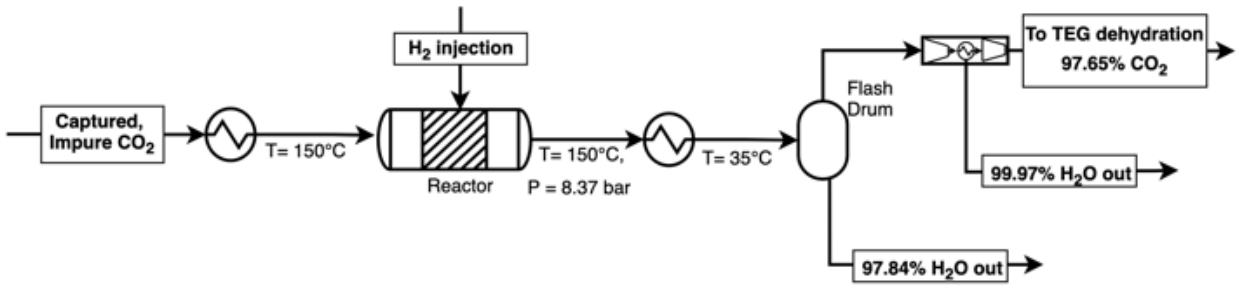

Figure 1: Process flow diagram for the catalytic de-oxygenation of captured CO_2.

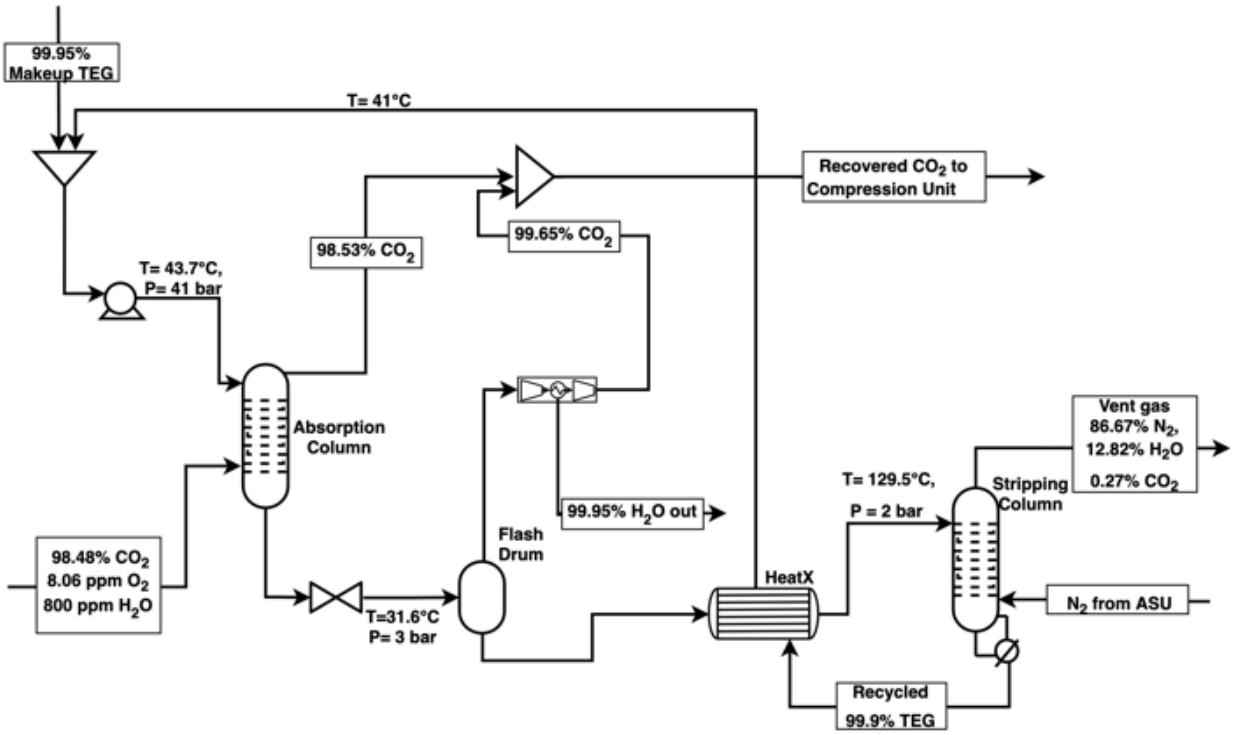

Figure 2: Process flow diagram for the TEG dehydration cycle of the captured CO_2.

absorber using a multistage compressor with interstage cooling, with which they will be mixed, and they are further compressed to pipeline conditions of 153 bar.

The water-rich TEG is then heated and enters the top of a stripping column while nitrogen, recovered from the ASU, is fed into the bottom as a stripping gas. The stripping column has a reboiler that operates at a boilup ratio of 0.8 but it does not have a condenser. The distillate exiting the top of the column is vented to the atmosphere since it is largely made up of nitrogen and water. The lean TEG obtained from the bottom of the column is 99.9% pure, it is cooled and pumped to 41 bar to be recycled back to the system. A makeup TEG stream is used to account for minor TEG losses within the cycle.

RESULTS

The performance of all four designs were evaluated for a net power of 550MW and the results are displayed in Table 2.

The total power generation is highest for the cryogenic distillation design compared to the others, due to its higher parasitic load which requires a more power generation to attain 550MW. The cryogenic distillation design also has a higher direct GHG emission compared to other designs on account of the CO_2 lost in the distillate vent gases, as previously mentioned, which in turn reduces its CO_2 sequestration ratio. The oxygen deficient and catalytic de-oxygenation designs exhibit nearly 100% CO_2 capture and fewer emissions, and subsequently have a higher sequestration ratio and lower direct GHG emissions. However, the catalytic de-oxygenation design has significantly higher indirect GHG emissions compared to the other designs, which is associated with the assumption that the hydrogen used in the de-oxygenation reactor was obtained from a steam methane reforming process operated without CCS [5]. Hence, the emissions from this process must be accounted for. Altogether, the latter design has the highest total GHG emissions.

Table 3 presents the product stream conditions for all four designs. As previously mentioned, the base case design

Table 2: Performance summary of each purification design.

Parameters	Base case	Cryogenic distillation	Oxygen deficient	Catalytic de-oxygenation
CCS Enabled	Yes	Yes	Yes	Yes
Petcoke feed rate (tonne/h)	183.5	193.3	192.6	185.6
Petcoke feed capacity (MWHHV)	1769	1863	1856	1789
Total power generated (MW)	733	772	735	742
Total parasitic load (MW)	183	221	185	192
Net power output (mW)	550	550	550	550
Heat rate (MJHHV/MWh)	11,577	12,196	12,150	11,712
Thermal Efficiency (%HHV)	31.1	29.5	29.6	30.7
Direct GHG Emissions ($kgCO_2eq/MWh$)	0.46	54.7	0.49	0.46
Indirect GHG Emissions ($kgCO_2eq/MWh$)	0.17	0.18	0.18	57.4
Total GHG Emissions ($kgCO_2eq/MWh$)	0.63	54.9	0.66	57.9
CO_2 sequestered (tonne/h)	596	567	600	582
CO_2 sequestered ratio (tonne CO_2/tonne petcoke)	3.25	2.93	3.12	3.14

Table 3: Composition of captured CO_2 stream for each purification design.

	Kinder Morgan Pipeline Spec	Base case	Cryogenic distillation	Oxygen deficient	Catalytic de-oxygenation
CCS Enabled		Yes	Yes	Yes	Yes
Meets pipeline Spec?		No	Yes	Yes	Yes
H_2O	690 ppm	337 ppm	401 ppm	337 ppm	314 ppm
CO_2	>95%	95.1%	99.9%	97.6%	98.5%
H_2S	10-200 ppm	trace	trace	trace	trace
CO	no spec	trace	trace	1.00%	trace
C_xH_y	<5%	trace	trace	trace	trace
H_2, N_2, Ar	<4%	1.34%	0.44 ppm	1.37%	1.4%
O_2	<10ppm	3.49%	9.40 ppm	9.41 ppm	8.06 ppm
NO_2	no spec	0.28 ppm	0.31 ppm	0.12 ppm	0.27 ppm
N_2O	no spec	0.01 ppm	0.01 ppm	0.01 ppm	0.01 ppm
SO_2	no spec	305 ppm	338 ppm	317 ppm	316 ppm
SO_3	no spec	0.72 ppm	0.80 ppm	0.47 ppm	0.72 ppm

Table 4: LCOE of each purification design with/without carbon tax and T&S.

	Base case	Cryogenic distillation	Oxygen deficient	Catalytic de-oxygenation
CCS Enabled	Yes	Yes	Yes	Yes
LCOE w/o carbon tax and w/o T&S	90.94	102.8	92.28	97.67
LCOE w/o carbon tax and with T&S	104.7	115.9	105.8	110.9
LCOE with carbon tax and w/o T&S	90.96	105.5	92.31	97.69
LCOE with carbon tax and with T&S	104.8	118.7	105.9	111

does not meet the pipeline requirements and it has been rejected. The cryogenic distillation design provides the highest product CO_2 purity compared to all other purification methods, making it a desirable design for when CO_2 purity is essential. Higher concentrations of unconverted fuels, such as CO and H_2, in the product stream of the oxygen deficient design is attributed to its incomplete combustion in the presence of oxygen below the stoichiometric ratio. These components are still within their respective specifications, and therefore this design remains satisfactory.

Table 4 presents the levelized cost of electricity (LCOE) for all four plant designs with the varying constraints of carbon tax and transportation and storage (T&S). Omitting both constraints, the base case design has the lowest LCOE followed by the oxygen deficient, catalytic de-oxygenation and the cryogenic distillation, which is the highest. When T&S is considered, the designs with the highest capture rates observe a more significant LCOE increase compared to the design with the lowest capture rate, cryogenic distillation. If a carbon tax of $50 per tonne of CO_2eq is applied without T&S, the cryogenic distillation design is greatly impacted due to its loss of CO_2 with vent gases. Applying both the carbon tax and the T&S cost indicated that the highest LCOE belongs to the cryogenic

distillation design followed by the catalytic de-oxygenation, oxygen deficient and base case, in decreasing LCOE order.

CONCLUSIONS

Although the base case design was the most efficient and cost-effective design, it did not meet the oxygen limit pipeline requirements and was excluded from the rest of the analysis. While the oxygen deficient design showed promising efficiencies, LCOE and total GHG emissions, the assumption that chemical equilibrium was attained under incomplete combustion must be evaluated to determine if these results are feasible at an industrial scale. The cryogenic distillation design achieves a very high final CO_2 purity, but has the highest LCOE compared to all the designs. This design would be advantageous if the product purity was of the utmost importance, such as the product would be sold for example. Finally, the catalytic de-oxygenation design was determined to be the most efficient design and has a lower LCOE than the cryogenic distillation design, while maintaining a high purity CO_2 product. However, it has higher indirect GHG emission associated with the H_2 injection within the de-oxygenation reactor. In brief, the three viable designs been presented in this study have their own trade-offs. Further details regarding the results of this study are presented in a manuscript pending publication [2].

Future work would entail the investigation of other purifications, such as catalytic methane oxidation, that would avoid any trade-offs to reduce GHG emissions, maintain a low LCOE and meet pipeline requirements.

ACKNOWLEDGEMENTS

The authors received funding for this research via an NSERC Discovery grant (RGPIN-2016-06310) and an Ontario Research Fund – Research Excellence Grant (RE09-058)

REFERENCES

1. De Visser E, Hendriks C, Barrio M, Molnvik MJ, de Koeijer G, Liljemark S, Le Gallo Y. *Dynamis CO_2 quality recommendations. Int J Greenhouse Gas Control* 2:478-484 (2008)
2. Okeke IJ, Ghantous T, Adams TA II. Design strategies for oxy-combustion power plant captured CO_2 purification. Submitted to *Chem Prod Process Mod* (2021)
3. Okeke IJ, Adams TA II. Advanced Petroleum Coke Oxy-Combustion Power Generation with Carbon Capture and Sequestration: Part I - Design and Techno-Economic Analysis. *Canadian J Chem Eng* 2021:1-16 (2021).
4. Deshpande PA, Madras G. Catalytic hydrogen combustion for treatment of combustible gases from fuel cell processors. *Applied Catalysis B: Environmental* 100: 481-490 (2010)
5. GREET Model. A fresh design for GREET life cycle analysis tool. 2017 Available from: https://greet.es.anl.gov/index.php?content=greetdotnet

This conference proceeding has not been peer reviewed.

CSChE Systems & Control Transactions

Open Access | Original Research

Conference Proceedings
Canadian Chemical Engineering Conference 2021
October 24-27, Montréal, Québec, Canada

PSEcommunity.org/LAPSE:2021.0796

PSE PRESS

Adaptive State Feedback Stabilization of Generalized Hamiltonian Systems with Unstructured Components

Seyedabbas Alavi, Nicolas Hudon*

Queen's University at Kingston, Department of Chemical Engineering, Kingston, Ontario, Canada
* Corresponding Author: nicolas.hudon@queensu.ca.

ABSTRACT

This paper considers the problem of adaptive state feedback controller design for stabilizing the generalized Hamiltonian systems with unstructured components. This class of models enables one to exploit the dissipative-conservative structure of generalized Hamiltonian systems for feedback control design while relaxing the burden of deriving an exact structured model representation. First, an efficient adaptation law is designed such that a correct value of parameters is estimated. Assuming that the overall system is stabilizable, and under mild assumptions on the unstructured part of the dynamics, a stabilizing adaptive control law is designed to stabilize systems to the desired steady-state. The stability of the closed-loop system is demonstrated using Lyapunov stability arguments. A numerical illustration of the proposed approach is presented to demonstrate the potential of the design method.

Keywords: Adaptive stabilization, Hamiltonian system, parameter estimation, Lyapunov stability

Date Record: Original manuscript received October 20, 2021. Published October 21, 2021

INTRODUCTION

Port-Hamiltonian (pH) systems (or generalized Hamiltonian systems) have attracted the attention of many researchers in recent years as a modelling framework useful for feedback control design and analysis. The structured properties of this system facilitate the stability and tracking controller design for dynamical systems [1,2]. In applications, however, controller performance and stability properties can be lost due to model uncertainties, noise in sensors readings, input disturbance, and parameter uncertainties. As well, for a given nonlinear system, it is often difficult to compute an exact (or standard) generalized Hamiltonian representation.

Studies on feedback stabilization of approximate Hamiltonian systems were presented in [3,4] by exploiting a homotopy-based decomposition. This approach exploits the geometric structure of the anti-exact part of the dynamics. In the present note, we follow this general approach to generalized Hamiltonian systems stabilization by considering the problem of adaptive state feedback stabilization of control affine nonlinear systems where one part of the dynamics can be represented as a structured system with quadratic Hamiltonian generating function and the remaining of the dynamics is unstructured. Using this approximate representation, and under mild assumptions on the stabilizability of the overall dynamics and on the norm of the unstructured dynamics, an adaptive stabilizing state feedback law is designed based on the structured part of the dynamics.

PROBLEM FORMULATION

We consider control affine systems with parametric uncertainties, i.e.,

$$\dot{x} = f(x,\theta) + g(x)u, \tag{1}$$

where $\theta \in R^l$ is the constant parametric uncertainty.

Assumption 1: System (1) is locally stabilizable for fixed parameter θ, i.e.,

$$span\{f(x), ad_f g(x), \cdots, ad_f^k g(x) | \forall x \in \{D\}\backslash\{0\}, k \in Z_+\} = \mathbb{R}^n, \tag{2}$$

where ad_f^k is the Lie bracket operator [5].

Following [6], it is possible to express system \eqref{eq:affpar} as a pH system with dissipation

$$\dot{x} = [J(x,\theta) - R(x,\theta)]\nabla H(x,\theta) + g(x)u. \tag{3}$$

However, finding an exact transformation to express system (1) as the generalized Hamiltonian system (3) is not always possible, therefore, we consider the parameter-dependent version of a generalized Hamiltonian system with unstructured dynamics

$$\dot{x} = [J(x,\theta) - R(x,\theta)]\nabla H(x) + \Psi(x,\theta) + g(x)u, \tag{4}$$

where the generating Hamiltonian function is selected to be quadratic and not a function of the unknown parameters, i.e.,

$H(x) = \frac{1}{2}x^T x$. This can be achieved by choosing a positive definite $R(\cdot)$ and skew-symmetric $J(\cdot)$ and leaving the rest as the unstructured part of the dynamic $\Psi(x,\theta)$s.

In the sequel, we demonstrate that the proposed representation can be exploited in the derivation of a suitable state feedback adaptive stabilizing control law, under mild assumptions on the unstructured part of the dynamics Ψ. The key assumption is that the system (4) (equivalently system (1)) is stabilizable for fixed unknown parameters θ. Moreover, we make the following assumption of the unstructured component of the dynamics $\Psi(x,\theta)$.

Assumption 2: The unstructured vector $\Psi(x,\theta)$ has Lipschitz property in x and θ, and meets the inequality

$$|\Psi(x,\theta)| \leq q(x,\theta)|R(x,\theta)\nabla H(x)| \quad \forall x \in \mathcal{D}\backslash\{0\}, \qquad (5)$$

where $\mathcal{D} \subset \mathbb{R}^n$ is a domain of interest centred at the origin and the state-dependent bound is bounded locally by a constant, i.e., $q(x,\theta) \leq q$ on $\mathcal{D}$.

In other words, the contribution of the unstructured part of the dynamics must be bounded by the natural dissipation of the system, encoded in the structured part of the dynamics.

Following [7-9], we state the following assumption on the drift vector.

Assumption 3: There is a vector function $P(x) \in R^{n\times l}$ and $Q(x) \in R^n$ such that

$$[J(x,\theta) - R(x,\theta)]\nabla H(x) = P(x)\theta + Q(x), \qquad (6)$$

where θ is a l dimensional constant parameter vector.

This assumption can be, up to a re-parameterization, met in practice, at least locally.

ADAPTIVE STABILIZING CONTROLLER DESIGN

Although we know the unstructured component, we do not use it in development of the controller. The main goal is to use the strucutured component along with the *information* about the unstructured component for stability analysis. We consider the Hamiltonian function $H(x) = \frac{1}{2}x^T x$, hence, $\nabla H(x) = x$. Using Assumption 3, we can write the system (4) as

$$\dot{x} = P(x)\theta + Q(x) + \Psi(x,\theta) + g(x)u, \qquad (7)$$

We do not have access to the true value of parameters for the controller formulation. To develop a feedback adaptive stabilizing control law, we consider the estimation $\hat{\theta}$ of the parameters. The estimated parameters is used to generate an auxiliary system as given below

$$\dot{\check{x}} = P(x)\hat{\theta} + Q(x) + \Psi(x,\hat{\theta}) + \Lambda(x - \check{x}) + g(x)u, \qquad (8)$$

where $\Lambda \in R^{n\times n}$ is a positive square diagonal matrix with entries to be assigned freely. We use the information generated by this auxiliary system to obtain a precise value for the unknown parameter. We define the estimation error by $\bar{x} = x - \check{x}$. Consequently, we obtain the following estimation error dynamic $\dot{\bar{x}} = \dot{x} - \dot{\check{x}}$ given by

$$\dot{\bar{x}} = P(x)\tilde{\theta} + \Phi - \Lambda(x - \check{x}), \qquad (9)$$

where $\Phi = \Psi(x,\theta) - \Psi(x,\hat{\theta})$, and the parameter estimation error is denoted by $\tilde{\theta} = \theta - \hat{\theta}$. One important requirement in parameter estimation is the persistent excitation in closed-loop, which is provided by making the reference signal rich enough. This requirement, however, could be *weakened* in nonlinear systems since the inherent nonlinearity of the system improves the system excitation, thus enhancing parameter convergence [10].

We are considering the case that the unknown parameter appears in the unstructured part of the dynamic. Since we do not use the unstructured component in the controller design, we need to make the reference signal rich enough to guarantee the Persistent Excitation (PE) condition. This allows recovering the true value for the unknown parameter θ.

Adaptive stabilization at the non-zero steady-state

We firstly present the results for the stabilization of the system at non-zero equilibrium points. The Hamiltonian function, centred at x^*, is expressed by.

$$H(x - x^*) = \frac{1}{2}(x - x^*)^T(x - x^*), \qquad (10)$$

We consider the controller of the form

$$u = \alpha(x, d, \hat{\theta}) + K_I(x)\xi$$
$$\dot{\xi} = -K_I^T(x)g^T(x)\nabla H(x - x^*) \qquad (11)$$
$$\dot{\hat{\theta}} = \Gamma P^T(x)(x - \check{x}) + \Gamma[P^T(x) - P^T(x^*)]\nabla H(x - x^*),$$

where $K_I(x) \in \mathbb{R}^{m\times m}$ is a positive matrix, $\xi \in \mathbb{R}^m$ is the controller dynamic, $P(x)$ is the matrix function satisfying Assumption 3 and α is going to be designed below.

The adaptation performance and parameter estimation strongly depends on the value of the $P(x)$ around the desired value x^*. As long as this value is non-zero, correct parameter estimation is guaranteed. Otherwise, we need to excite the system in order to generate sufficient information for adaptation law. This is more important for stabilization of the system at the origin since in many cases, the entries of the matrix $P(x)$ become zero around the origin. Consequently, the adaptation evolution stops before the estimated parameter settles on the true values. Following [10,11] and to achieve the desired performance, we add the dither signal $d(t)$ to the desired set-point to make the reference signal rich enough. In order to achieve the stabilization at the same time, we consider a decaying excitation signal as given below

$$d(t) = e^{-at}bsin(\omega t), \qquad (12)$$

where a, b and c are scalar values. The following Proposition states the asymptotic stability of the system (4) at desired non-zero constant equilibrium points x^* when we add the integral action to the system. Because of the space limitation, the proofs are omitted

Proposition 1: Consider the non-exact generalized Hamiltonian system (4) with Hamiltonian function (10), interconnected with controller (11), where

$$\alpha = -[g^T(x^*)g(x)]^{-1}g^T(x^*)[\hat{A} + K_p R(x,\hat{\theta}))\nabla H(x - x^*) - g(x^*)u^* - K_d d(t)], \qquad (13)$$

where $\hat{A} = \Delta\hat{J} - \Delta\hat{R}$ and $\Delta J = J(x,\hat{\theta}) - J(x^*,\hat{\theta})$ and $\Delta R = R(x,\hat{\theta}) - R(x^*,\hat{\theta})$. $K_p, K_d \in \mathbb{R}^{n\times n}$ are positive constant gain matrix. We also assume the squared matrix $g^T(x)g(x)$ has

full rank m for all $x \in \mathcal{D}$. Under local stabilizability condition (2), and assuming that the unstructured component $\Psi(x,\theta)$ meets the conditions of Assumption 2, the trajectory of system (4) is asymptotically stabilized at x^*.

Remark 1: The parameter convergence speed is manipulated by three factore: 1- nonlinearity of matrix $P(x)$ is, 2- entries values of matrix Λ, and 3- the gain Γ.

Remark 2: In this study, the auxilary system $\dot{\breve{x}}$ generates extra information to assist the adaptation law in finding the exact parameter value. As well, we can tune the gains to achieve the desired performance in closed-loop. As a result, we can *relax* the external excitation requirement for the estimation.

Adaptive stabilization at the zero steady state

The Hamiltonian function, centered at the origin, is expressed by

$$H(x) = \frac{1}{2}x^T x, \tag{14}$$

We consider the controller of the form

$$\begin{aligned} u &= \alpha\big(x, d, \hat{\theta}\big) + K_I(x)\xi \\ \dot{\xi} &= -K_I^T(x)g^T(x)\nabla H(x) \\ \dot{\hat{\theta}} &= \Gamma P^T(x)(x - \breve{x}), \end{aligned} \tag{15}$$

where $H(x) = \frac{1}{2}x^T x$, $K_I(x) \in \mathbb{R}^{m\times m}$ is a positive matrix, $\xi \in \mathbb{R}^m$ is the controller dynamic, $P(x)$ is the matrix function satisfying Assumption 3 and α is going to be designed below. The following Proposition states the asymptotic stability of the system (4) at $x^* = 0$ when we add the integral action to the system. The proof is omited to save on space.

Proposition 2: Consider the non-exact generalized Hamiltonian system (4) with Hamiltonian function (14), interconnected with controller (15), where

$$\begin{aligned} \alpha = -[g^T(x)g(x)]^{-1}g^T(x)\big[K_p R\big(x,\hat{\theta}\big)\nabla H(x) \\ - K_d d(t)\big], \end{aligned} \tag{16}$$

with $K_p, K_d \in \mathbb{R}^{n\times n}$ are positive constant gain matrix. We also assume the squared matrix $g^T(x)g(x)$ has full rank m for all $x \in \mathcal{D}$. Under local stabilizability condition (2), and assuming that the unstructured component $\Psi(x,\theta)$ meets the conditions of Assumption 2, the trajectory of system (4) is asymptotically stabilized at the origin.

We illustrate the construction above for the stabilization of following nonlinear system at the origin.

ILLUSTRATIVE EXAMPLE: ISOTHERMAL VAN DE VUSSE REACTION

To illustrate the constructions on non-zero steady state stabilization, we consider the van de Vusse reaction. The main reaction involves the transformation of cyclopentadiene (component A) to the product cyclopentanol (component B). A parallel reaction takes place producing the by-product dicyclopentadiene (component D). Furthermore, cyclopentenol reacts again giving the undesired product cyclopentandiol (component C). All these reactions may be described by the reaction scheme:

$$\begin{aligned} A &\rightarrow B \rightarrow C \\ 2A &\rightarrow D \end{aligned}$$

The main advantage is to obtain desirable component which is component B. We focus on the two-dimesional isothermal van de Vusse system where the steady state concentration of components depend on the dilution rate Di. We first focus on the two-dimesional isothermal van de Vusse system. The goverging equations for this system are given as

$$\begin{aligned} \dot{C_A} &= -k_1 C_A - k_3 C_A^2 + Di(C_{A0} - C_A) \\ \dot{C_B} &= k_1 C_A - k_2 C_B - Di C_B \end{aligned} \tag{17}$$

where $k_i(T_{in}) = k_{0_i}\exp\left(\frac{E_i}{RT_{in}}\right)$. The numerical values of the process parameters are given in Table 1.

Table 1: van de Vusse reaction numerical values

C_{A0}	5 mol/l
T_{in}	403.15 K
Di	15 l/hr
C_p	3.01 kJ/(kg.K)
ρ	0.9434 kJ/mol
ΔH_1	4.2 kJ/mol
ΔH_2	-11 kJ/mol
ΔH_3	-41.85 kJ/mol
k_{10}	1.287 e 12 l/(mol.hr)
k_{20}	1.287 e 12 l/(mol.hr)
k_{30}	9.043 e 9 l/(mol.hr)
E_1/R	-9758.3 K
E_2/R	-9758.3 K
E_3/R	-8560 K

By setting $C_A = x_1$, $C_B = x_2$ and $Di = u$, we obtain

$$\begin{bmatrix}\dot{x}_1 \\ \dot{x}_2\end{bmatrix} = \begin{bmatrix}-k_1 x_1 - k_3 x_1^2 \\ k_1 x_1 - k_2 x_2\end{bmatrix} + \begin{bmatrix}x_{10} - x_1 \\ -x_2\end{bmatrix} u \tag{18}$$

To check the stabilizability Assumption 1, we analyze the rank condition of the matrix $S = \big[f(x), ad_f g(x)\big]$ which is always 2 for all $x \in \mathcal{D}$ except at the origin $x_1 = x_2 = 0$; therefore, the system is stabilizable.

Application of the main results

A possible representation of the van de Vusse system is given using the Hamiltonian function

$$H(x) = \frac{1}{2}(x_1^2 + x_2^2),$$

the structured matrix

$$J(x) = \begin{bmatrix}0 & -k_1 \\ k_1 & 0\end{bmatrix}, \quad R(x) = \begin{bmatrix}k_1 + k_{3x_1} & 0 \\ 0 & k_2\end{bmatrix}$$

leaving the unstructured part of the dynamics

$$\Psi(x,\theta) = \begin{bmatrix}k_1 x_2 \\ 0\end{bmatrix}$$

We can find η and q such that the unstructured component has Lipschitz property and satisfies Assumption 2. The detailed calculations are omitted due to space limitations. We consider two cases.

k_3 is unknown

Assuming k_3 as the unknown parameter, we can find

$$P(x) = \begin{bmatrix}-x_1^2 \\ 0\end{bmatrix}, \quad Q(x) = \begin{bmatrix}-k_1 x_1 \\ k_1 x_1 - k_2 x_2\end{bmatrix} \tag{19}$$

For this case, equation (9) becomes

$$\dot{\hat{x}} = \begin{bmatrix} -x_1^2 \\ 0 \end{bmatrix} \tilde{k}_3 - \begin{bmatrix} \lambda_1 & 0 \\ 0 & \lambda_2 \end{bmatrix} \begin{bmatrix} x_1 - \hat{x}_1 \\ x_2 - \hat{x}_2 \end{bmatrix}, \qquad (20)$$

Initially, the reactor is operating at a steady-state of $x^* = (0.92,0.73)$, which corresponds to $u^* = 10(1/hr)$. The reactor temperature is fixed at $403.15\,K$ and at this temperature $k_i = (39.57,39.57,5.47)$. We seek to reach the optimum steady-state, where C_B is maximized. As the feeding rate D increases, the concentration of A and B rises simultaneously, however, increasing the D beyond a certain range of values (roughly $20(1/hr)$) does not noticeably raise C_B up (compared to C_A). On the other side, raising D results in higher operational expenses. Hence, we select $x^* = (1.49,0.98)$ as our optimal steady-state which is corresponding to $D = 20(1/hr)$.

Simulations are performed for initial condition for intial condition $x_0 = (2,1)$ and after selecting $\lambda_1 = 2, \lambda_2 = 7, K_p = [1 \quad 0; 0 \quad 1]$ and $k_i = 4$.

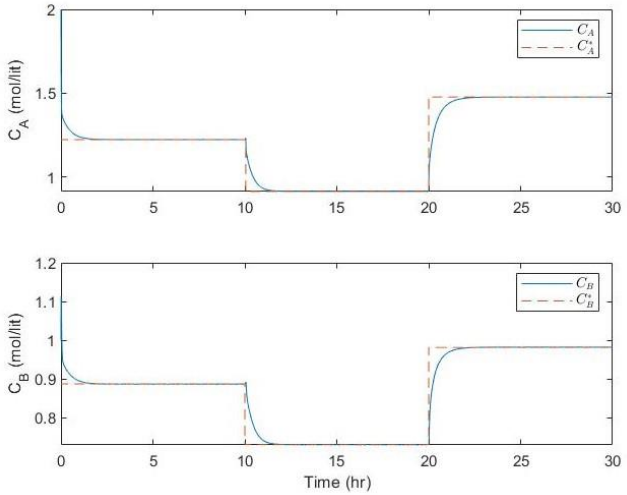

Figure 1. Closed-loop trajectory response for isothermal van de Vusse reaction when $\theta = k_3$.

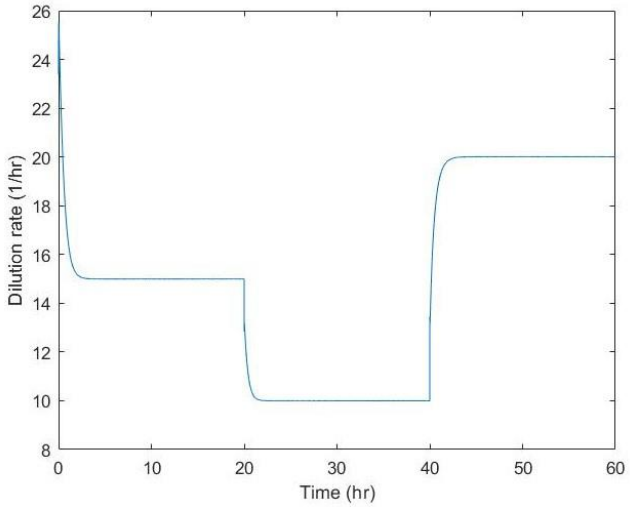

Figure 2. Adaptive controller output value for isothermal van de Vusse reaction when $\theta = k_3$.

Based on the obtained plots, the dynamic controller is able to stabilize the system and desired equilibrium points.

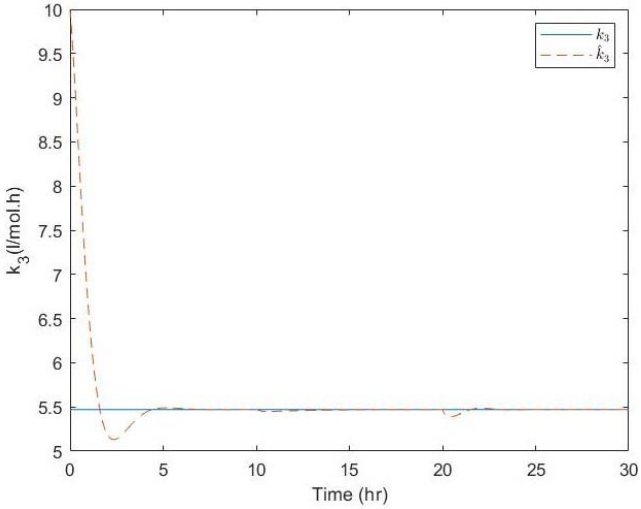

Figure 3. Closed-loop estimation response for k_3 in isothermal van de Vusse reaction when $\theta = k_3$.

Figure 1 shows that the system trajectories converge to the desired steady state. The dynamics of control input and parameter estimation responsed are given in Figure 2 and 3.

k_1, k_2 is unknown

Matrices P and Q changes to

$$P(x) = \begin{bmatrix} -x_1 - x_2 & 0 \\ x_1 & -x_2 \end{bmatrix}, \qquad Q(x) = \begin{bmatrix} -k_3 x_1^2 \\ 0 \end{bmatrix} \qquad (21)$$

Controller and trajectories responses are similar to Figures 1 and 2. Figure 4 illustrates the parameter estimation response after selecting $\lambda_1 = 2$, $\lambda_2 = 2$.

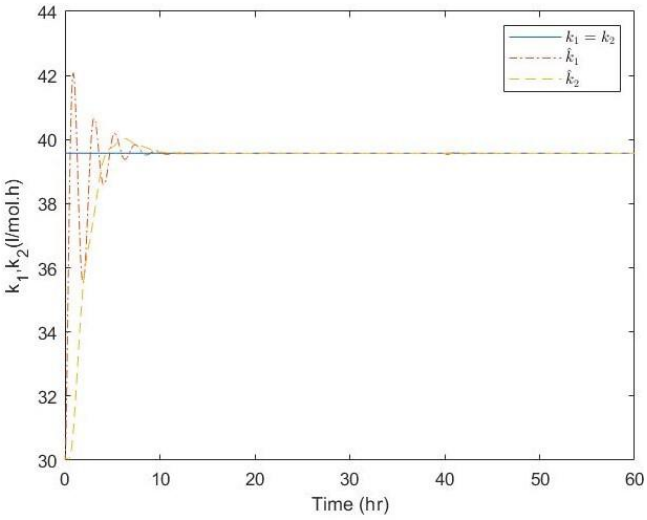

Figure 4. Closed-loop estimation response for k_1 and k_2 in isothermal van de Vusse reaction.

CONCLUSION

In this paper, we considered the problem of adaptive state feedback stabilizing controller design for a class of generalized Hamiltonian systems with unstructured component.

First, an adaptation law is designed to give an exact estimate of the parameter value. Then, a stabilizing state feedback controller is proposed using the Lyapunov stability criterion. Under a mild condition on the unstructured dynamics related to the natural dissipation of the generalized Hamiltonian system, it is shown that the overall closed-loop system is stable at the desired equilibrium point. Using this approach, a simpler controller can be designed by exploiting the generalized Hamiltonian structure without solving matching equations. Finally, the results are validated by the numerical simulation of isothermal Van de vusse reactions. Further work is underway to deal with the case that unknown parameter apears in the unstructured component as well as the adaptive output feedback desing for the proposed classes of systems.

ACKNOWLEDGEMENTS

This research is supported by the Natural Science and Engineering Research Council of Canada (NSERC) via the Discovery Grant program.

REFERENCES

1. Maschke B, Van der Schaft A. Port-Controlled Hamiltonian systems. *Modelling origins and system theoretic properties IFAC Proceedings Volumes.* 25:13:359-365 (1992)
2. Ortega R, van der Schaft A, Mareels I, Maschke B. Putting energy back in control. *IEEE Control Systems Magazine,* 21:2:18-33 (2001)
3. Hudon N, Guay M. Constructive controller design by damping feedback stabilization of control affine systems. *Systems and Control Letters* 62:11:1009-1017 (2013)
4. Guay M, Hudon N. Stabilization of nonlinear systems via potential-based realization. *IEEE Transactions on Automatic Control* 61:4:1075-1080 (2016)
5. Khalil H. Nonlinear Systems. 3rd ed. Upper Saddle River, New Jersey: prentice Hall (2002)
6. Van der Schaft A. $\mathcal{L}_2$ −Gain and Passivity Techniques in Nonlinear Control. 3rd ed, Springer (2017)
7. Praly L. Adaptive nonlinear regulation: estimaton from the Lyapunov equation. *IEEE Transactions on Automatic Control* 37:6:729-740 (1992)
8. Cao Z, Hou X, Zhao W. Adaptive robust simultaneous stabilization controller with tuning parameters design for tow dissipative Hamiltonian systems, *Archives of Control Sciences* 27:4:505-525 (2017)
9. Wei A, Wang Y. Adaptive parallel simultaneous stabilization of a set of uncertain port-controlled Hamltonian systems subject to actuator saturation, *International Journal of Adaptrive Control and Signal Processing* 28:11:1128-1144 (2014)
10. Lin J S, Kanellakopoulos I. Nonlinearities engance parameter convergence in strict feedback systems. *IEEE Transaction on Automatic Contgrol* 44:1:89-94 (1999)
11. Adelota V, Guay M. Parameter convergence in adaptive extremum-seeking control. *Automatica* 43:1:105-110 (2007)

This conference proceeding has not been peer reviewed.

PSE PRESS

PSEcommunity.org
PSE Press ● Hamilton

Chemical Institute of Canada | *For Our Future*
Institut de chimie du Canada | *Pour notre avenir*